

Portable Magnetic Resonance Sensors and Methods for Noninvasive Disease Diagnostics

by

Ashvin Bashyam

B.S. Biomedical Engineering
The University of Texas at Austin (2014)

S.M. Electrical Engineering & Computer Science
Massachusetts Institute of Technology (2016)

Submitted to the
Department of Electrical Engineering and Computer Science
in Partial Fulfillment of the Requirements for the Degree of
Doctor of Philosophy in Electrical Engineering and Computer Science
at the
Massachusetts Institute of Technology

September 2019

© 2019 Massachusetts Institute of Technology. All rights reserved.

Signature of Author
Department of Electrical Engineering and Computer Science
August 20, 2019

Certified by.....
Michael J. Cima
Professor of Materials Science and Engineering
Thesis Supervisor

Accepted by
Leslie A. Kolodziejcki
Professor of Electrical Engineering & Computer Science
Chair, Department Committee on Graduate Students

Portable Magnetic Resonance Sensors and Methods for Noninvasive Disease Diagnostics

by

Ashvin Bashyam

Submitted to the Department of Electrical Engineering and Computer Science
On August 20, 2019 in Partial Fulfillment of the
Requirements for the Degree of Doctor of Philosophy in
Electrical Engineering and Computer Science

Abstract

Many diseases manifest as a shift in fluids between distinct tissue fluid compartments. For example, fluid depletion and fluid overload lead to a deficit or accumulation of fluids within the intramuscular interstitial space. A direct measurement of these fluid shifts could serve as a highly specific diagnostic or prognostic tool to improve clinical management of these disorders. Proton magnetic resonance is exquisitely sensitive to the local physical and chemical environment of water molecules within the body. Therefore, we hypothesized that localized magnetic resonance (MR) measurements could interrogate local tissue fluid distributions and assess systemic fluid volume status. This thesis explored the potential for a portable MR sensor to characterize shifts in tissue fluid distribution and identify the onset and progression of fluid volume status disorders.

First, we designed a portable, single sided MR sensor capable of performing remote measurements of the multicomponent T2 signal originating from distinct fluid compartments. Further, we present a design framework to create single sided sensors with magnetic field strength and geometry suitable for a wide range of applications. We then demonstrate that a localized measure of tissue fluid distribution using a portable MR sensor is capable of identifying systemic changes in fluid volume status associated with fluid depletion. We validate these findings via whole animal MR measurements and a standard MRI scanner capable of localizing its measurement towards the muscle tissue. Finally, we explore new strategies to enable the translation of these portable MR sensors towards humans.

We demonstrate techniques combining multicomponent T2 relaxometry, depth-resolved measurements, and diffusion-weighted pulse sequences to improve identification of fluid shifts within muscle tissue despite the presence of confounding tissues, such as the subcutaneous tissue.

The magnetic resonance sensors and measurement techniques developed here lay the foundations for a non-invasive, portable, and quantitative indicator of tissue fluid distribution. This technology has the potential to serve as a clinical diagnostic for both localized and systemic fluid imbalances. Furthermore, these approaches enabling portable, quantitative MR measurements can be extended to the diagnosis and staging of the progression of other diseases which exhibit shifts in fluid distributions.

Thesis Supervisor: Michael J. Cima

Title: Professor, Department of Materials Science and Engineering

Acknowledgements

"Getting an education from MIT is like taking a drink from a fire hose."

Jerome Wiesner, MIT President (1971 to 1980)

First and foremost, thank you, Michael, for providing me with scientific guidance and inviting me to join your dynamic and tight-knit research group. Your contagious passion to always learn more, eagerly ask the next question, and challenge assumptions provided me with an unparalleled environment that helped me grow to be the scientist and engineer I am today. From you, I learned the importance of asking the right questions and that there's often no substitute for a well-designed experiment in the lab. Your support, encouragement, and mentorship have been an invaluable part of my graduate experience.

Thank you to each of my committee members: The generosity you showed with your time and energy truly changed the trajectory of my work. Elfar Adalsteinsson, thank you for chairing my committee and consistently offering me encouragement and positivity. Thank you, too, for welcoming me to the broader magnetic resonance community. Jacob White, I always came away from our conversations having learned something new. You taught me not to be afraid to challenge the conventional way of doing things. Denny Ausiello, you have gone above and beyond in your commitment to my personal growth and the success of my projects. The breadth of your scientific knowledge and clinical experience never failed to spark interesting conversations. You were always the voice reason who pushed me to think about how what we are doing will ultimately affect patients. Matt Rosen, you never cease to amaze me with the creativity and unwavering enthusiasm for pushing the boundaries of my work. To everyone, I am grateful for all of the candid advice, perspectives, and feedback.

I will fondly look back on my time with the Cima lab over the last five years. Thank you, Michael, for assembling and supporting such a stimulating and dynamic research environment. Not only was it a place to call home at MIT, but it also brought together a phenomenal group of people. I was lucky to get to know and learn from such wonderful colleagues. Thanks to everyone past and present whom I crossed paths with in the Cima lab; together you made my days there something I looked forward to. Thanks to Matt Li for welcoming me to the lab, showing me how to put together a magnet without losing a finger, and forever remaining a skeptic; and Alex Lammers for first showing me how to (safely) navigate a machine shop and now for showing a surprising tolerance for my puzzles. Greg Ekchian, you've opened my eyes to what it takes to run a truly translational clinical research project and to find an apartment in Kendall Square. I still don't know which scares me more. A special thanks to Chris Frangieh for being the best collaborator anyone could have hoped for and holding me accountable with my science, workouts, and smoothie habits. Khalil Ramadi, I've thoroughly enjoyed putting our heads together these past few years seeing what we can come up with. Thanks to Ritu Raman for never failing to share the inside scoop on the best ice cream in Cambridge; Max Cotler, Erin Rousseau, and Kriti Subramanyam for going the extra mile to build an open and collaborative community within the lab; and finally, thank you Wendy Brown, Barbara Layne, and Lenny Rigione for keeping the lab running smoothly over these past years. Thanks to everyone else in the lab with whom I've worked, learned, and shared countless discussions including Jay Sy, Christophoros Vassiliou, Kevin Spencer, Laura Tanenbaum, Helen Schwerdt, Chris Lee, Josh Murdock, Oliver Jonas, and Carlos Lopez to name a few. I have cherished our time together and hope our paths cross again in the future.

Thanks to everyone outside of the lab who supported my research through their generosity, ingenuity, and thoughtful advice. The extended network of collaborators and advisors, for formal and informal, made this experience so much richer. This group includes Stephen Cauley, Filiz Yetişir, Larry Wald, Clarissa Cooley, Patrick McDaniel, Nick Arango, Thomas Heldt, Bo Zhu, Krishna Nayak, Mikhail Shapiro, Mark Does, Herbert Lin, Sahir Kalim, Siavash Raigani, and Heidi Yeh. A special thanks to Jason Stockmann: you were always incredibly generous with your time (especially when it came to late night deliveries of supplies) and never hesitated to share your perspectives on all things magnetic resonance.

The research environment at the Koch Institute is truly exceptional and encouraged me to ask the sorts of questions that I simply could not imagine answering anywhere else. The scientific staff within the core facilities enabled large parts of my research. A special thanks to Wei Huang and Virginia Spanoudaki for their patience as I first learned to operate the MRI; to Kathy Cormier, Charlene Condon, Michael Brown, Weijia Zhang, and Roderick Bronson for adeptly delivering and interpreting exquisite histology slides around the clock; and to everyone who helped me master the art of collecting in vivo data: Scooter Holcombe, Vanessa Lau, Jenny Haupt, and Morgan Jamiel.

Across my department, the Koch Institute, the Biological Engineering department, and MIT, there are so many of you whom I consider dependable friends and inspirational colleagues. I hope that we continue to explore and experience the world together. Thanks to Jacob Simon, Deepak Mishra, Kelly Moynihan, Adrienne Rothschilds, Varesh Prasad, Brett Geiger, Alex Triassi, Bo Qing, Zeninjon Enwemeka, and Apoorv Gupta for welcoming me to the soccer field and (equally importantly) your cars, especially after a rainy game. Thanks to Manu Kumar, Jacob Guggenheim, and Isaac DuPree for hosting the coziest Super Bowl parties I have ever known (despite never turning the heat up enough!). Manu, thanks for joining me on the occasional run; your tireless mileage was motivating, especially in the winters. Thanks to Jacob, for never being the voice of reason during our adventures, from Iceland to Patagonia. Thanks to the many friends with whom I am fortunate to have shared a sailboat ride, a climbing or hiking trip, a relay race on the (entire) Cape, my first century bike ride, a snow shelter, or standing in line for way too long for a lobster roll. Thanks to Claire Duvallet, Khoi Nguyen, Andee Wallace, and Kelly Moynihan for helping make Boston feel like home; to Brett Geiger, Tyler Toth, Emi Lutz, and Dan Anderson for your love of the outdoors and many generous belays; to Adrienne Rothschilds for spontaneous runs along the Charles; to Josh Javor for generally wholesome conversations and for an avid love for the outdoors; to George Sun, Ally Huang, and Ross Jones for board games, beers, and the occasional hedgehog; to Julia Joung for aggressively challenging my longstanding cat allergies; to Nader Morshed for sharing your perceptive outlook on life; to Aaron Dy and Mary Dy for being the responsible adults in the room (and doing your part for science!); and to Jaideep Dudani for your contagious passion to understand the world and joining in on any and all outdoors shenanigans.

The remarkable community of Hertz Fellows has been incredibly humbling, thought provoking, and inspiring. Thanks to the always encouraging group of mentors for helping me push through the most challenging parts of this experience: Philip Welkhoff, Carla Newman, Jay Davis, Hans Mark, Robbee Kosak, Amir Nashat, Lily Kim, Scott Rakestraw, and Shannon Yee to name just a few. The community that the Hertz Foundation built catalyzed some of my most valuable friendships. Thank you especially to Judy Savitskaya for providing a constant source of humor, endless thought-provoking exchanges, and equally ambitious travel companion; and Alex Hegyi for never missing an opportunity to persuade me to move out to California and, mostly recently, for serving as our infallible drone pilot. Thanks to Megan Blewett, Aman Sinha, John Cannon, and Justin Norden for an ongoing unforgettable experience building something together and for welcoming me whenever I happen to be in town.

I am proud to say that the oftentimes eccentric, idiosyncratic Boston Hertz community has become an inextricable part of my life in Boston. Thanks to Vyas Ramanan and Kelly Moynihan for pushing the limits of science photography, inventing a new phobia (the fear of sharing one's address), and, in all seriousness, helping me understand how fascinating biology can be. Thanks to Jesse Engreitz for firing the first (but not the last) of many marshmallows; to Jim Valcourt for unknowingly offering up your apartment as tribute in the marshmallow war; to Max Kleiman-Weiner for your regular offers of surfing lessons and elaborate home-cooked dinners; to Dan Roberts for unforgettable beer fests and sharing your refined taste in bagels and Upper West Side balconies; to DJ Strouse for teaching us all about optimizing miles; to Thomas Segall-Shapiro whose lost love for beer we all mourn together; and to Cooper Rinzler for helping me see the bigger picture and teaching us all about molten semiconductors.

Thanks to my friends who have been with me from before I began this journey; you have been a constant source of joy and support. Thanks especially to Vaibhav Agarwala, Mansi Raythatha, Emmanuel Nunez, Zi-on Cheung, Chris Donahue, Jayhee Min, Suraj Makhija, Nick Kubala, and Collin Buchan who have managed to pull me away from graduate school from time to time. A special shout out to Nancy, Nancy 2, Barb, Ruth, Sonia, and Matilda for always living life the fullest.

Finally, I want to thank my family, especially my mom, dad, and Sanjai. None of this would have been possible without you. Your tireless sacrifice, endless care, and enduring support laid the foundation for everything here and onwards.

Contents

- 1 Chapter 1 Introduction..... 15
 - 1.1 Motivation: advancing diagnosis of fluid volume status imbalances 15
 - 1.1.1 Fluid depletion 15
 - 1.1.2 Fluid overload..... 17
 - 1.1.3 End-stage renal disease 17
 - 1.2 Physiology of fluid regulation..... 19
 - 1.3 Magnetic resonance measurements of tissue fluid distribution..... 19
 - 1.4 Portable MR sensors for localized measurements of fluid volume status.... 21
 - 1.5 Single sided MR sensors to enable portable, localized measurements 22
 - 1.6 Thesis overview..... 23
- 2 Chapter 2 Design of a permanent magnet array for single sided magnetic resonance..... 26
 - 2.1 Introduction 26
 - 2.1.1 High gradient magnets 26
 - 2.1.2 Sweet-spot magnets 27
 - 2.2 Unilateral Linear Halbach concept..... 30
 - 2.3 Magnet design methodology..... 32
 - 2.3.1 Parameterization of Unilateral Linear Halbach magnet design 32
 - 2.3.2 Numerical modeling of magnetic field profile..... 34
 - 2.3.3 Characterizing the performance of a magnetic field 34
 - 2.4 Effects of design parameters on magnet performance 36
 - 2.4.1 Exploration of design space 36
 - 2.4.2 Influence matrix..... 37

2.5	Magnet design, construction, and characterization	39
2.5.1	Final magnet design.....	39
2.5.2	Magnet construction	41
2.5.3	Magnet characterization.....	43
2.6	Robustness to variability in magnetization strength.....	45
2.7	Multi objective optimization of magnet performance	48
2.7.1	Background on Pareto optimality.....	49
2.7.2	Design space exploration guided by Pareto optimality	49
2.7.3	Results.....	49
2.8	Discussion	51
3	Chapter 3 Design and characterization of portable MR sensor for remote, multicomponent T2 relaxometry.....	53
3.1	Introduction	54
3.2	Portable MR sensor design.....	54
3.3	Static magnetic field characterization.....	57
3.4	Sensitivity profile characterization.....	58
3.5	Single component T2 relaxometry	59
3.6	Multiexponential fitting	62
3.7	Multicomponent T2 relaxometry	63
3.8	Discussion	64
4	Chapter 4 Identification of fluid depletion via MR measurements.....	66
4.1	Introduction	66
4.2	Mouse model of fluid loss induced by thermal dehydration	66
4.3	Whole animal MR measurements.....	68

4.4	Muscle localization via MRI.....	75
4.5	Portable MR measurements.....	85
4.6	Discussion	92
5	Chapter 5 Techniques to enable clinical translation of portable MR sensors ..	97
5.1	Introduction	98
5.2	Tuning RF excitation frequency enables slice selection	99
5.3	Multicomponent T2 relaxometry enables tissue fraction estimation.....	103
5.4	Depth sensitivity profile and tissue fraction estimation improves muscle measurement localization.....	108
5.5	Varying echo time enables sensitivity towards sample diffusivity	115
5.6	Muscle edema induces shift in multicomponent T2 relaxometry MR signal	120
5.7	Measurement of muscle edema despite proximal subcutaneous tissue	123
5.8	Discussion	130
6	Chapter 6 Perspectives and future directions.....	134
6.1	Introduction	134
6.2	New portable MR sensor design.....	135
6.3	New acquisition strategies	137
6.4	Clinical study in ESRD patients.....	139
6.4.1	Clinical motivation.....	139
6.4.2	Clinical study design.....	140
6.5	Conclusions	143
	Bibliography.....	144

List of Figures

Figure 2.1. Illustrations of prior efforts in sweet spot magnet design for single-sided NMR.....	29
Figure 2.2. Illustrations of Unilateral Linear Halbach magnet concept.	31
Figure 2.3. Illustrations defining the parameters of the Unilateral Linear Halbach magnet.....	33
Figure 2.4. Field characterization of final magnet design.	41
Figure 2.5. Renderings of magnet assembly.	43
Figure 2.6. Experimental field characterization of final magnet design.....	44
Figure 2.7. Magnet design without gaps and large magnets.	46
Figure 2.8. Magnet design with 0.25-inch magnets.	47
Figure 2.9. A subset of Pareto optimal magnets and other candidate magnets indicates the tradeoff between field strength, depth, and field volume.	50
Figure 3.1. Portable MR sensor.	55
Figure 3.2. Impedance matching circuit design and performance characterization.	56
Figure 3.3. Static magnetic field profile characterization of portable MR sensor...	57
Figure 3.4. Illustration of sensitivity profile characterization of portable MR sensor.	59
Figure 3.5. Linearity of paramagnetic species concentration versus relaxation rate from portable MR sensor.	60
Figure 3.6. Validation of T2 relaxometry measurements from portable MR sensor with benchtop NMR spectrometer.	61
Figure 3.7. Multicomponent relaxometry with portable MR sensor.....	64
Figure 4.1 Mouse model of thermal dehydration.....	68
Figure 4.2. Multiexponential fit on whole animal MR measurements.....	70
Figure 4.3. MR derived muscle signal predicts dehydration.....	72
Figure 4.4. Whole animal NMR T2 relaxometry quantifies fluid loss.....	75
Figure 4.5. ROIs on T2 weighted images of mouse leg muscle.	76

Figure 4.6 Illustration of T2 relaxometry via a series of spin echo MRI images. ...	79
Figure 4.7. T2 relaxometry decay curves from MRI.	79
Figure 4.8. Correction of Rician noise from MRI echoes improves accuracy of parameter estimates from exponential fits.	80
Figure 4.9. T2 relaxometry with MRI localized to the muscle identifies fluid depletion.	81
Figure 4.10 T2 relaxometry with MRI localized to the muscle quantifies fluid depletion due to thermal dehydration.	84
Figure 4.11 Predicting weight loss with initial MRI muscle ECF amplitude.	85
Figure 4.12 Portable MR sensor localized to the skeletal muscle.	86
Figure 4.13 Multicomponent T2 relaxometry on skeletal muscle via portable MR sensor.	88
Figure 4.14 T2 relaxometry with portable MR sensor identifies fluid depletion due to thermal dehydration.	89
Figure 4.15 T2 relaxometry with portable MR sensor quantifies fluid depletion due to thermal dehydration.	92
Figure 5.1. Illustration of portable MR sensor adjacent to lower leg of human subject.	100
Figure 5.2. Experimental schematic to characterize the sensitivity profile versus depth.	101
Figure 5.3 Sensitivity profile of portable MR sensor versus depth.	102
Figure 5.4. Spin echo duration and bandwidth versus pulse length.	102
Figure 5.5. Spin echo duration versus RF excitation frequency.	103
Figure 5.6. Multicomponent T2 relaxometry allows estimation of tissue fraction from a heterogeneous sample.	105
Figure 5.7. Residuals of ex vivo tissue hybrid sample.	106
Figure 5.8. Estimation errors from hybrid sample.	107
Figure 5.9. Synthetic subcutaneous tissue phantom.	110
Figure 5.10. Experimental schematic identifying planar subcutaneous and muscle tissue samples on top of portable MR sensor.	110

Figure 5.11. Simulation of error in estimating muscle and fat fractions versus signal SNR.	112
Figure 5.12 Method for estimating proximal subcutaneous tissue thickness.	114
Figure 5.13. Thickness estimation error versus predicted thickness for each unique subcutaneous tissue thickness.	115
Figure 5.14. Relaxation time and diffusivity of aqueous samples.	117
Figure 5.15. Varying echo time provides portable MR sensor with sensitivity towards sample diffusivity in vitro.	118
Figure 5.16 Varying echo time provides portable MR sensor with sensitivity towards sample diffusivity ex vivo.	119
Figure 5.17. Intramuscular muscle edema is evident on H&E staining.	121
Figure 5.18. Intramuscular muscle edema induces T2weighted hyperintensity. .	122
Figure 5.19. Intramuscular muscle edema shifts multicomponent T2 relaxometry signal.	123
Figure 5.20. Illustration of portable MR sensor with synthetic subcutaneous tissue phantom placed between RF transceiver coil and rat lower leg.	124
Figure 5.21. Portable MR sensor identifies onset and recovery of acute muscle edema (time domain).	125
Figure 5.22. Portable MR sensor identifies onset and recovery of acute muscle edema.	127
Figure 5.23. Muscle signal enhancement with diffusion weighting.	129
Figure 6.1. Schematic illustration of decision-support via portable MR measurement for ESRD patients.	142

List of Tables

Table 2.1. Summary of design parameters for Unilateral Linear Halbach magnet array	34
Table 2.2. Influence matrix summarizing findings from design space exploration.	38
Table 2.3. Design parameters and optimal values of final magnet design.	40
Table 2.4. Projected and actual characteristics of designed Unilateral Linear Halbach magnet.	40
Table 2.5. Performance comparison of magnet design.	48

Chapter 1

Introduction

1.1 Motivation: advancing diagnosis of fluid volume status imbalances

1.1.1 Fluid depletion

Hyperosmotic dehydration traditionally refers to a total body water deficit often induced by a combination of restricted fluid intake and exposure to adverse environments ¹. Fluid volume depletion is associated with poorer health outcomes when concomitant with chronic diseases, increased mortality among elderly and intensive care patients, decreased physical and cognitive performance, and impaired postoperative recovery ^{2–10}.

Undiagnosed dehydration leads to negative health effects across many patient populations. These include those experiencing dehydration due to limited fluid intake, environmental exposure, or physical activity; critically ill patients in the intensive care unit; elderly and neonatal patients; and those presenting to the emergency department ^{1,2,15,16,7–14}. Accurate and timely diagnosis is challenging as clinical presentation and symptoms are nonspecific and often present as an accompanying comorbidity to the primary diagnosis ^{1,6,17}. For example, geriatric patients are highly susceptible to dehydration due to diminished thirst perception and plasma vasopressin ^{6,18–20}. A diagnosis of dehydration in the elderly upon hospital admission increased 30-day post-admission mortality rate by 80% ¹⁷.

Soldiers are especially vulnerable to dehydration due to extended exposure in extreme environments, scenarios of intense stress where thirst perception is diminished, and limited water storage/transportation capabilities¹³. Additionally, a real-time measure of fluid volume status could inform fluid management in ICU patients, especially those contraindicated for invasive measures such as right heart catheterization.

Despite the substantial health consequences of unmanaged dehydration, no accurate, robust, and practical assessment method currently exists^{1,21}. Commonly used vital signs and symptoms (e.g. headache, oral mucosa assessment, capillary refill time, skin turgor, fatigue) fail to provide a specific or objective assessment of dehydration^{21–25}. These diagnostic criteria do not provide an accurate measure of dehydration and are easily confounded by other comorbidities such as vascular disease, neurological deficit, and environmental conditions. Signs and symptoms of dehydration are often only apparent after fluid loss has progressed to severe stages.

Existing techniques involving sampling urine and/or blood, while clinically valid and accurate, are confounded by many factors, are invasive, require complex or time-consuming methods, and/or cannot be deployed in many settings (e.g. point of care)^{26–30}. Measurements of more easily accessible bodily fluids (e.g. saliva, tears, and sweat) exhibit substantial variability between individuals and are strongly biased by factors such as physical activity, food consumption, and humidity^{31,32}. Bioimpedance-based estimates of total body water as well as extracellular and intracellular fluid volumes fail to provide an actionable measure of fluid loss as its variability between individuals is substantial even when closely following measurement protocols^{33–35}. The variability of bioimpedance-based techniques is likely due to its reliance on an empirically derived model in healthy adults, which may not generalize to more diverse patient populations. Existing efforts to measure dehydration have focused on measurement of easily accessible, indirect physiological responses to fluid depletion. The inherently large variability in the

response of individuals towards dehydration and a multitude of confounding factors limits the widespread adoption of these techniques ¹.

There is a clear need for new approaches towards simple, non-invasive, and reliable measurement of fluid depletion. Desirable methods would interrogate and identify the underlying physiological response to dehydration, namely perturbations in the fluid distribution between tissues, and would not be based on population models ³⁰.

1.1.2 Fluid overload

On the other end of the spectrum of fluid volume status, fluid overload or hypervolemia can indicate the progression of a variety of diseases. Fluid overload is associated with congestive heart failure (CHF), end-stage renal disease (ESRD), and liver failure (1–9). Identification of fluid overload may inform improved treatment for patients with these chronic diseases.

Congestive heart failure is a chronic cardiovascular disease with 6 million patients in the United States³⁶. The pathologic accumulation of excess fluid throughout the body (congestion) negatively impacts patient quality of life, through decreased autonomy and mobility, pain, and fatigue^{37–40}. CHF is one of the leading causes of hospitalization and hospital readmission in the elderly ^{36,41}. Early identification of changes in cardiac function, especially acute decompensated heart failure, can improve management through interventions to reduce hospitalization rate, improve patient outcomes and decrease healthcare expenditures.

1.1.3 End-stage renal disease

The identification of both hypovolemia and hypervolemia is of critical importance to end-stage renal disease patients undergoing hemodialysis (HD). Accurate, real-time monitoring of volume status would improve outcomes for ESRD patients ⁴². ESRD patients have excess fluid regularly removed via hemodialysis. Ultrafiltration goals during HD are guided by estimating euvoletic weight (i.e. dry weight) of the

patient. The removal of excess fluid beyond that necessary to reach dry weight leads to intradialytic hypotension (IDH). IDH occurs in up to 75% of hemodialysis patients and can cause nausea, vomiting, cramping, and chest pain ¹⁶. This negatively affects patient quality of life and reduces long-term compliance with HD prescription ⁴³. Increased morbidity of IDH includes bowel ischemia, stroke, fistula thrombosis, myocardial infarction which is associated with a 26% increase in mortality ^{44,45}. Myocardial stunning due to intradialytic hypovolemia induces changes such as fibrosis, remodeling, and hypertrophy, which are risk factors for future cardiac events ⁴⁶. Furthermore, repeated, acute cerebral ischemia is associated with cognitive decline and neurological disease (e.g. dementia) ⁴⁷. Long-term volume overload and poorly managed ultrafiltration rates are also common ^{48,49}. Clinicians and patients lack a simple and reliable tool to measure the extent of fluid overload to assist with long-term fluid management or to indicate when HD patients are at risk for IDH ^{42,45,50}.

Current techniques for the identification and treatment of fluid overload are unable to provide a valid assessment of volume status consistent across HD sessions and HD patients ^{42,50–53}. Existing management efforts rely heavily on clinical signs and patients' weight change throughout the course of a HD session ⁵¹. Clinical assessments are subjective and, in many cases, unable to predict fluid overload ⁵⁴. For example, pedal edema, a commonly utilized clinical measure of volume overload, correlates poorly with many other more objective, resource-intensive measures of fluid overload ⁵⁵. Existing management efforts rely on weighing patients before each session. This technique does not resolve individual fluid compartments and is easily confounded by changes in nutrition, lean body mass, poor appetite, infection, and many other factors ^{22,48,51,53,56}.

Alternative techniques for indicating a patient's dry weight, such as bioimpedance, blood pressure, and biochemical markers similarly rely on systemic physiological changes rather than directly measuring fluid distribution. These methods therefore exhibit large interpatient and inpatient variability ^{22,50,51}. These techniques

cannot robustly characterize dynamics in the underlying physiology (i.e. interstitial fluid depletion as HD progresses).

1.2 Physiology of fluid regulation

We sought to develop a diagnostic capable of interrogating the underlying physiology of fluid volume status imbalances. A direct measurement of the distribution of fluids within tissue is likely to be less susceptible to confounding factors that affect other measurements that less directly assess fluid distribution.

Disruptions in fluid volume status are characterized by changes in the distribution of water between body fluid compartments and tissues ⁵⁷⁻⁵⁹. Dehydration, specifically hyperosmotic dehydration, is characterized by a shift in the distribution of water within tissue fluid compartments driven by homeostatic regulation ^{57,58,60-62}. Dehydration induces relatively large volume depletion of the intramuscular fluid compartments (extracellular and intracellular) suggesting that a measurement of these tissue-specific fluid volumes could inform a diagnosis of dehydration ⁵⁸. Conversely, hypervolemia induce an expansion of these fluid compartments.

Furthermore, the intramuscular extracellular fluid (ECF) compartment is more highly responsive to these fluid shifts than the intracellular fluid (ICF) compartment and either compartment in the subcutaneous space ^{58,63}. ECF fluid depletion is driven primarily by fluid shifts from the interstitial space into the vascular space to maintain electrolyte and osmotic balance. The opposite is true during ECF fluid expansion concomitant with fluid overload. Therefore, a localized measurement of shifts in fluid within the intramuscular fluid compartments could serve as an indicator of disruption to systemic euvolemia.

1.3 Magnetic resonance measurements of tissue fluid distribution

Proton nuclear magnetic resonance (^1H NMR) is exquisitely sensitive to the local physical and chemical environment of water molecules within the body⁶⁴. A T2-based MR measurement can provide information related to the composition and volume of a fluid compartment.

A magnetic resonance relaxation process can be characterized by two time constants as shown by Bloch ⁶⁵. The first, known as spin-lattice relaxation or longitudinal relaxation, is denoted as T1. The second, known as spin-spin relaxation or transverse relaxation, is denoted as T2. A measurement of these relaxation times can provide information related to the material, chemical, and physical properties of a sample. A sample comprised of multiple distinct fluid compartments, such as tissue with intracellular and extracellular compartments, can produce an MR signal described by multiple T2 relaxation processes. The amplitude of each of these components can be used to estimate the relative size or volume of its respective compartment. The relaxation time of each component can provide information related to the identity of the respective compartment (e.g. intracellular, interstitial, etc.) ^{66–69}. The use of a multiexponential decay model to extract information related to the identity and relative volume of a heterogeneous sample is known as multicomponent T2 relaxometry.

Our group previously demonstrated that multicomponent T2 relaxometry via whole-body NMR can identify fluid depletion as a decrease in the signal amplitude from the lean tissue component⁷⁰. This led us to explore the localization of a similar measurement towards the skeletal muscle tissue with the ultimate goal of miniaturizing the magnetic resonance (MR) sensor.

Multicomponent T2 relaxometry via magnetic resonance imaging has demonstrated sensitivity towards distinct fluid compartments within skeletal muscle tissue ⁷¹. These fluid compartments correspond to intracellular and extracellular water ^{68,72–74}. Lower extremity skeletal muscle offers an easily accessible site due to its

relatively large size and a thin subcutaneous tissue layer for a portable magnetic resonance sensor performing a localized measurement.

1.4 Portable MR sensors for localized measurements of fluid volume status

The ultimate goal of this work was to develop a portable sensor to measure fluid volume status rather than requiring a whole body measurement. The ability to perform a localized measurement towards a specific tissue compartment is essential to allow for the miniaturization of this MR measurement into a portable MR sensor.

A portable MR sensor would offer many advantages over both traditional MRI and other measurements of fluid overload. Its miniature size and low power consumption would offer a mobile platform capable of performing measurements across a wide range of environments including hospitals, outpatient facilities, sporting events, and military operations. This would increase the availability of volume status measurements especially outside of highly resourced environments, such as hospitals. A portable MR sensor dedicated to the measurement of fluid volume status would be straightforward to operate as there would be no need for any user controlled acquisition parameters. This is critical to ensure widespread adoption by clinical staff (e.g. nurses, technicians). Furthermore, the interpretation of the measurement would be fully automated in contrast to traditional MRI. The potential to perform these MR measurements without a trained operator or radiologist for image interpretation would increase accessibility of fluid volume status measurements. Finally, a high sensitivity device would enable the measurement to be performed in a few minutes suggesting the potential for use as a real-time measure of fluid volume status.

1.5 Single sided MR sensors to enable portable, localized measurements

Existing approaches towards portable MR sensors typically rely on single sided sensors. These sensors, also known as unilateral sensors, allows measurement of spin relaxation properties of samples remote from the surface of the device due to their open geometry and portability ⁷⁵. The ability to perform in situ measurements of arbitrarily sized objects, even those larger than the sensor, is critical to allow a miniaturized sensor to perform a measurement of human skeletal muscle tissue.

These single sided magnetics can be inadequate in their ability to isolate the measurement towards the muscle tissue due to limitations in penetration depth, spatial selectivity, and available contrast mechanisms ^{76,77}. Measurement of skeletal muscle tissue in the extremities requires penetration beyond the proximal subcutaneous tissue ⁷⁸. Measurement depth is highly constrained due to the rapid attenuation of static and RF magnetic fields away from the surface of the sensor. Larger devices can achieve increased penetration depth, but this compromises portability and increases cost. Encoding spatial information via switchable gradients is substantially more difficult with single sided MR sensors compared to MRI due to the high field inhomogeneity of their static and gradient magnetic fields and restrictions on allowable tissue RF power deposition. Therefore, single sided MR measurements of the muscle are often contaminated by other nearby tissues. The available contrast mechanisms to help isolate the signal from a single tissue (i.e. muscle) are restricted due to the relatively low sensitivity and high magnetic field inhomogeneity of single sided MR devices. Many pulse sequences capable of separating fat from other tissues rely on phenomena such as chemical shift, which cannot be realized given the relatively high field inhomogeneity of single sided MR sensors compared to traditional MRI.

The presence of confounding tissues, such as subcutaneous tissue, can obscure or confound measurements intended to be isolated towards the muscle tissue.

Separation of signals originating from tissues with similar relaxation properties is difficult and a substantial source of error in relaxometry studies ⁷⁹. Performing multicomponent T2 measurements relatively deep within the tissue with a single sided MR sensor while maintaining sensitivity is challenging.

1.6 Thesis overview

Existing approaches towards management of diseases related to imbalances in fluid volume status are rudimentary and rely on nonspecific indicators of patient volume status. The use of clinical signs and physical symptoms has been augmented by the introduction of laboratory tests and more advanced measurement techniques (e.g. bioimpedance, ultrasound). Despite these advances, no true gold standard exists for the measurement of fluid volume status. The presence of numerous confounding factors limits the effectiveness of existing indirect measurements of systemic fluid distribution. A more direct measure that interrogates the distribution of fluids within tissue may improve our ability to identify imbalances to euvoemia before clinical signs become apparent.

This thesis sought to explore the potential for a portable magnetic resonance-based measurement, localized to the skeletal muscle tissue, to identify imbalances in fluid volume status. Magnetic resonance is known to exhibit sensitivity towards the distribution of fluids within heterogeneous samples. The skeletal muscle offers an ideal target tissue for this measurement as it acts as an amplifier of deviations in systemic fluid volume status from euvoemia. Furthermore, a portable MR sensor may be able to perform a remote measurement of the skeletal muscle as it is easily accessible in most patients.

The research that comprises this thesis is organized into distinct sections corresponding to the progression of this vision from a concept towards human

translation. First, we present a new design for single sided portable MR sensors that enables high sensitivity measurements of regions remote from the surface of the sensor (Chapter 2). Additionally, we present a framework to tune the magnetic field strength and geometry to be extended and applied more generally. We then design and characterize a portable MR sensor capable of performing T2 relaxometry within tissue for use in fluid volume status measurements (Chapter 3). We then explore the potential for this technology to be applied towards the identification and quantification of fluid loss in a preclinical model (Chapter 3). This validates both our hypothesis of applying T2-based MR towards the identification of dehydration and the use of our portable MR sensor as a superior alternative to MRI. We then looked towards human translation and explored strategies to increase the penetration depth and isolation of the muscle signal of portable MR measurements (Chapter 3). Finally, perspectives on this work and potential future directions are presented (Chapter 6).

This page intentionally left blank

Chapter 2

Design of a permanent magnet array for single sided magnetic resonance

2.1 Introduction

Single-sided NMR, also known as unilateral NMR, allows measurement of spin relaxation and diffusion properties for samples remote from the surface of the device due to their open geometry and portability ⁷⁵. The ability to perform in situ measurements of arbitrarily sized objects, even those larger than the sensor, opens applications in healthcare, materials analysis, food quality assurance, and the oil and gas industry ^{80–84}. Traditional closed-bore NMR systems, such as MRI, are often unsuitable where the sample is much larger than the sensor, a portable sensor is required, or resource limitations preclude the use of such systems.

The primary component of an NMR system is the magnet, which provides the static magnetic field for nuclear polarization. This work focuses on magnets produced by an array of permanent magnets due to their cost effectiveness, low maintenance and power requirements, and portability. Demas et al. offers a more detailed assessment of the tradeoffs between various magnet technologies for NMR ⁷⁶. Magnet assemblies for this purpose fall into one of two classes: a) high gradient or b) sweet spot.

2.1.1 High gradient magnets

High gradient designs feature an inhomogeneous magnetic field oriented either parallel or perpendicular to the surface of the sensor ⁸⁵⁻⁸⁷. This design offers higher magnetic field strength and more efficient use of magnetic flux leading to smaller sensors. These magnets are suitable when one-dimensional imaging, rather than a highly uniform field for bulk measurements, is desired ⁸⁸. Signal localization is achieved by encoding position via the static magnetic field gradient ⁸⁸. The ability to localize the source of the signal to a well-defined region using frequency selective RF pulses allows the RF coil geometry to be precisely tuned to closely match the field profiles of the B_0 and B_1 fields while maintaining their perpendicularity for optimal sensitivity. Spin-echo pulse sequences are typically used with these sensors, rather than gradient-echo, due to the high degree of field inhomogeneity. The high gradient inherent to these designs precludes the use of these systems for measuring high mobility spins, such as those with free-fluid which often includes biological samples due to dephasing induced by diffusion ⁶⁴. While this can be partially mitigating through shimming and pulse sequence selection, the loss in sensitivity can exceed an order of magnitude when performing high spatial resolution (<100 μm) measurements ⁸⁹.

2.1.2 Sweet-spot magnets

Sweet-spot magnets, the focus of this work, generate a uniform magnetic field containing a saddle region. A saddle region is a volume where the gradient of the magnetic field is close to zero. The magnetic field can be parallel or perpendicular to the surface of the sensor. This region of local homogeneity can be much larger than the sensitive region formed with a high gradient magnet, especially along the axis perpendicular to the surface of the sensor. This can allow for measurement of a larger sample for fixed RF power and bandwidth ⁹⁰. Further, the more homogeneous field reduces signal attenuation induced by diffusive motion of spins. This is valuable when measuring samples, such as biological samples or human tissue, with substantial free fluid.

There have been numerous prior efforts in designing sweet spot magnets as shown in **Figure 2.1**. A well-known early demonstration directed the static magnetic field perpendicular to the surface of the sensor as shown in **Figure 2.1a** ^{90,91}. While offering a more straightforward approach towards magnet design, RF coil design becomes more challenging as traditional solenoidal coils located on the surface of the magnet cannot be utilized. As a result, the expected improvement in sensitivity from a sweet spot magnet can be considerably compromised ⁷⁵.

The magnet design shown in **Figure 2.1b** demonstrates a magnetic field oriented parallel to the surface of the sensor using a sweet spot region-of-interest (ROI) geometry ⁹². The saddle region is generated by orienting two identically magnetized magnets axially and in the same direction. A gap between the magnets allows for a saddle region to be formed. Magnetic flux is more efficiently utilized since the magnets are oriented in the same direction as the static magnetic field within the ROI allowing for a compact design.

Finally the design shown in **Figure 2.1c** combines principles from the previous two designs: a) the use of an offset central magnet to produce a saddle region through field cancellation and b) the use of magnets oriented parallel to the surface of the sensor to efficiently produce a uniform region in the same direction ⁷⁷. This design is limited in the degree of control it offers over the size, shape, and position of the uniform region. Marble et al. and Pulyer et al. provide a more thorough review and comparison of past sweet spot magnets ^{77,93}.

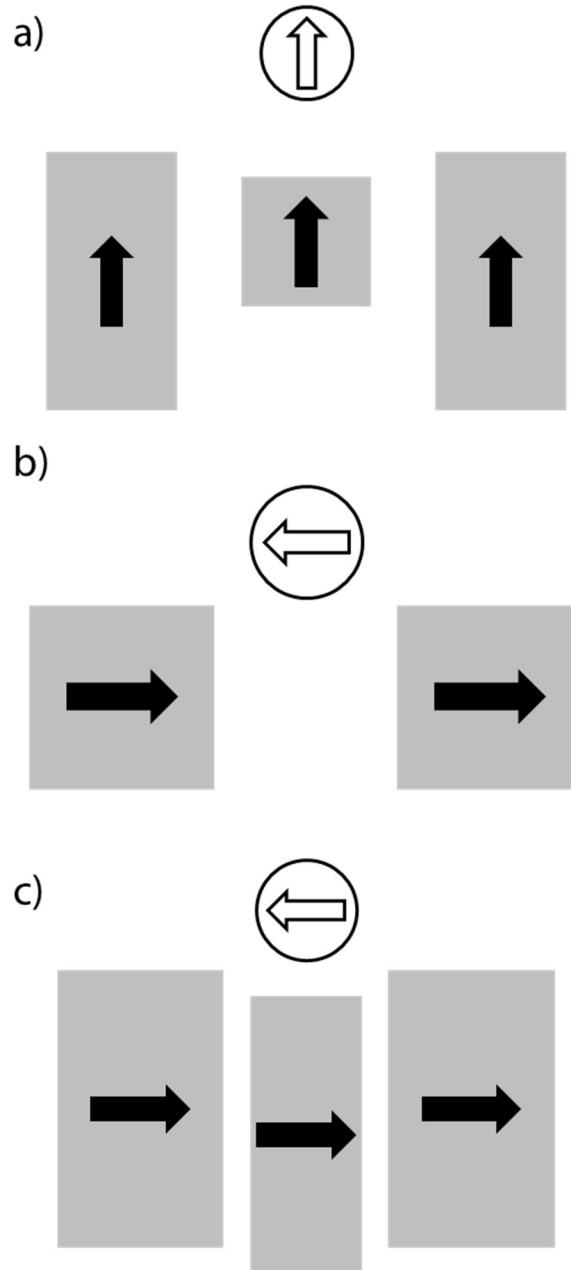


Figure 2.1. Illustrations of prior efforts in sweet spot magnet design for single-sided NMR. Rectangles represent magnets with inset arrows indicating magnetization direction. Circles represent remote uniform magnetic field region with inset arrows indicating field direction.

We propose a novel sweet spot magnet geometry, the Unilateral Linear Halbach, as shown in **Figure 2.2**, that combines principles from a linear Halbach array magnet with that of the sweet spot magnet demonstrated by Marble et al. ^{77,94}. We demonstrate that the introduction of vertically oriented magnets, at opposing faces along the magnetization direction of the array, termed Halbach elements, provides

a sweet spot design with a tunable geometry. The addition of Halbach elements improves the utilization of stray magnetic flux allowing for a larger and stronger uniform region. The central slice is offset in the $-y$ direction, similarly to the magnet shown in **Figure 2.1c**, which allows it to increase the field strength of the uniform region without disrupting the saddle region created from the adjacent magnets. In this work, we explore the influence each design parameter has on magnet performance using finite element analysis to produce a framework for Unilateral Linear Halbach design. Finally, we experimentally validate these findings through design, construction, and characterization of a magnet suitable for use within a portable medical diagnostic sensor.

2.2 Unilateral Linear Halbach concept

The Unilateral Linear Halbach utilizes a magnet geometry similar to that of Marble et al. (**Figure 2.1c**) surrounded by vertically oriented magnets which augment the magnetic field with elements from a linear Halbach array^{77,94} as shown in **Figure 2.2**. The central elements are magnetized in a direction parallel to the surface of the sensor. These elements produce a uniform region with a zeroed second derivative. The middle of magnet is lower than the adjacent magnets. The outer elements are magnetized in a direction perpendicular to the surface of the sensor. The elements follow the magnetization scheme of a linear Halbach array. In the example shown below, the magnetization of the leftmost element is pointing towards the surface of the sensor while the rightmost element is antiparallel.

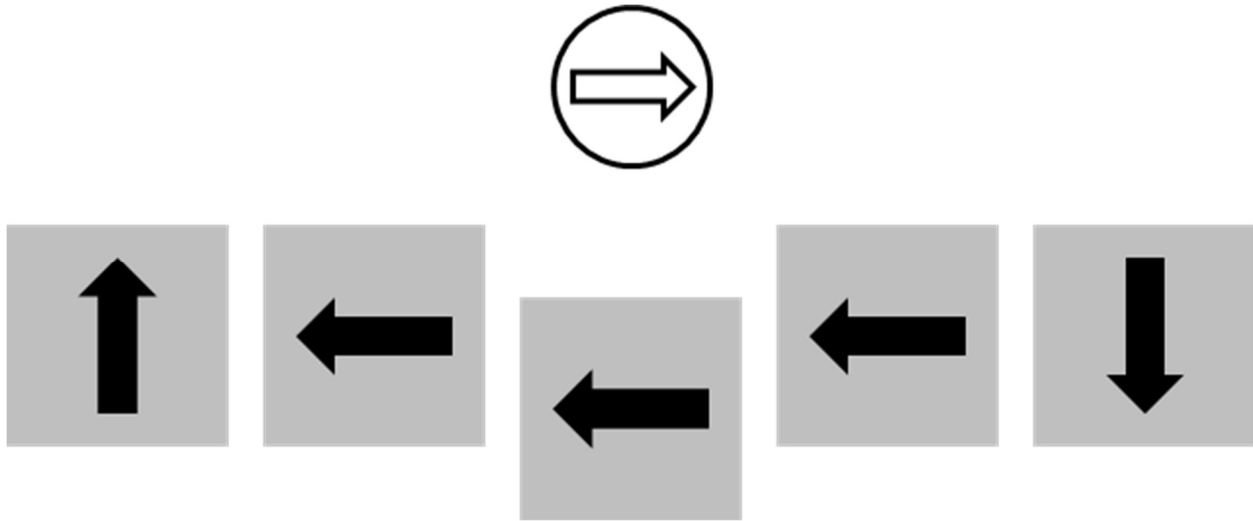


Figure 2.2. Illustrations of Unilateral Linear Halbach magnet concept. Rectangles represent magnets with inset arrows indicating magnetization direction. Circles represent remote uniform magnetic field region with inset arrows indicating field direction.

This design generalizes to magnet assemblies comprising many identical discrete magnets where this pattern is repeated along the two axes perpendicular to the magnetic field. Magnets constructed from tens or hundreds of separate magnets, rather than a few large magnets, offer many advantages. Manufacturing introduces inherent variability between each magnet. The use of many magnets allows these undesired fluctuations to counteract each other producing a more uniform field. Designs comprising fewer numbers of magnets often require shimming to achieve desired field uniformity ^{77,95}. Each magnet provides many additional degrees of freedom that can be individually tuned and optimized. In this design, we choose not to handle each magnet individually for simplicity. Extending this work to allow for that would be straightforward. Assembling a magnet array can require specialized equipment and pose unique safety hazards due to the large and sometimes unpredictable forces between magnets ⁹⁶. Our design, using hundreds of relatively small magnets, limited the assembly forces on a magnet to 110 N (~25 lbs) during insertion which is easily manageable without extensive mechanical assistance. This simplifies the construction process, as much less robust fixtures are necessary. A downside to working with individual magnets is the reduced amount of magnetic material, which translates into decreased field strength. Gaps between the magnets

within the assembly, which are often inevitable to ensure structural integrity and manufacturability, are non-magnetic and, therefore, do not contribute to the magnetic field profile. The improvement in field uniformity afforded by the cancelation of inter-magnet variability outweighs the losses in field strength due to gaps between magnets (**Table 2.5**). Simulation results indicate that inter-magnet variability compromises the size and shape of the uniform region with a design utilizing a few larger magnets, especially at higher levels of variability (e.g. $\pm 4\%$ to $\pm 8\%$ relative magnetization tolerances).

As is the case with most sweet-spot magnets, there is a tradeoff between the field strength, field uniformity, and the distance of the uniform region (or sweet-spot) from the surface of the magnet. A major task in magnet design is assessing these tradeoffs and identifying an optimal design. The effect of each design variable on the performance of the magnet is explored and discussed in the following section.

2.3 Magnet design methodology

2.3.1 Parameterization of Unilateral Linear Halbach magnet design

The magnet array, defined as the relative position of each magnet, is described by the side length of each individual magnet, number of slices in each direction, relative position and orientation of the slices, and the gaps between the slices as shown in **Figure 2.3** and **Table 2.1**. The design shown below, indicating the initial design for this work, was inspired by the approximate geometry of previous single-sided magnets^{77,86}. We chose to use 12.7 mm (1/2 inch) N52 neodymium magnets as they offered a high performance (maximum energy product), cost-effectiveness, and a safe magnet around which to base our design. Larger magnets (19 mm or 3/4 inch) offered the ability to design an assembly with less of its internal volume occupied by air gaps, but the downsides of both increased susceptibility to inter-magnet

variability (due to the decrease in total number of magnets) and increased attractive forces during assembly outweighed the potential advantage.

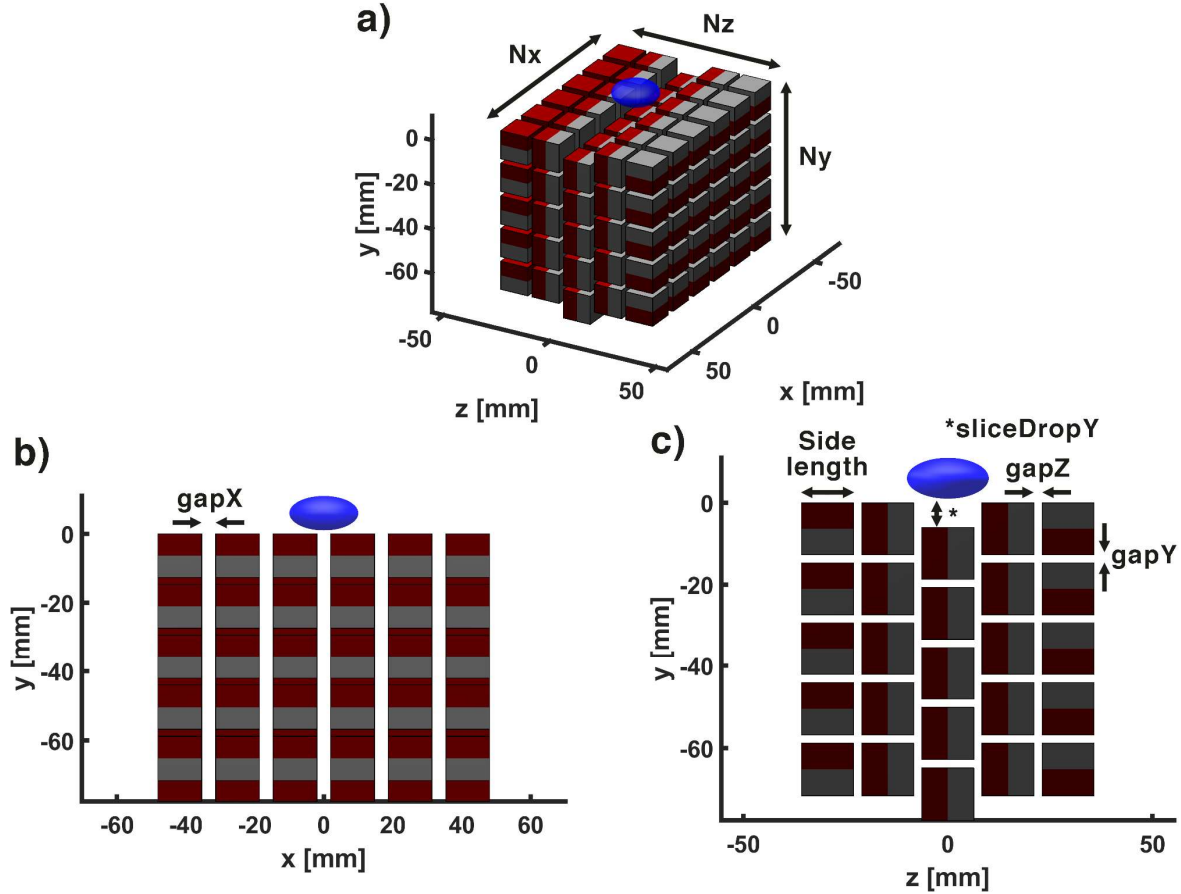


Figure 2.3. Illustrations defining the parameters of the Unilateral Linear Halbach magnet. The magnets are defined by their individual side length, the number of magnets in each direction (N_x , N_y , N_z), their relative spacing ($gapX$, $gapY$, $gapZ$), and the distance that the middle slice is depressed ($sliceDropY$). Red and grey shading indicates positive and negative poles, respectively. Blue ellipsoid indicates approximate location of uniform region of magnetic field.

Parameter	Description
N_x	Number of magnets in x direction
N_y	Number of magnets in y direction
N_z	Number of magnets in z direction

<i>gapX</i>	Air gap between adjacent magnets in x direction, [mm]
<i>gapY</i>	Air gap between adjacent magnets in y direction, [mm]
<i>gapZ</i>	Air gap between adjacent magnets in z direction, [mm]
<i>sliceDropY</i>	Displacement of middle slice in $-y$ direction, [mm]

Table 2.1. Summary of design parameters for Unilateral Linear Halbach magnet array

2.3.2 Numerical modeling of magnetic field profile

Finite element analysis using COMSOL Multiphysics (Burlington, MA) was performed to simulate the magnetic field profile generated by the magnet array. The remanence (remanent flux density) and magnetic permeability of each magnet was specified based on theoretical values for N52 neodymium magnets. This analysis was performed through finite element analysis on a user-defined mesh on which it solves Gauss' Law for the magnetic field using the magnetic potential.

Magnets were defined as cubes with a side length of 12.7 mm (1/2 inch) with a remanent flux density of 1.48 Tesla and a relative permeability of unity with compensation for saturation of the magnets. The entire simulation was performed within a rectangular prism surrounding the magnets defined as air with no magnetization and a relative permeability of unity.

2.3.3 Characterizing the performance of a magnetic field

A set of metrics were derived from the magnetic field, which defined its geometry and strength in order to compare the fields generated by magnets with different

configurations. The uniform region was found by finding the contiguous region of $B_z(x, y, z)$ defined as the volume \mathcal{V} , which maximized an approximation of the signal to noise ratio of a thermal noise limited NMR experiment as calculated by Hoult and Richards ⁹⁷. The approximate expression for the signal to noise ratio, assuming a well-designed transceiver coil, is given as:

$$SNR \cong \int_{\mathcal{V}} B_z(x, y, z)^{\frac{7}{4}} d\mathcal{V} \quad (2.1)$$

The maximum field deviation within the uniform region, $B_z(\mathcal{V})$, was constrained to less than ϵ (1%), which represents a reasonable bandwidth for the RF excitation pulse ⁹⁸:

$$\max(B_z(\mathcal{V})) - \min(B_z(\mathcal{V})) \leq \epsilon * B_{z,0} \quad (2.2)$$

where ϵ is the uniformity of the magnetic field and $B_{z,0}$ is the magnetic field strength of the uniform region and is defined as the mean of the minimum and maximum field strengths within the uniform region. This assumes the Q factor of the RF transceiver coil will be sufficiently low to ensure that this pulse bandwidth is achievable.

The following constraint was enforced to ensure that the uniform region was sufficiently uniform in orientation as off axis precession can introduce artifacts into the measurement ⁹⁹:

$$\tan^{-1} \sqrt{\frac{B_x(\mathcal{V})^2 + B_y(\mathcal{V})^2}{B_z(\mathcal{V})^2}} \leq 1^\circ, \forall \mathcal{V} \quad (2.3)$$

The $B_{z,0}$ that defined the uniform region with maximum SNR as in **Equation (2.1)** with each point within the region satisfying the constraints as in **Equations (2.2)** and **(2.3)** was computed for a given magnet design. The following metrics were then

computed to allow comparison of fields produced by different magnet designs: magnetic field strength (B_0), volume, size in the x direction measured from the center ($sizeX$), size in the y direction measured from the center ($sizeY$), size in the z direction measured from the center ($sizeZ$), and distance from the surface of the magnet to the center of the field ($posY$) which can be considered an approximation of measurement depth. These metrics are used to design a magnet array based on the desired application. Further constraints were imposed to ensure that the uniform region was centered above the magnet and the majority of its volume existed within a convex hull. This ensures that a standard solenoidal transceiver coil will be able to excite a sample within the uniform region.

2.4 Effects of design parameters on magnet performance

2.4.1 Exploration of design space

Each design parameter was varied and its effect on the performance of the magnetic field assessed. This formed the basis for design of the final magnet assembly as tradeoffs between magnetic field performance could be considered. The performance metrics considered, derived from the uniform magnetic field, are the field strength (B_0), the depth or distance from the surface of the sensor ($posY$), and the sizes in each direction ($sizeX$, $sizeY$, $sizeZ$). For simplicity, all other parameters were held constant.

The number of magnets in each direction is a primary determinant of magnet performance and, therefore, suitability for a particular application. The size and strength of the uniform region is strongly affected by the total amount of magnetic material. Excessive size, mass, or strength of stray fields can contraindicate a magnet for a given application. The tuning of the gaps between slices also has a substantial effect on the field strength, size, and shape of the uniform region. Some

parameters were varied in conjunction due to the highly interdependent nature of these parameters on the performance of the magnet.

2.4.2 Influence matrix

The results of this exploration of the design space provide guidance towards how design parameters can be tuned to produce stronger, deeper, and larger uniform magnet fields, as shown in **Table 2.2**. These first-order relationships indicate that the design parameters fully span the set of performance metrics. Many of the design parameters have a clear effect on magnet performance, such as the effect of the number of magnets on field strength. Others exhibit more complex behavior, such as the effect of the gaps in the x or z directions on the size of the uniform region.

A strategy to guide the design of a magnet assembly can be formulated based on these findings. The gap in each direction should be minimized to the furthest extent that the given manufacturing method allows. This will maximize magnetic field strength while minimally affecting the depth and size of the uniform region. The number of magnets in the z direction should be set to achieve the desired magnet size while exceeding the desired depth. Finally, magnets in the x and y directions should be added until the desired tradeoff between depth and field strength is achieved. This final step should be repeated for various values of *sliceDropY* until a suitable compromise between performance metrics is met.

As an alternative to the proposed heuristics-based approach, a more formal formulation of the design goal would enable use of optimization tools. Two main challenges arise upon taking this approach. First, it is unclear how to establish an objective function capable of fully defining the design goals while also appropriately penalizing deviations in each performance metric. Determining if certain tradeoffs are acceptable is not always straightforward, even when designing for a particular application. Second, the high dimensionality and computational cost of simulating the magnetic field profile precludes the use of many traditional optimization

algorithms. Techniques such as genetic algorithms, Monte Carlo algorithms, and multi-objective optimization have been previously applied towards magnet design for NMR ^{100,101}. We explored the use of Pareto optimality with two design criteria – the depth and the volume of the uniform region – while constraining the design with a minimum magnetic field strength and maximum magnetic mass. We found that a consistent tradeoff exists between depth of the uniform region, volume of the uniform region, and the magnetic field strength. This process could aid in the selection of an optimal design given a set of constraints. The optimal magnet design will depend on the application as factors including geometry of the sample, desired acquisition time, and sensitivity must be considered.

	Field strength	Depth	Size, x	Size, y	Size, z
Nx	+	–	+		
Ny	+	–		–	
Nz	–	+			+
$gapX$	–	–			–
$gapY$	–	+			
$gapZ$	–	+	+		
$sliceDropY$	–	+	–	–	+

Table 2.2. Influence matrix summarizing findings from design space exploration. + indicates that the design variable and performance metric are positively related while a – indicates the opposite. No consistent or strong relationship was found for those left empty.

Each performance metric can be considered as either part of an objective function or used to define a constraint. Identifying the desired performance of the magnet when beginning the design process is essential to ultimately identify a suitable design. For example, an application aimed at interrogating the subcutaneous fat must produce a uniform region with a depth that exceeds a minimum value. An application interested in resolving features in space in the y direction may set a maximum threshold for the size in the y direction.

2.5 Magnet design, construction, and characterization

2.5.1 Final magnet design

These findings were utilized to design a magnet array as part of a portable clinical diagnostic sensor. The main functional requirements of the magnet required that the uniform field magnetize a sufficient volume of tissue at a useful depth at a high enough field to produce a high sensitivity measurement.

A field strength of approximately 0.2 Tesla was considered sufficient as that was similar to that of previous work in single-sided NMR for research purposes ^{77,86}. A depth of at least 15 mm was sought in order to ensure measurement beyond the dermis and subcutaneous layers ¹⁰². The ratio of size of the uniform field in the y and z direction was desired to be close to unity in order for location of the magnetized tissue to be more easily characterized. A volume of roughly 1 cm³ was sought for the uniform region when defined as having a field deviation of 1% from its center ⁹⁸. The volume of the magnet was limited to approximately 1000 cm³ to ensure portability as this magnet would weigh less than 9 kg. Minimum values for *gapX*, *gapY*, and *gapZ* were set based on manufacturing capabilities and the strength of the aluminum used for the housing.

The design strategy outlined above was followed for the given constraints. The dimensions of the final magnet design are shown in **Table 2.3**. The projected and actual characteristics of the magnet assembly are shown in **Table 2.4** demonstrating that the design process identified a suitable design. Attempting to produce a suitable design using the geometry shown in **Figure 2.1c** resulted in either a magnet too large for this application or with a lower field strength.

Design parameter	Value
------------------	-------

N_x	8
N_y	6
N_z	9
$gapX$	2.22 mm
$gapY$	0.64 mm
$gapZ$	1 mm
$sliceDropY$	11 mm

Table 2.3. Design parameters and optimal values of final magnet design.

	Goal	Simulated
Field strength [Tesla]	0.2	0.174
Field volume [mm ³], $\epsilon=1\%$	1000	1287
Field depth [mm]	15	16.2
Magnet volume [cm ³]	1000	884

Table 2.4. Projected and actual characteristics of designed Unilateral Linear Halbach magnet.

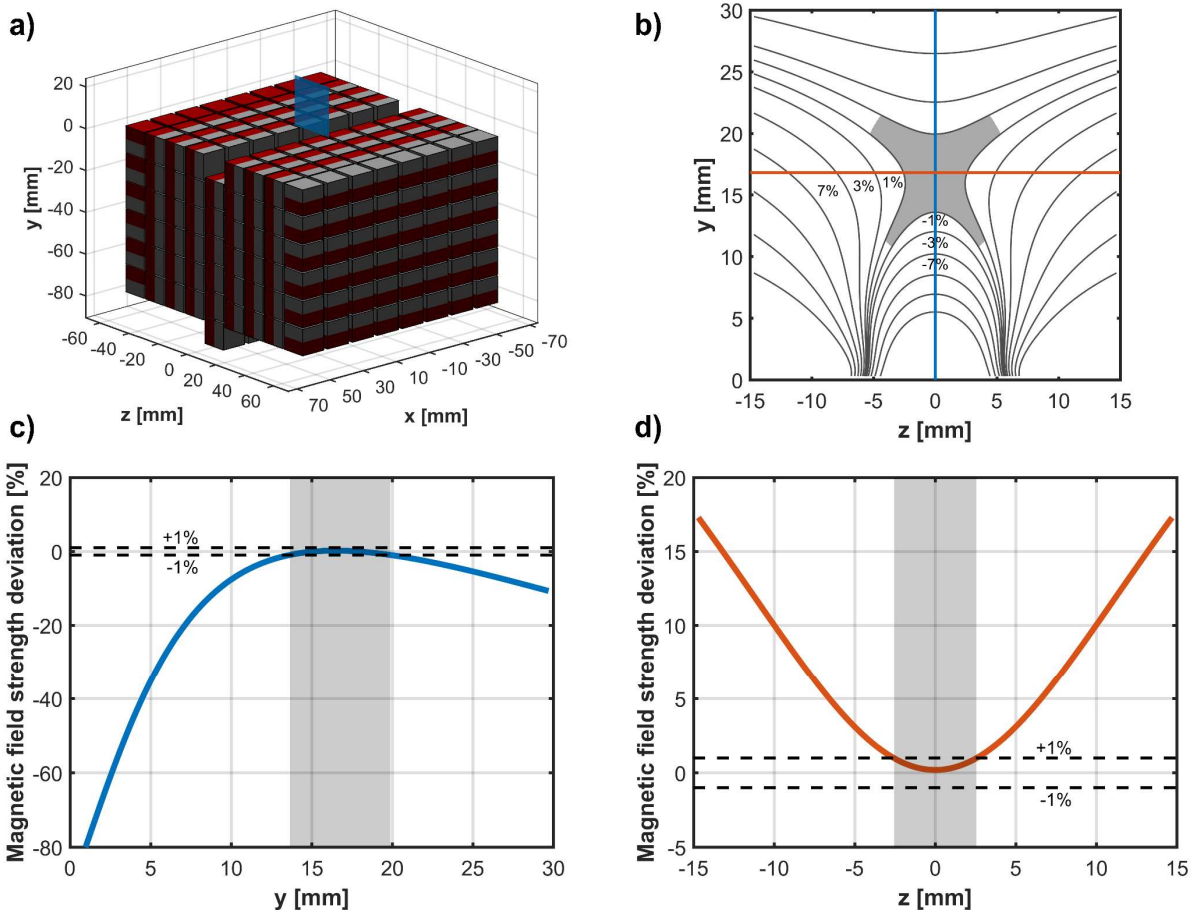


Figure 2.4. Field characterization of final magnet design. a) Illustration of the final magnet design. Red and grey shading indicates positive and negative poles, respectively. b) Simulated field profile directly above the center of the magnet, indicated by the blue plane shown in (a). Shaded region indicates predicted sensitive region assuming a transceiver coil sensitive to a region approximately 10 mm wide with a bandwidth of $\pm 1\%$. **c-d)** Magnetic field strength deviation from B_0 along y-axis and z-axis, respectively, through the center of the uniform region. Shaded regions correspond to $\pm 1\%$ deviation from B_0 .

2.5.2 Magnet construction

The magnet assembly was constructed with custom fabricated 12.7 mm (0.5 inch) cube, grade N52 neodymium magnets (Viona Magnetics, Hicksville, NY) manufactured with a dimensional tolerance of 50.8 μm (0.002 inch). The neodymium magnets are in an unstable, high energy state when placed into the desired configuration. Therefore, an aluminum housing (Proto Labs, Maple Plain, MN) capable of restraining the individual magnets was necessary. Further, the

housing needed to ensure safe insertion of magnets without experiencing unexpected or intractable forces from adjacent magnets. A modular design strategy was chosen which involved nine fixtures, or slices, each containing 48 magnets placed face to face after the magnets were inserted into their pockets. Renderings of a single slice and the entire assembly are shown in **Figure 2.5a** and **Figure 2.5b**, respectively.

a)



b)



Figure 2.5. Renderings of magnet assembly. Renderings of a) a single aluminum fixture and b) all aluminum slices for the magnet assembly. For illustrative purposes, a single magnet is placed in the first row, a single row has its aluminum cover in place, and a single brass screw is fastening the cover on the right. Each square pocket has a side length of 12.7 mm.

2.5.3 Magnet characterization

The final magnet assembly exhibited a field profile with a shape that very closely matched the prediction from numerical simulations as shown in **Figure 2.6**. The field profile was measured by scanning a hall probe (HMMT-6J04-VR, Lake Shore Cryotronics) connected to a gaussmeter (Model 475 DSP Gaussmeter) through a grid with 150 μm spacing. The field strength was measured at 0.17 Tesla while the simulated field strength, using measured values of remanence and relative permeability for the permanent magnets, was 0.174 Tesla. This discrepancy can likely be explained by variations between magnets and imperfections in magnet assembly.

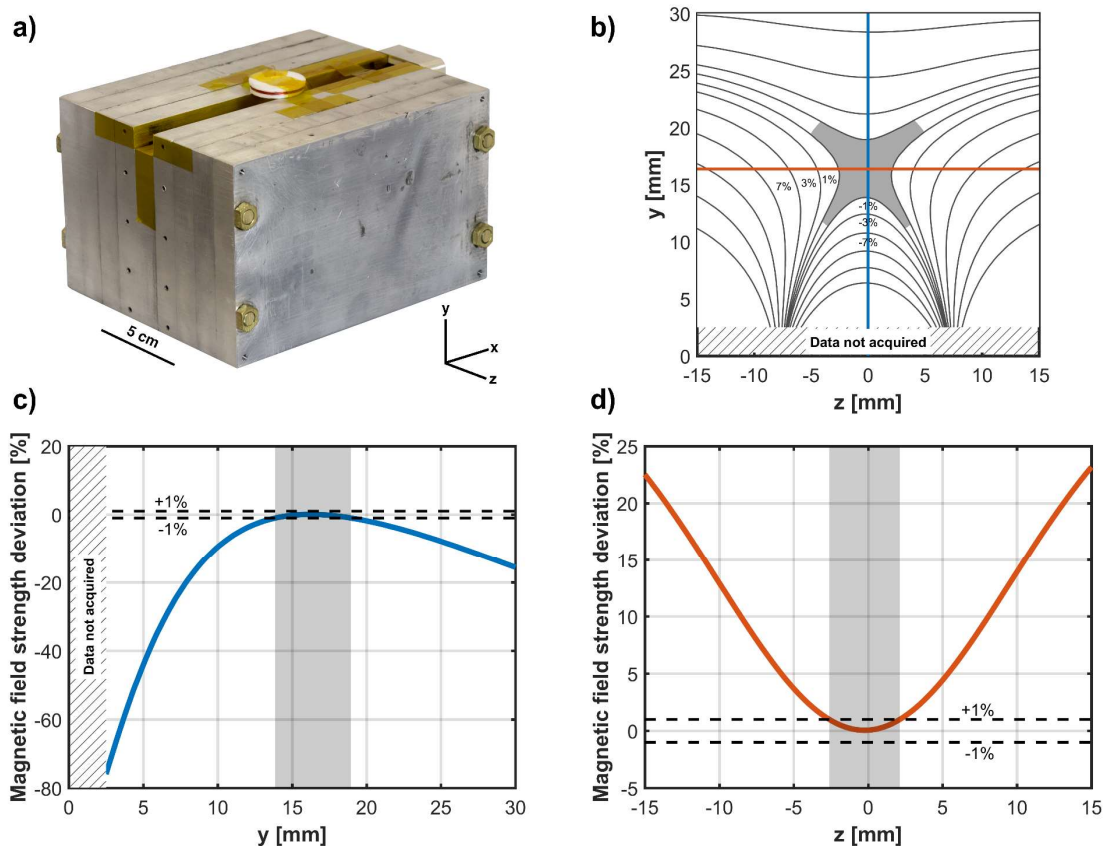


Figure 2.6. Experimental field characterization of final magnet design. **a)** Constructed magnet with RF matching circuit and solenoidal transceiver coil. **b)** Measured field profile directed above center of magnet. Shaded region indicates predicted sensitive region assuming a transceiver coil sensitive to a region approximately 10 mm wide with a bandwidth of $\pm 1\%$. **c-d)** Magnetic field strength deviation from B_0 along y-axis and z-axis, respectively, through the center of the uniform region. Shaded regions correspond to $\pm 1\%$ deviation from B_0 .

2.6 Robustness to variability in magnetization strength

A primary advantage conferred by constructing the magnet array from many small discrete magnets rather than fewer larger magnets is robustness to inter-magnet variability. The magnetization of each magnet is dependent on the manufacturing process. Variations can arise due to fluctuations in environmental conditions during sintering and magnetization steps or from differences in the purity of raw materials. Achieving precise tolerances can be a substantial driver of cost.

We assess the tradeoff between working with larger magnets that fill the air gaps with magnetic material versus smaller magnets, which reduce the effects of variability. Starting with the final design (**Table 2.3** and **Figure 2.4**), two additional magnets were simulated. The first was created where slices or groups of slices were replaced with a single large magnet with homogeneous magnetization. Each slice on the end and the middle slice were replaced with a single magnet. The second through fourth and the sixth through eight slices were each replaced with a single magnet. This resulted in a magnet design composed of five magnets. In order to facilitate a direct comparison, the size of these magnets were optimized until the uniform region was approximately identical to that produced by the original magnet. The largest magnets in this design were simulated as three identical magnets in order to simplify the simulation. This also allowed a gap between the magnets to be adjusted to better match the field profile to that of the original magnet. This configuration is shown in **Figure 2.7**.

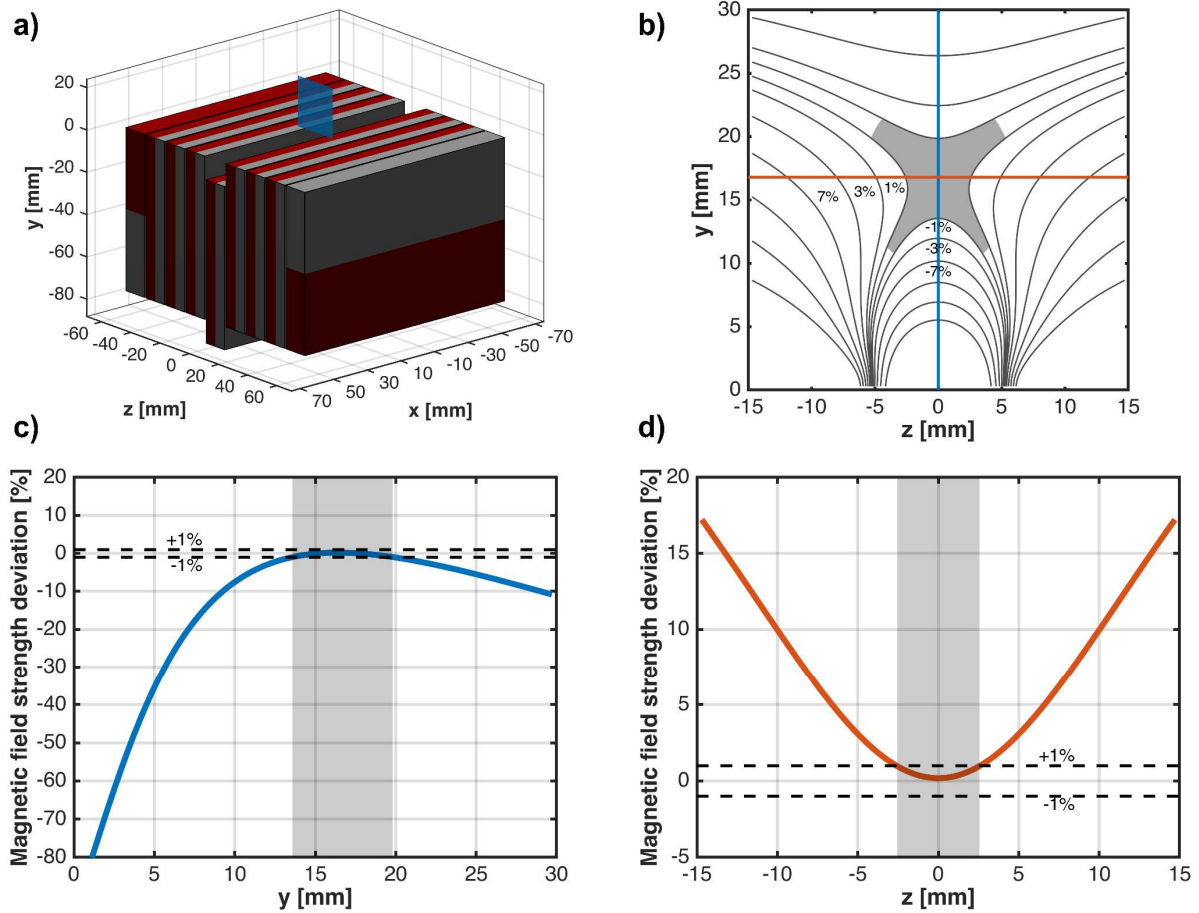


Figure 2.7. Magnet design without gaps and large magnets. **a)** Illustration of the magnet design without gaps comprising 9 large magnets. Red and grey shading indicates positive and negative poles, respectively. **b)** Simulated field profile directly above the center of the magnet, indicated by the blue plane shown in (a). Shaded region indicates predicted sensitive region assuming a transceiver coil sensitive to a region approximately 10 mm wide with a bandwidth of $\pm 1\%$. **c-d)** Magnetic field strength deviation from B_0 along y-axis and z-axis, respectively, through the center of the uniform region. Shaded regions correspond to $\pm 1\%$ deviation from B_0 .

The second design was created by simply doubling the number of magnets in each direction while halving each gap. This magnet, comprising 3456 unique 0.25-inch magnets, provides a more thorough understanding of how a large number of magnets can improve robustness to inter-magnet variability. This configuration is shown in **Figure 2.8**.

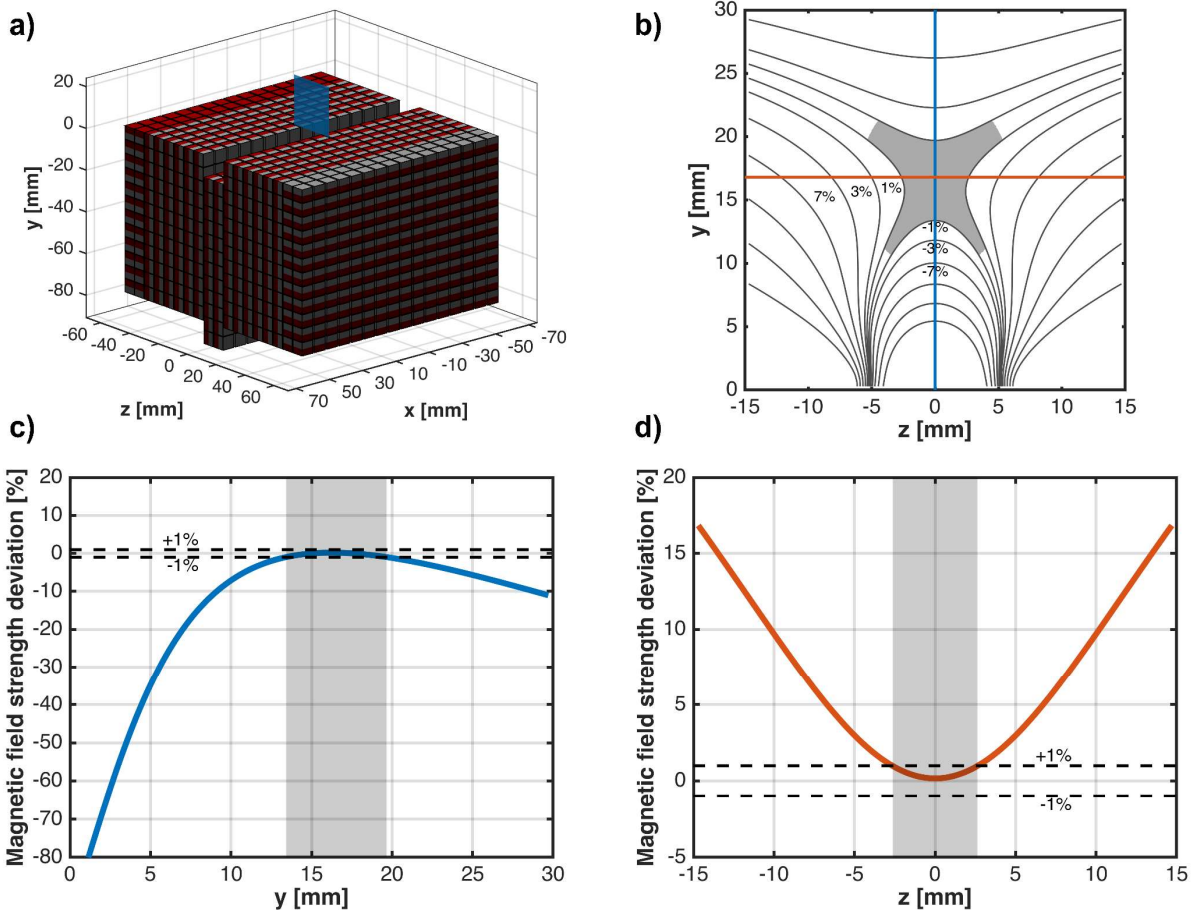


Figure 2.8. Magnet design with 0.25-inch magnets. **a)** Illustration of the magnet design comprising 3456 0.25-inch magnets. Red and grey shading indicates positive and negative poles, respectively. **b)** Simulated field profile directly above the center of the magnet, indicated by the blue plane shown in (a). Shaded region indicates predicted sensitive region assuming a transceiver coil sensitive to a region approximately 10 mm wide with a bandwidth of $\pm 1\%$. **c-d)** Magnetic field strength deviation from B_0 along y-axis and z-axis, respectively, through the center of the uniform region. Shaded regions correspond to $\pm 1\%$ deviation from B_0 .

A series of simulations were performed comparing the original magnet array against both the array comprising larger magnets and the array with many smaller magnets. The magnetization of each of the individual magnets was sampled from a uniform distribution with a range of 4% and $\pm 8\%$ of the original remanence to simulate inter-magnet variability. Each geometry was simulated 16 times for each magnetization tolerance value and the field profiles then assessed. The results are shown in **Table 2.5**.

Magnet design	Relative tolerance of magnetization	B_0	$posY$	$sizeX$	$sizeY$	$sizeZ$
5 large magnets	$\pm 4\%$	$\pm 2.3\%$	$\pm 2.3\%$	$\pm 10\%$	$\pm 3.1\%$	$\pm 3.4\%$
	$\pm 8\%$	$\pm 2.7\%$	$\pm 4.3\%$	$\pm 32.2\%$	$\pm 15.7\%$	$\pm 14.2\%$
Original magnet: 432 0.5" magnets	$\pm 4\%$	$\pm 0.5\%$	$\pm 0.7\%$	$\pm 1.2\%$	$\pm 0.8\%$	$\pm 2.3\%$
	$\pm 8\%$	$\pm 1\%$	$\pm 1.4\%$	$\pm 1.2\%$	$\pm 1.6\%$	$\pm 4.6\%$
3456 very small 0.25" magnets	$\pm 4\%$	$\pm 0.1\%$	$\pm 0.2\%$	$\pm 1.2\%$	$\pm 0.8\%$	$\pm 1.1\%$
	$\pm 8\%$	$\pm 0.2\%$	$\pm 0.2\%$	$\pm 1.2\%$	$\pm 0.8\%$	$\pm 2.1\%$

Table 2.5. Performance comparison of magnet design. Performance of the original magnet array (432 small magnets), a magnet array with fewer magnets (5 large magnets), and a magnet array with 3456 small magnets with $\pm 4\%$ and $\pm 8\%$ inter-magnet variability. For each performance metric, the range of variation around the normalized mean is reported. The magnet arrays with increased numbers of magnets are more robust to variability across every metric.

The magnet arrays comprising smaller magnets consistently demonstrate smaller ranges of variation for each performance metric. These trends are true for smaller and larger relative tolerances of magnetization (4% and 8%). The difference in range is quite significant in some cases such as with $sizeY$ and $sizeZ$. The unpredictability of the performance of a magnet array made up of a few larger magnets may negatively affect other aspects of the sensor design, such as the RF coil. These results are more pronounced at larger magnetization tolerances. This suggests that a design comprising many smaller discrete magnets offers an effective means to improve the cost effectiveness and field uniformity of Unilateral Linear Halbach magnets.

2.7 Multi objective optimization of magnet performance

2.7.1 Background on Pareto optimality

The concept of Pareto optimality defines a framework to perform optimization over a design space with multiple criteria. A magnet design is said to be Pareto optimal if there exists no other design which improves upon one performance criterion without compromising at least one other criterion. The Pareto frontier defines the set of these solutions where each is Pareto optimal. A designer can use the Pareto frontier to constrain the process of identifying a solution.

2.7.2 Design space exploration guided by Pareto optimality

We searched for Pareto optimal solutions for magnets below a threshold magnet volume ($\sim 1000 \text{ cm}^3$) at various B_0 field strengths. For simplicity, the two performance criteria were 1) the volume of the uniform region and 2) the depth of the uniform region from the surface of the magnet. Simulations began by varying each parameter individually with the starting point set as the design introduced in **Table 2.3**. The Pareto optimal points were then identified for each magnetic field strength of interest. A random subset was selected as initial points and then candidate magnet designs generated by random perturbation from these starting points. This process of generating candidate designs based on the Pareto optimal set was repeated for a total of 12,000 simulations.

2.7.3 Results

The results of the design space exploration guided by Pareto optimality for a set of field strengths of interest are shown in **Figure 2.9**. It is immediately evident that there is a tradeoff between field strength, depth, and field volume. This demonstrates the wide applicability of the Unilateral Linear Halbach design for applications with varying requirements for measurement depth, uniform region volume, and field strength.

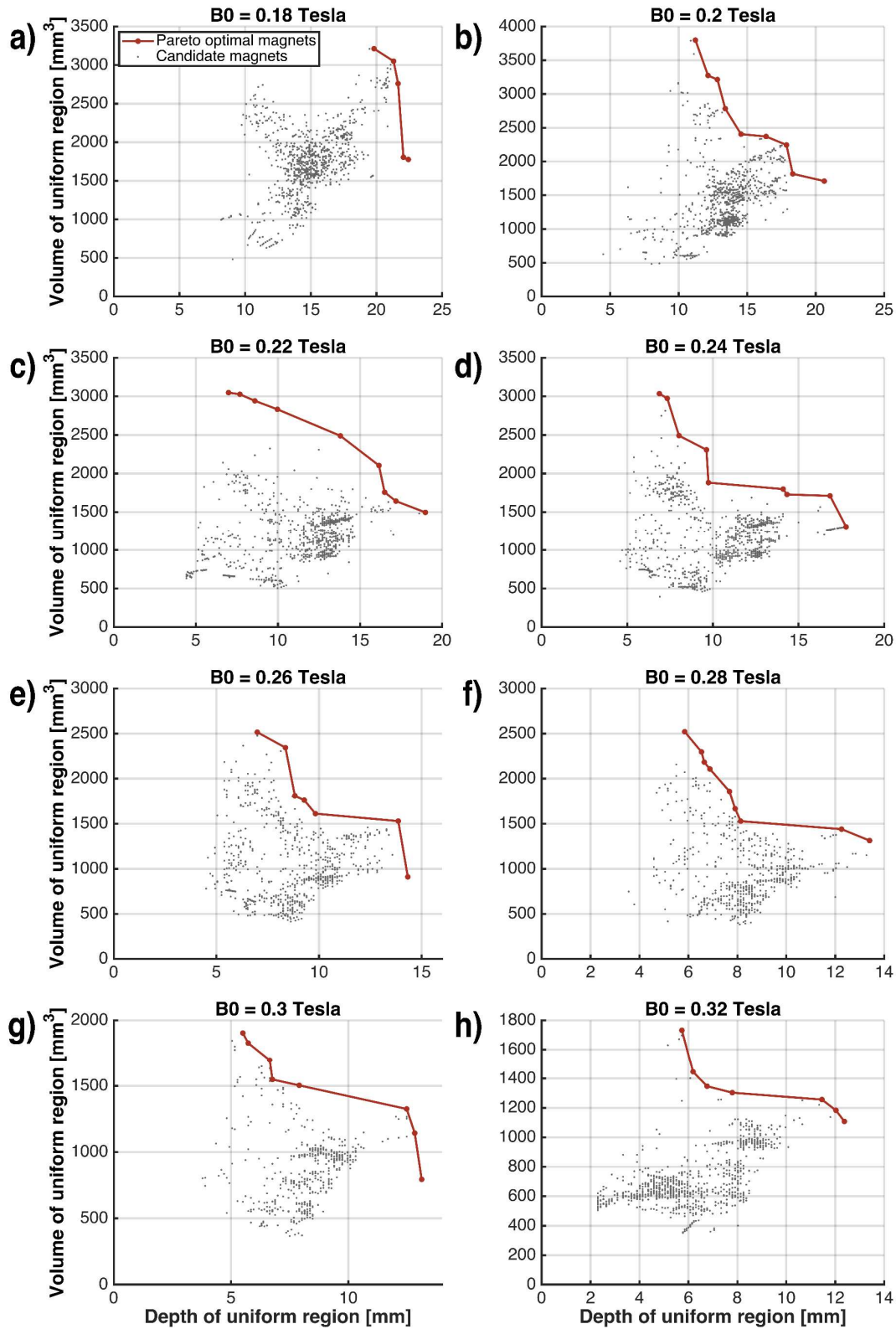


Figure 2.9. A subset of Pareto optimal magnets and other candidate magnets indicates the tradeoff between field strength, depth, and field volume. Each panel (a-h) shows the set of candidate magnets and Pareto optimal magnets as evaluated based on the two criteria of depth and volume of

uniform region having fields strengths equal to 0.18, 0.20, 0.22, 0.24, 0.26, 0.28, 0.30, and 0.32 Tesla, respectively.

2.8 Discussion

Unilateral NMR provides a unique measurement technique with potential for use across many applications, including medical diagnostics. Each application of this technology will likely require a unique magnet design to achieve the necessary depth of measurement and sensitivity within specified physical constraints. The Unilateral Linear Halbach magnet design proposed here offers remote, high field, low gradient homogenous regions for portable single-sided NMR. This approach offers a tunable design framework to efficiently produce sweet spot regions using an array of permanent magnets. The magnetic field produced by this design is aligned parallel to the surface of the sensor, allowing for the use of a standard, solenoid transceiver coil.

One limitation of this approach is that the physical characteristics of the sample and geometry of the RF probe were not considered during the design process. The probe could then be designed in conjunction with the magnet to enable more effective utilization of the uniform region of the magnetic field. Shaping the RF field profile to match that of the static magnetic field could enable greater sensitivity and a larger sensitive region ¹⁰³.

Rather than optimizing for the dimensions and strength of the magnetic field, a Bloch simulation would allow the ultimate sensitivity of the sensors to be used as the optimization criteria. This would simplify the design process as the multi-objective optimization problem would be reformulated more straightforwardly. On the other hand, the number of design parameters would grow as the geometry of the coil must also be optimized over. Further, knowledge of the sample (e.g. spin diffusivity) would be required as it affects the parameters of this Bloch simulation.

Sweet spot magnets provide a unique approach towards single-sided NMR as the relatively large and homogeneous field enables rapid, high-bandwidth measurements. The influence matrix produced from simulations builds a framework for future magnet designs. Our experimental demonstration closely matches numerical models indicating the effectiveness and simplicity of both our approach and this design. Readily available, low-cost permanent neodymium magnets can be used to construct single-sided NMR systems with this magnet design framework.

This page intentionally left blank

Chapter 3

Design and characterization of portable MR sensor for remote, multicomponent T2 relaxometry

3.1 Introduction

A portable MR sensor has the potential to enable the identification of localized shifts in tissue fluid distribution. This can inform a diagnosis of imbalances in systemic fluid volume status across a variety of diseases. We designed a new portable MR sensor capable of performing multicomponent T2 relaxometry measurements within a remote region located distal from the surface of the sensor.

Prior efforts in single sided MR sensors for medical applications have traditionally utilized sensors with a high gradient static magnetic field. This limits both the spatial extent of the sensitive region and the sensitivity of the system.

In this work, we utilize the previously described Unilateral Linear Halbach magnet array geometry to achieve a high sensitivity, remote, sweet spot static magnetic field. This magnet geometry allows for a highly tunable magnetic field strength and geometry that allows for an application specific design of the magnet to be realized.

3.2 Portable MR sensor design

We designed a portable magnetic resonance sensor capable of measuring the fluid distribution within tissue via multicomponent T2 relaxometry (**Figure 3.1a**). This sensor was designed and constructed with a permanent magnet array to generate a static magnetic field (B_0) based on the Unilateral Linear Halbach array (**Figure 3.1b-c**)¹⁰⁴. This sweet spot magnet design enables high sensitivity measurements over a large uniform region compared to more commonly used high gradient designs⁸⁵.

Permanent, rare earth magnets provide a means to generate a static magnetic field while also allowing for cost effectiveness, low maintenance, minimal power requirements, and portability compared to the more traditional superconducting magnets found in MRI. Furthermore, the magnetic field is parallel to the surface of the sensor allowing for the use of a standard radiofrequency (RF) transceiver coil in order to maximize sensitivity¹⁰⁴.

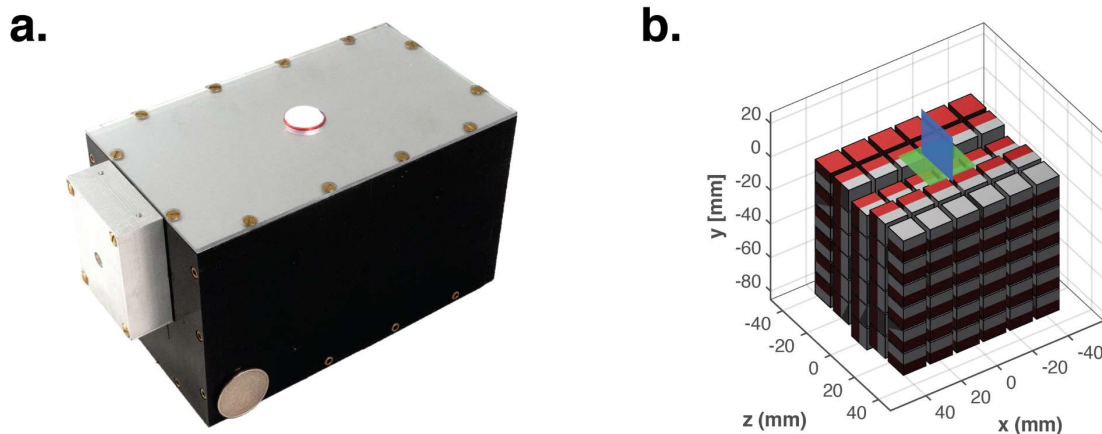


Figure 3.1. Portable MR sensor. **a)** Fully assembled sensor with RF matching circuit and solenoidal transceiver coil. **b)** Illustration of Unilateral Linear Halbach permanent magnet array design for sensor. Red and grey shading indicates positive and negative poles, respectively, of each magnet.

The portable MR sensor was designed with the goal of achieving high sensitivity measurements remote from the surface of the sensor. The Unilateral Linear Halbach magnet geometry was utilized with an array of cube permanent magnets¹⁰⁴. Finite element analysis with COMSOL Multiphysics (Burlington, MA) was

utilized to simulate the magnetic field profile of the magnet array. The magnet was parameterized by seven design parameters in order to constrain the dimensionality of the optimization problem as previously detailed ¹⁰⁴. The final values used for each parameter are as follows: N_x 6, N_y 6, N_z 5, gapX 2.23 mm, gapY 0.76 mm, gapZ 2.54 mm, and sliceDropY 5.1 mm.

The permanent magnets are custom fabricated 12.7 mm (0.5 inch) cube, grade N52 neodymium magnets (Viona Magnetics, Hicksville, NY) manufactured with a dimensional tolerance of 50.8 μm (0.002 inch). The magnets are contained within an aluminum assembly manufactured with a dimensional tolerance of 0.127 mm (0.005 inch) (Proto Labs, Maple Plain, MN). The RF transceiver coil is a 8-turn solenoid wound around a cylindrical PTFE bobbin with a diameter of 16 mm. The coil geometry was selected to maximize the sensitivity of the sensor. A narrowband “L” impedance matching network was placed approximately 8 cm from the transceiver coil. The matching network consists of two high Q, tunable capacitors (Johanson Manufacturing) (**Figure 3.2a**). The first capacitor is placed in parallel with the transceiver coil and the other is placed in series with this parallel circuit. The matching circuit provides a precisely tunable impedance match at the Larmor frequency of the sensor (**Figure 3.2b**).

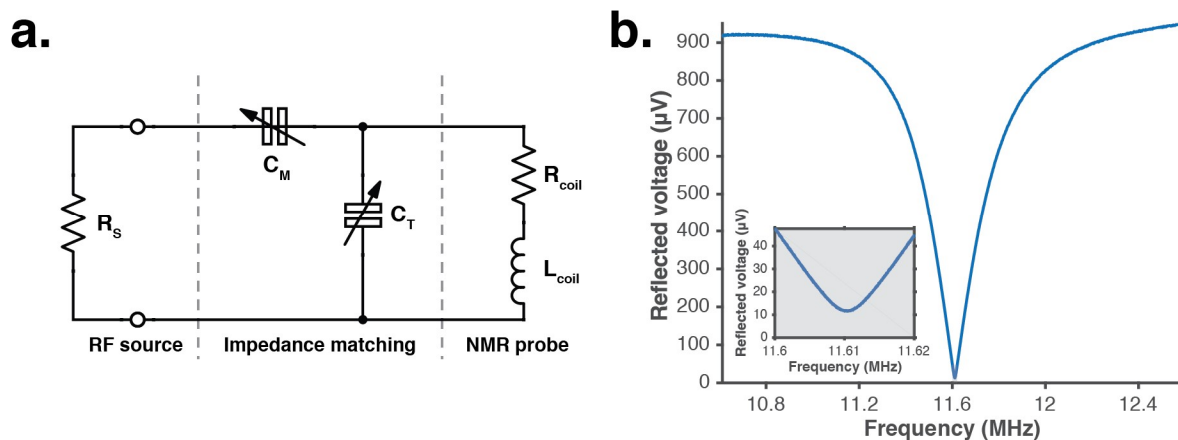


Figure 3.2. Impedance matching circuit design and performance characterization. **a)** RF impedance matching circuit schematic using an “L” topology. **b)** Reflected signal versus frequency when tuned

to a single operating frequency. Inset highlights the ability to reach a very low reflection coefficient at a desired frequency.

3.3 Static magnetic field characterization

The magnet produces a uniform region with a magnetic field strength of 0.28 Tesla located approximately 2 to 7 mm from the surface of the sensor as modeled by field simulations and experimentally confirmed with an acquired field profile (**Figure 3.3**).

The static magnetic field profile of the portable MR sensor was measured by scanning a hall probe (HMMT-6J04-VR, Lake Shore Cryotronics) connected to a gaussmeter (Model 475 DSP Gaussmeter) through a three-dimensional grid with 1 mm spacing. The uniform region was identified as the contiguous region which when excited with a 1% RF bandwidth would produce the strongest MR signal ¹⁰⁴.

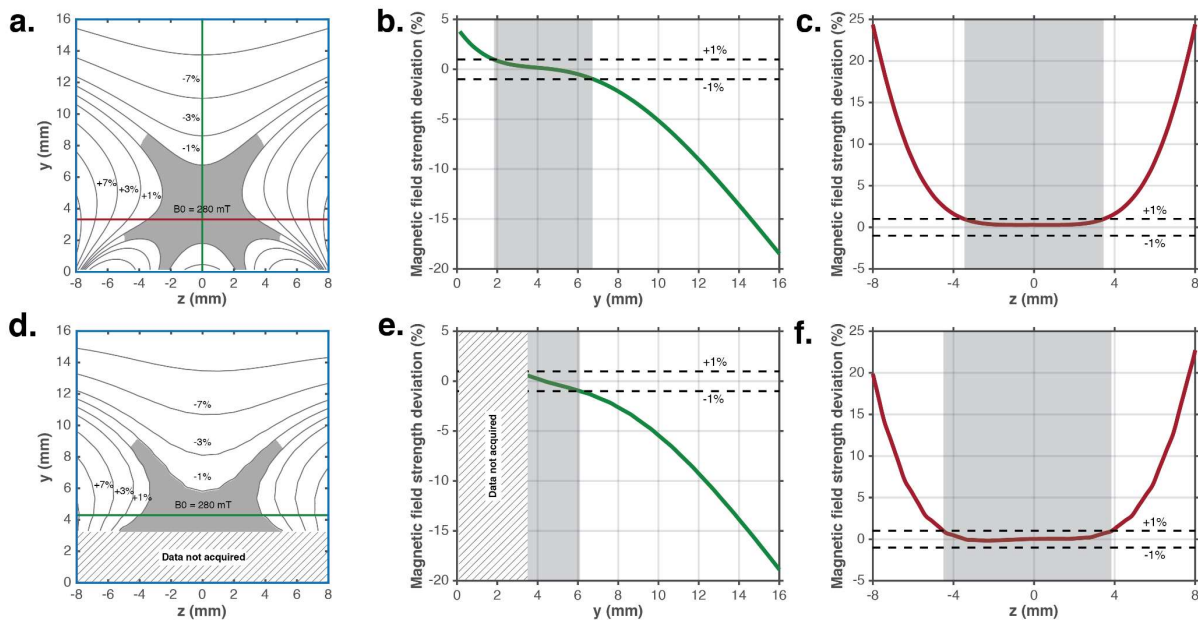


Figure 3.3. Static magnetic field profile characterization of portable MR sensor. **a,d**) Simulated field profile directly above the center of the magnet. Shaded region indicates predicted sensitive region assuming a transceiver coil sensitive to a region approximately 10mm wide with a bandwidth of $\pm 1\%$. **b-c**) simulated and **e-f**) measured magnetic field strength deviation from B_0 along y-axis and z-axis, respectively, through the center of uniform region. Shaded regions correspond to $\pm 1\%$ deviation from B_0 .

3.4 Sensitivity profile characterization

The sensitivity of the system was characterized by measuring the relative signal amplitude from a sample scanned through the sensitive region. The sensor is sensitive towards a region located directly above the RF coil spanning a volume of $12 \times 5 \times 2$ mm (**Figure 3.4**). This allows localization of the measurement towards skeletal muscle tissue while reducing any confounding signal from subcutaneous tissue ⁷⁸.

The two-dimensional sensitivity profiles were determined by measuring the relative signal strength produced by a 2 mm spherical sample of aqueous CuSO_4 solution scanned through planes perpendicular to the surface of the sensor. The relative signal strength was estimated from each scan as the relative amplitude of the peak corresponding to the spherical sample. This isolated the signal produced by the aqueous sample from background signal produced by the sensor.

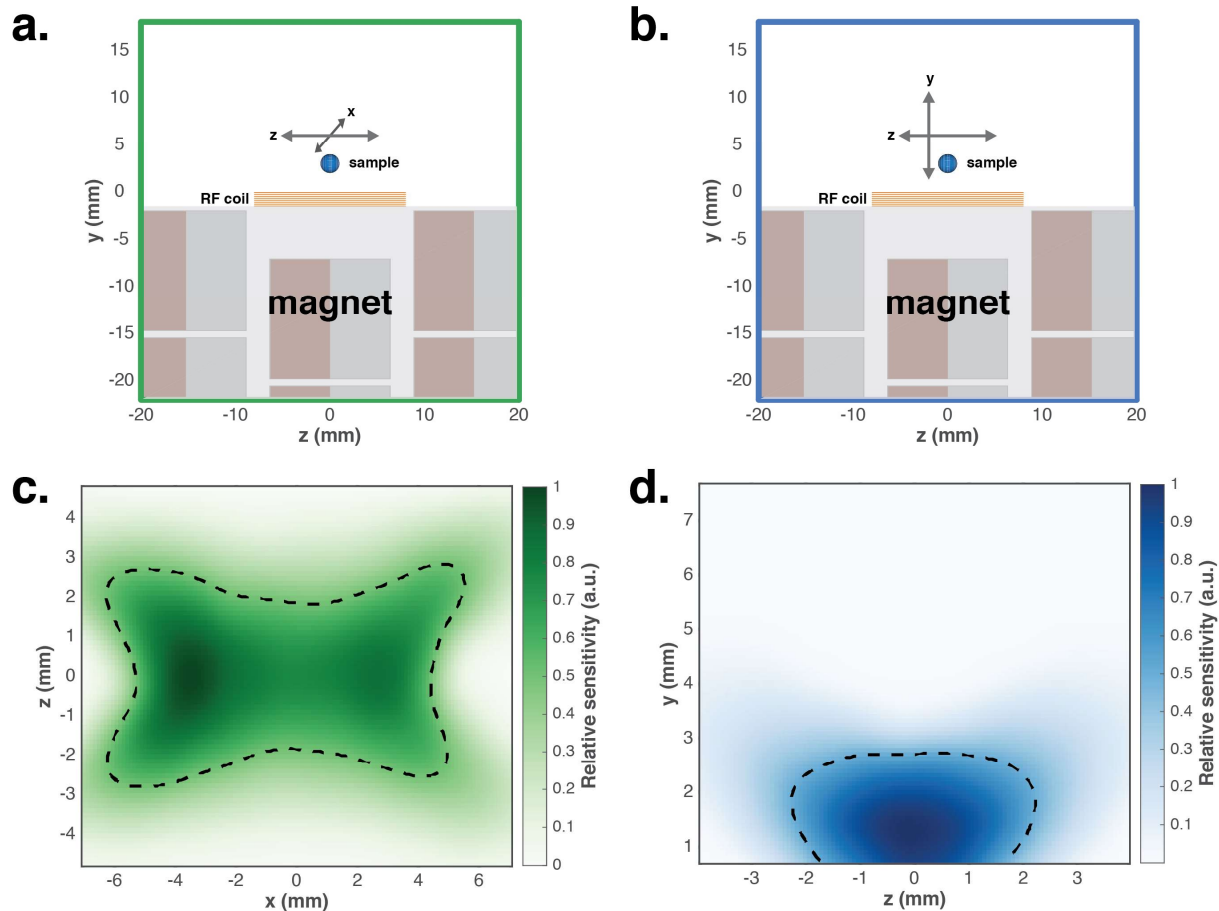


Figure 3.4. Illustration of sensitivity profile characterization of portable MR sensor. **a-b)** Experimental schematic for MR sensor sensitivity profiles along **a)** xz-plane and **b)** yz-plane. A 2 mm spherical bulb of CuSO_4 aqueous solution was scanned across the measurement plane. The amplitude of the peak corresponding to the solution indicated the signal strength originating from the contents of the bulb. **c-d)** Relative sensitivity of sensor across the **c)** xz-plane and the **d)** yz-plane indicates a $12 \times 5 \times 2$ mm sensitive region. Dashed lines indicate 50% relative sensitivity from the peak of the measurement region.

3.5 Single component T2 relaxometry

The portable MR sensor reliably demonstrates the linear relationship between transverse (T_2) relaxation rate and concentration of paramagnetic species (CuSO_4) in aqueous solution, a representative synthetic tissue phantom, using a CPMG (Carr-Purcell-Meiboom-Gill) pulse sequence for acquisition ($n = 19$, $R^2 = 0.997$, $p < 1 \times 10^{-22}$, statistics by t test) (**Figure 3.5a**). There is a linear relationship between sample concentration and estimated relaxation rate across a wide range of

concentrations per Bland-Altman analysis ($n = 19$, mean of differences = 0.0008, 95% confidence interval = -0.008 to 0.009, $p = 0.21$, statistics by significance of Spearman rank correlation of means and differences) (**Figure 3.5b**).

The calibration curves of portable MR sensor R2 vs. paramagnetic species concentration were acquired as follows: Aqueous CuSO₄ solutions were prepared at the following concentrations: 0 mM, 1.17 mM, 1.22 mM, 1.47 mM, 1.87 mM, 2.55 mM, 3.11 mM, 11.1 mM, 12.5 mM, 13.2 mM, 15.2 mM, 16 mM, 17.9 mM, 20.3 mM, 23.4 mM, 25.3 mM, 27.6 mM, 30.4 mM, and 38 mM. Portable MR measurements were performed with the CPMG pulse sequence with 8192 echoes, an echo time of 65 μ s, a repetition time of 1032.5 ms, an RF excitation frequency of 11.66 MHz, a pulse duration of 12 μ s, an acquisition bandwidth of 2 MHz (dwell time of 0.5 μ s), and 16 acquired points per echo with a Kea2 spectrometer (Magritek, Wellington, New Zealand).

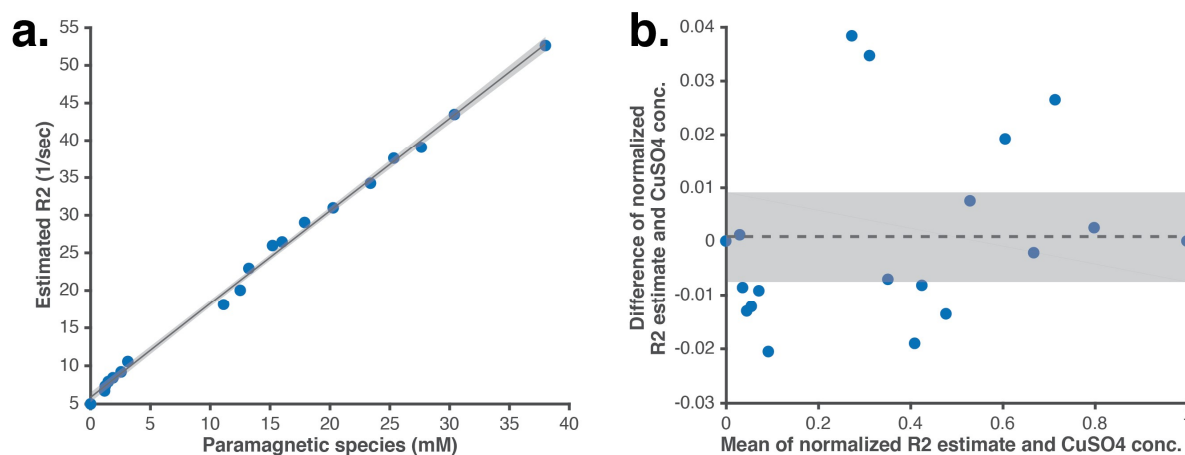


Figure 3.5. Linearity of paramagnetic species concentration versus relaxation rate from portable MR sensor. **a)** Linearity of R2 relaxometry measurements with portable MR sensor versus paramagnetic species concentration. Shaded region indicates the standard deviation of the error of the linear fit ($n = 19$, $R^2 = 0.997$, $p < 1 \times 10^{-22}$, statistics by t test). **b)** Bland-Altman analysis for linear fit. Residuals of linear fit for estimated relaxation rate do not show any trends dependent on paramagnetic species concentration. Residuals of a linear fit are approximately normally distributed ($n = 19$, $p = 0.768$, Lilliefors test for normality). Bland-Altman analysis indicates a linear relationship between sample concentration and estimated relaxation rate across a wide range of concentrations ($n = 19$, mean of differences = 0.0008, 95% confidence interval = -0.008 to 0.009, $p = 0.21$, statistics by significance of Spearman rank correlation of means and differences).

These results are validated against a gold-standard benchtop NMR spectrometer (minispec mq7.5, Bruker, USA) further demonstrating validity of our portable sensor (**Figure 3.6**). The estimated relaxation rates from the two MR systems are linearly related ($n = 19$, $R^2 = 0.996$, $p = 1 \times 10^{-12}$, statistics by t test). There is no bias in estimation of relaxation rates across a wide range of concentrations per Bland-Altman analysis indicating strong agreement between the two measurements ($n = 19$, mean of differences = -0.004 , 95% confidence interval = -0.012 to 0.004 , $p = 0.70$, statistics by significance of Spearman rank correlation of means and differences).

The data for the calibration curve from the benchtop NMR spectrometer were acquired via CPMG with 65535 echoes, an echo time of $426 \mu\text{s}$, a repetition time of 27.94 seconds, an RF excitation frequency of 19.95 MHz, an excitation pulse duration of $1.9 \mu\text{s}$, an inversion pulse duration of $3.8 \mu\text{s}$, an acquisition bandwidth of 1 MHz (dwell time of $3 \mu\text{s}$), and 1 acquired point per echo with a (minispec mq20, Bruker, USA). Relaxation times were extracted by fitting the decay curves with a monoexponential model.

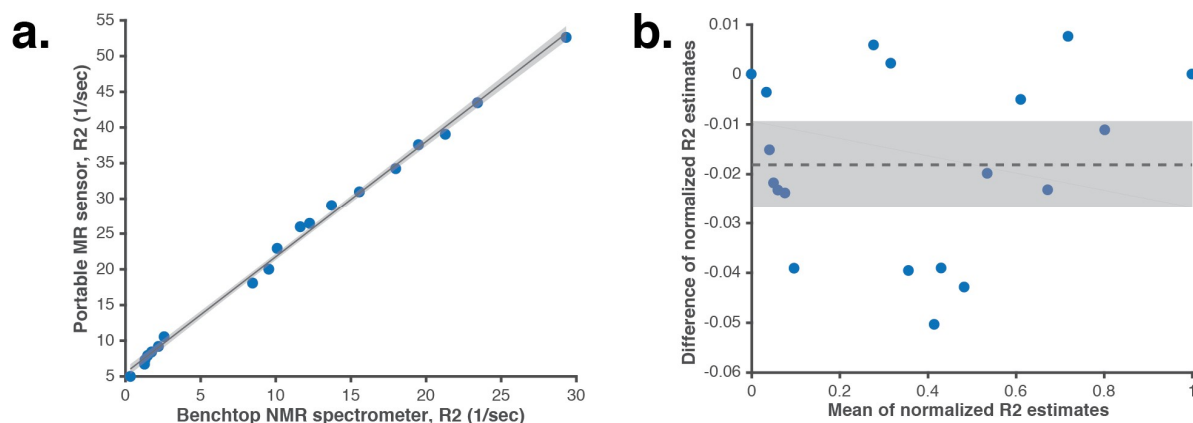


Figure 3.6. Validation of T2 relaxometry measurements from portable MR sensor with benchtop NMR spectrometer. **a)** The estimated relaxation rates from the two MR systems are linearly related ($n = 19$, $R^2 = 0.996$, $p = 1 \times 10^{-12}$, statistics by t test). Shaded region indicates the standard deviation of the error of the linear fit. Residuals of a linear fit between the relaxation rate estimates between the two MR systems are approximately normally distributed ($n = 19$, $p = 0.768$, Lilliefors test for normality). **b)** There is no bias in estimation of relaxation rates across a wide range of concentrations per Bland-Altman analysis indicating strong agreement between the two measurements ($n = 19$, mean of differences = -0.004 , 95% confidence interval = -0.012 to 0.004 , $p = 0.70$, statistics by significance of Spearman rank correlation of means and differences).

3.6 Multiexponential fitting

CPMG T2 decay curves were estimated as a multiexponential signal in order to extract relaxation times (τ_i) and relative amplitudes (A_i). When more than one point was collected for each echo, echo integrals were computed as the sum of the points sampled for each echo during CPMG. A general multicomponent exponential decay signal can be represented as:

$$\hat{y}(t, \mathbf{A}, \boldsymbol{\tau}) = \sum_{i=1}^N A_i * \exp(-t/\tau_i) \quad (4)$$

where $\hat{y}(t)$ is the estimated signal, N is the number of components, \mathbf{A} is a vector of amplitudes, and $\boldsymbol{\tau}$ is a vector of corresponding relaxation times. Two types of models were used to represent the multicomponent nature of these signals. The first optimizes over both the relaxation times and relative amplitudes. The optimal set of parameters is found by minimizing the L2-norm of the residuals between the estimated and the measured signal:

$$\mathbf{A}^{opt}, \boldsymbol{\tau}^{opt} = \underset{\mathbf{A}, \boldsymbol{\tau}}{\operatorname{argmin}} \|y(t) - \hat{y}(t)\|_2 \quad (5)$$

where $y(t)$ is the measured signal and $\|\cdot\|_2$ represents the L2-norm. This model allows discovery of the relaxation times of a multiexponential signal. The second model optimizes only over the relative amplitudes as the relaxation times are specified as parameters:

$$\mathbf{A}^{opt} = \underset{\mathbf{A}}{\operatorname{argmin}} \|y(t) - \hat{y}(t, \boldsymbol{\tau})\|_2 \quad (6)$$

This more constrained model allows the amplitudes to be estimated more accurately. 95% confidence intervals for each parameter were computed assuming an asymptotic normal distribution for each estimate. Signal to noise ratio (SNR)

was defined as the maximum magnitude value divided by the standard deviation of the noise. The noise distribution was estimated from the residuals of the fit.

3.7 Multicomponent T2 relaxometry

A heterogeneous synthetic tissue phantom consisting of two distinct compartments with unique T2 relaxation rates was measured using the portable MR sensor (**Figure 3.7a**). The heterogeneous synthetic tissue phantom was constructed from 30 glass capillary tubes (1 mm diameter) arranged in a tightly packed circular formation (**Figure 3.7a, inset**). Two equal sets of tubes were filled with the requisite concentrations of aqueous CuSO_4 solution to produce T2 relaxation times of 24 ms (29 mM) and 84 ms (5 mM). The tubes were arranged randomly.

Measurements were performed with the CPMG pulse sequence with 8192 echoes, an echo time of 65 μs , a repetition time of 1032.5 ms, an RF excitation frequency of 11.64 MHz, a pulse duration of 12 μs , an acquisition bandwidth of 2 MHz (dwell time of 0.5 μs), and 16 acquired points per echo with a Kea2 spectrometer (Magritek, Wellington, New Zealand).

Relaxation time constants and relative amplitudes of each fluid compartment can be accurately and reproducibly extracted from signals acquired by the MR sensor via T2 relaxometry (**Figure 3.7b-c**). Amplitudes were extracted by fitting the decay curves with a biexponential model. Repeated trials were performed to yield histograms of estimation error. This exemplifies the ability to accurately quantify fluid distribution across a heterogeneous sample via a single-sided portable MR sensor.

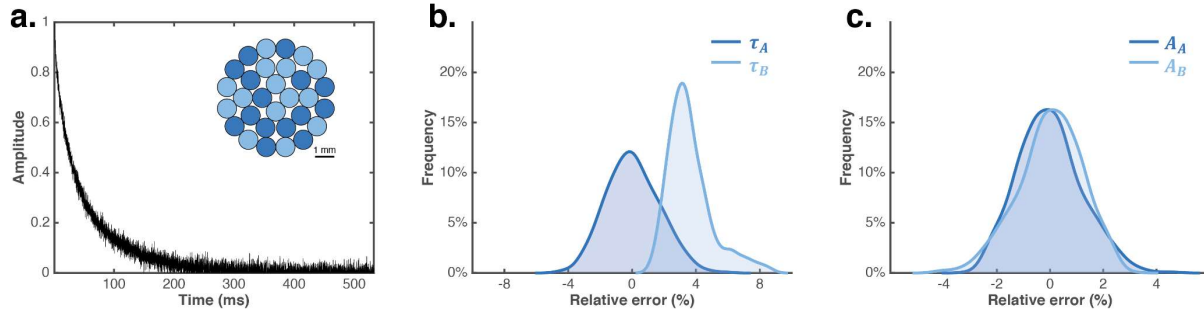


Figure 3.7. Multicomponent relaxometry with portable MR sensor. **a)** MR signal acquired with CPMG acquisition from a synthetic tissue phantom comprising equal parts fast (24 ms, dark blue) and slow (84 ms, light blue) fluid compartments. Inset illustrates cross section of phantom. **b-c)** Analysis of each component with a biexponential model demonstrates accurate identification and quantification of the decay rate (τ_A , τ_B) and relative amplitude (A_A , A_B) of each component. Repeated trials yield histograms of estimation error.

3.8 Discussion

The portable MR sensor offers many advantages over traditional MRI. Its miniature size and low power consumption, both realized through the use of permanent magnets rather than superconducting coils, offer a mobile platform capable of performing measurements across a wide range of environments including hospitals, outpatient facilities, sporting events, and military operations. The device is straightforward to operate as there is no need for any user controlled acquisition parameters. Furthermore, the interpretation of the measurement is fully automated in contrast to traditional MRI. The potential to perform these MR measurements without a trained operator or radiologist for image interpretation may increase accessibility of fluid volume status measurements. Finally, the measurement can be performed in a few minutes suggesting the potential for use as a real-time measure of fluid volume status.

Several enhancements to the portable MR sensor design and MR pulse sequences would improve measurement accuracy and reduce variability to enhance the potential for clinical translation. The relatively inhomogeneous field and imperfect refocusing pulse flip angle likely created stimulated echoes from additional coherence pathways during portable MR measurements. This can bias the

estimation of T2 and lead to overestimation of the T2 especially in tissues with a high T1 to T2 ratio ¹⁰⁵. The use of a pulse sequence with reduced stimulated echoes would allow direct comparison of relaxation times between different MR systems and a more thorough investigation of shifts in relaxation time with change in fluid volume status ¹⁰⁶.

Chapter 4

Identification of fluid depletion via MR measurements

4.1 Introduction

A portable, miniaturized magnetic resonance-based platform for the diagnosis of dehydration is demonstrated in this study of fluid depletion in mice. We show that multicomponent T2 relaxometry localized to the skeletal muscle, performed with a standard MRI system, is capable of quantifying fluid loss induced by dehydration in a mouse model. We further demonstrate that the portable MR system is capable of localizing this measurement towards skeletal muscle tissue in vivo. Finally, we assess the ability of multicomponent T2 relaxometry performed with this portable sensor to measure dehydration supporting the preliminary findings from our previous clinical study. This technology provides an original approach towards measuring fluid volume status through a direct measure of the underlying physiology. The work in this chapter was performed in collaboration with Chris J. Frangieh.

4.2 Mouse model of fluid loss induced by thermal dehydration

A mouse model of dehydration induced through exposure to elevated temperature and airflow combined with fluid restriction provided an appropriate model to

examine fluid shifts in the skeletal muscle (**Figure 4.1a-b**). Animal studies were approved by the Massachusetts Institute of Technology (MIT) Institutional Animal Care and Use Committee (protocol number 0716-045-19), and animals were cared for in the U.S. Department of Agriculture–inspected MIT Animal Facility under federal, state, local, and National Institutes of Health guidelines for animal care. Female Swiss Webster (CrI:CFW(SW)) mice were purchased from Charles River Laboratories. Mice underwent dehydration when 6–7 weeks old. Animals were provided *ad libitum* access to food and water for at least 72 hours prior to the start of experiments.

Dehydration induced by exposure to elevated temperatures preferentially depletes ECF over ICF⁵⁷. Body weight loss of between 4 and 11% was induced over 5 to 10 hours in experimental mice (**Figure 4.1c**). Each mouse was measured before and after dehydration with a magnetic resonance system (whole animal NMR, a standard MRI scanner, or our portable MR sensor) (**Figure 4.1a**). Mice undergoing dehydration were first weighed, measured with whole animal NMR and measured with MRI (or portable MR). Mice were then weighed periodically while exposed to dehydrating conditions. When weight loss reached at least 8% of initial body weight or the rate of weight loss decreased, the mice underwent a second course of MR measurements. Mice were weighed with a precision of 0.01 g at the start of each experiment, before and after any MR measurement, and at regular (approximately 30 min) intervals during the dehydration period. During dehydration, each mouse was housed individually in a clear plastic container placed inside a dark, 37 C, 15–20% relative humidity environment. A 96-well plate was placed in each container to contain urine and feces. Plates were weighed and replaced at regular (approximately 30 min) intervals. An axial fan (120 mm diameter, 2600 RPM, 110 CFM) was placed immediately adjacent to each container to increase airflow.

Control animals were provided access to food and water while at ambient environmental conditions. These control animals experienced a mean weight loss of 3% body weight during experiments despite no exposure to elevated temperature

and no restriction of food and water intake. This fluctuation in weight was likely due to voiding of urine and feces due to disruption of regular diurnal cycle and stress due to handling^{107–109}. We expect that these animals maintained euvolemia throughout the experiment due to their unrestricted access to food and water. When dehydration is induced in experimental animals, weight loss ranges from 7 to 14% of body weight. We compute an adjusted weight loss by subtracting 3% from measured weight loss to account for these losses. Adjusting for weight loss due to stress and handling allowed the study to correlate the change in MR signal with weight loss induced only by thermal dehydration.

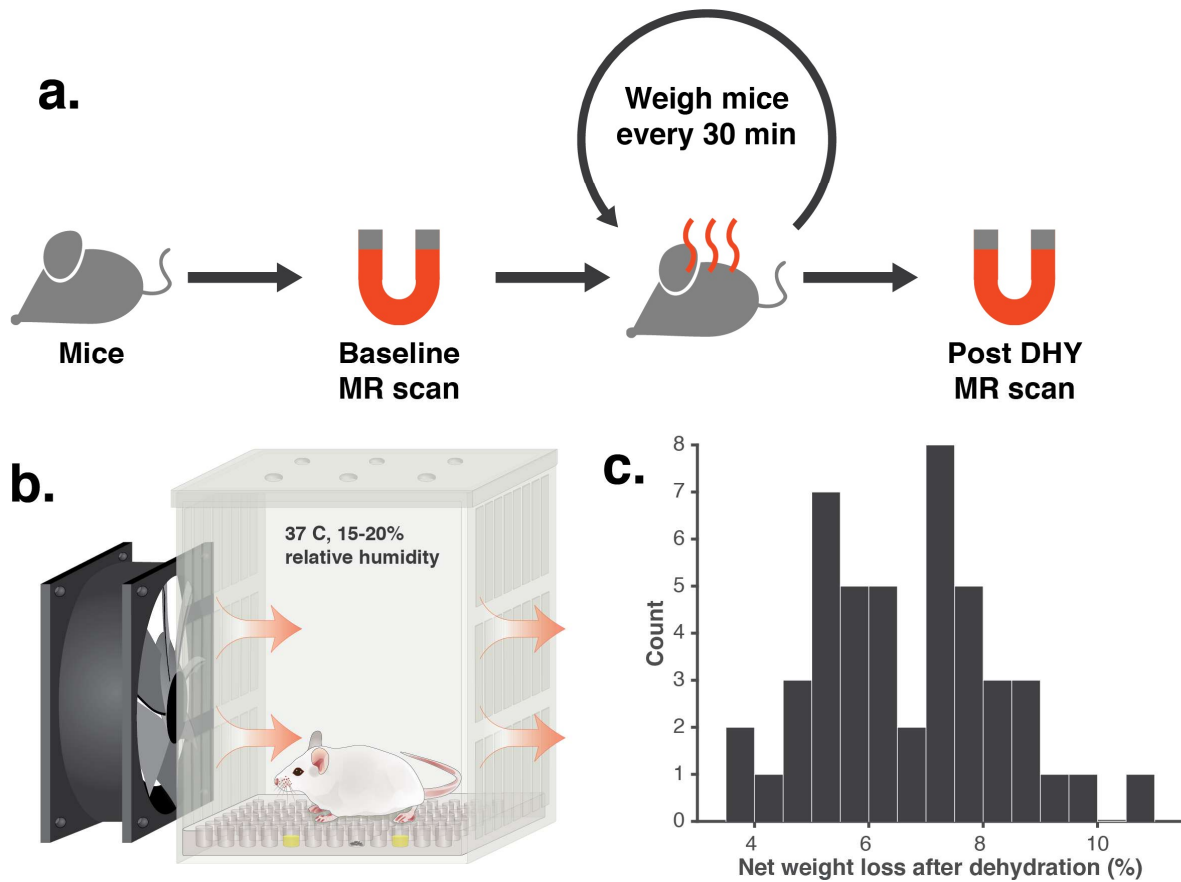


Figure 4.1 Mouse model of thermal dehydration. **a-b)** Schematic illustration of mouse thermal dehydration model. Mice were exposed to a 37 C, 15-20% relative humidity, and high airflow environment. Urine and feces were collected in a 96-well plate. **c)** Histogram of weight loss at the start of MR measurements.

4.3 Whole animal MR measurements

Whole animal multicomponent T2 relaxometry measurements performed via benchtop NMR relaxometry on each mouse before and after dehydration were used to validate the animal model and demonstrate the utility of a MR measurement to identify dehydration. Whole animal NMR measurements were performed using a 0.17 Tesla (7.5 MHz) benchtop time-domain relaxometer (LF50, BCA-Analyzer/minispec mq7.5, Bruker, USA). Measurements were performed with the CPMG pulse sequence with 21668 echoes, an echo time of 0.1 ms, a repetition time of 4 seconds, an RF excitation frequency of 7.5 MHz, an excitation pulse duration of 13.67 μ s, an inversion pulse duration of 27.6 μ s, 6 acquired points per echo, an acquisition bandwidth of 1 MHz (dwell time of 15 μ s), and 4 scan averages. Unanesthetized animals were each placed in a clear, plastic cylindrical (50 mm diameter) plastic tube. Animals were immobilized through the insertion of a PTFE plunger into the cylinder. Air was flowed through the cylinder for the duration of the scan.

The time domain NMR relaxometry signal shows a decrease in decay time (pre: 96.7 ms; post: 88.0 ms) after dehydration in a single animal (**Figure 4.2a**).

Multicomponent relaxometry allows examination of the relaxation time and relative volumes of distinct fluid compartments within the animal to be individually isolated and analyzed. The component corresponding primarily to lean muscle tissue was most responsive to fluid depletion (**Figure 4.2b**)^{70,110}. Thermal dehydration is known to induce a decrease in skeletal muscle volume as measured by MRI⁶¹.

The lean muscle tissue amplitude was nearly three times as important as the respective relaxation time in predicting weight loss when assessed via binary decision regression tree analysis (**Figure 4.2c**). The amplitude of the second component from whole animal MR measurements, corresponding to lean muscle tissue, was an approximately 2.8 times more important predictor of weight loss than the respective relaxation time. Predictor importance was calculated by estimating the change in mean squared error attributed to the inclusion of each

predictor in a binary regression decision tree. Error bars indicate standard error of the mean across all models generated via 10-fold cross validation.

Multicomponent T2 relaxometry can measure the decrease in fluid volume attributed to the lean muscle compartment due to dehydration.

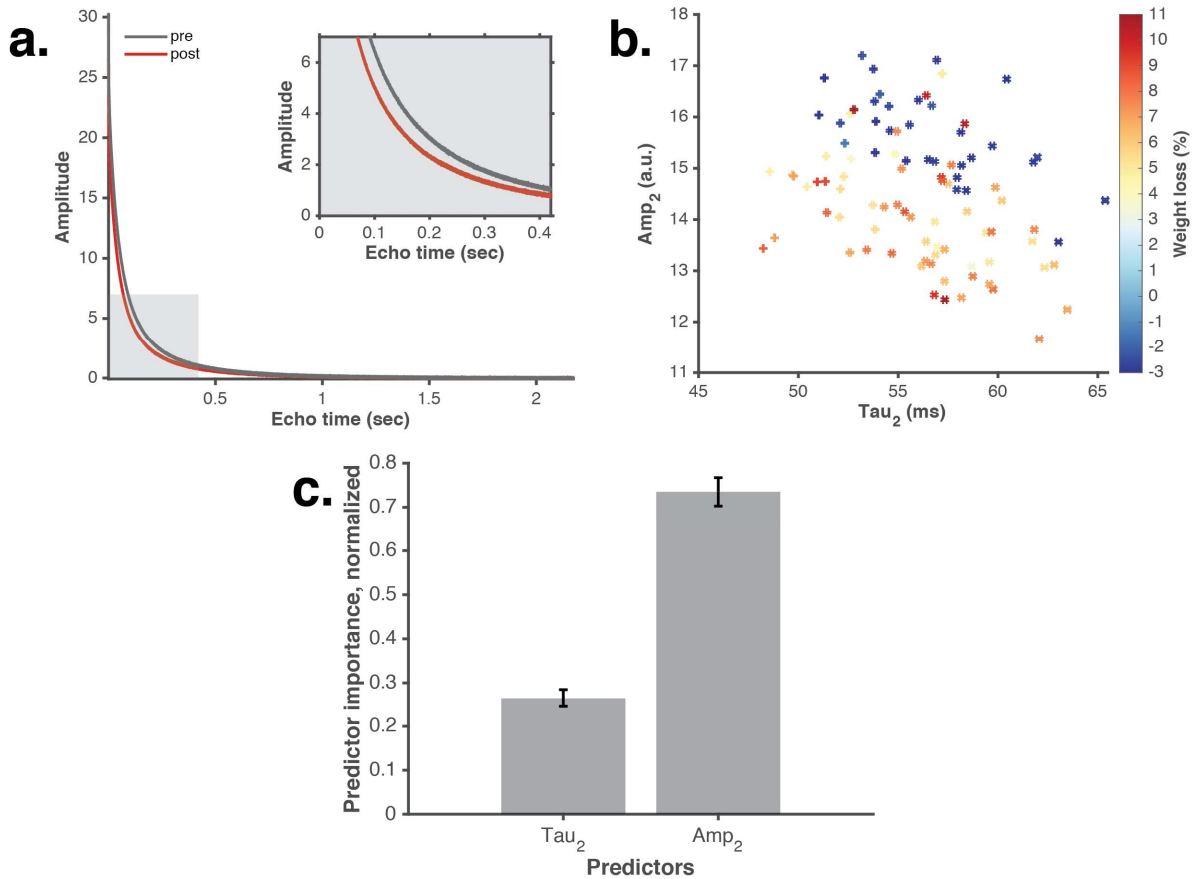


Figure 4.2. Multiexponential fit on whole animal MR measurements. **a)** T2 decay curves from whole animal NMR before and after dehydration show a difference in decay rate. Inset highlights this difference as greatest between 50 and 250 ms. **b)** Dehydration induces a shift in the relaxation time and amplitude corresponding to the second peak in a three component exponential fit. **c)** Identification of strongest predictor of weight loss from whole animal MR measurements

The change in fluid volume was estimated by first learning the T2 relaxation time constants corresponding to each tissue fluid compartment by fitting a multicomponent exponential model to every animal. A triexponential fit with fixed relaxation times as in **Eq. (6)** with $\tau_1 = 10$ ms, $\tau_2 = 52$ ms, $\tau_3 = 264$ ms) was performed to extract the relative amplitudes of fast (A_1), medium (A_2), and slow (A_3)

components. These relaxation times correspond to the mean relaxation times when performing a triexponential fit as in **Eq. (5)** jointly across all scans.

Each distinct exponential signal was averaged across animals, and each time constant was assigned to a particular fluid compartment. The relative contribution of each fluid compartment to each decay curve was then estimated by fitting a linear combination of each of the monoexponential signals (each fluid compartment) to the composite signal.

The estimated fluid volume attributed to the lean muscle tissue decreases significantly after dehydration ($n = 47$, $p < 1 \times 10^{-15}$, statistics by t test) while not changing significantly among control animals ($n = 11$, $p < 0.1241$, statistics by t test) (**Figure 4.3a**). A binary classifier of measurements performed before (pre) and after (post) dehydration via logistic regression demonstrates strong performance. The area under the receiver operating characteristic (ROC) curve (AUROC) is 0.93 [95% C.I., 0.88 to 0.96]. (**Figure 4.3b**). The amplitude of the second component is approximately normally distributed for both measurements performed before (pre) (DHY: $n = 47$, $p = 0.5512$; CTL: $n = 11$, $p = 0.4423$) (**Figure 4.3c**) and after (post) (DHY: $n = 47$, $p = 0.3528$; CTL: $n = 11$, $p = 0.7466$) (**Figure 4.3d**) dehydration for both control and dehydrated mice.

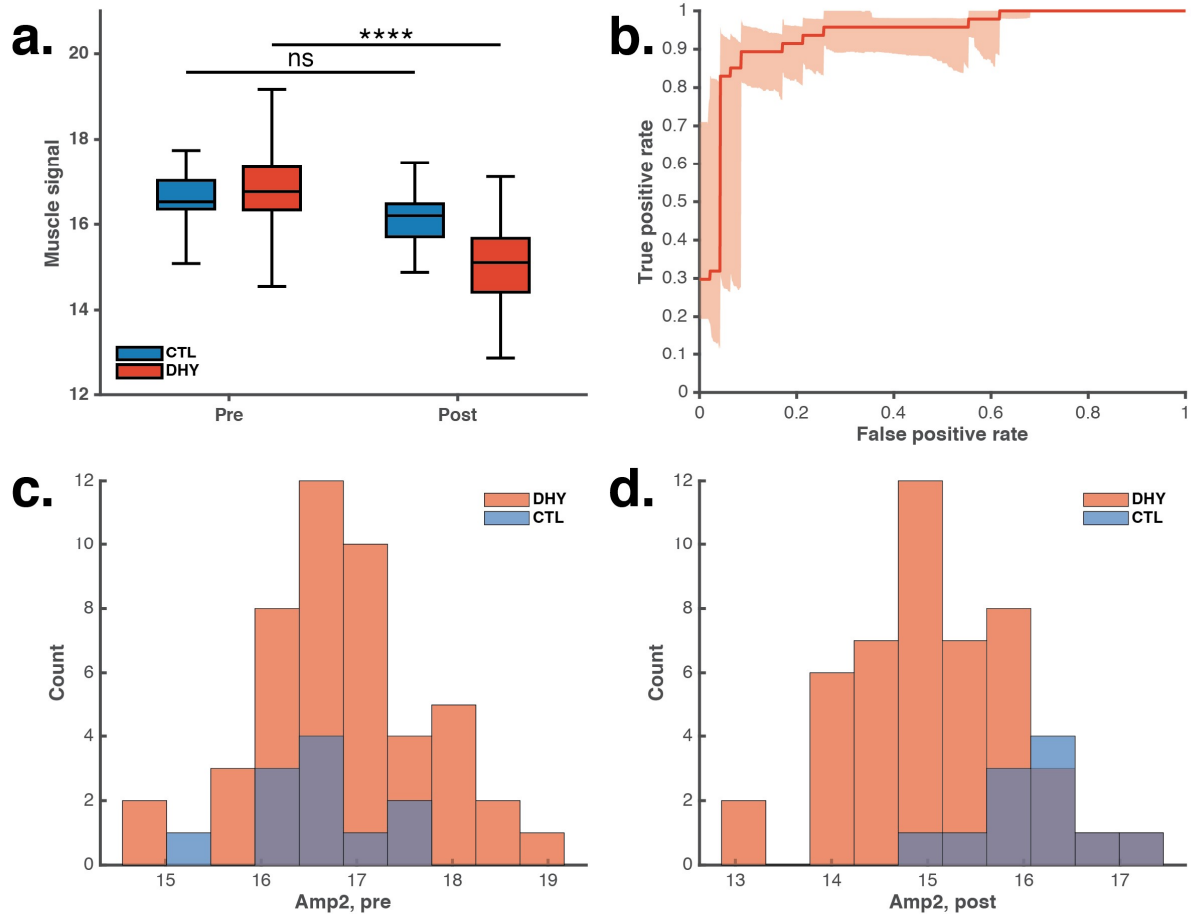


Figure 4.3. MR derived muscle signal predicts dehydration. **a)** The amplitude of the second peak in a triexponential fit with fixed time constants, corresponding to the muscle signal, significantly decreases after dehydration ($n = 47$, $p < 1 \times 10^{-15}$, statistics by t test). Control animals did not exhibit a significant change ($n = 11$, $p < 0.1241$, statistics by t test). **b)** A receiver operator characteristic (ROC) curve of a classifier of pre versus post measurements among dehydrated animals via logistic regression demonstrates an AUROC of 0.93 [95% C.I., 0.88 to 0.96]. Shaded region indicates 95% confidence intervals. The amplitude of the second component is approximately normally distributed for **c)** before dehydration (pre) (DHY: $n = 47$, $p = 0.5512$; CTL: $n = 11$, $p = 0.4423$) and **d)** after dehydration (post) (DHY: $n = 47$, $p = 0.3528$; CTL: $n = 11$, $p = 0.7466$) measurements.

We expected significant variability in the initial hydration state of each animal. We isolated the effect of fluid depletion on the intramuscular fluid component signal by analyzing its change from before to after dehydration. The change in this signal is significantly greater among dehydration versus control animals ($n = 58$, $p < 1 \times 10^{-8}$, statistics by t test) (**Figure 4.4a**). The change in this amplitude from before to after dehydration is approximately normally distributed (DHY: $n = 47$, $p = 0.6320$; CTL: $n = 11$, $p = 0.7042$, statistics by Lilliefors test for normality) (**Figure 4.4b**). The

estimated change in fluid volume attributed to the lean muscle tissue compartment does not show a significant correlation with weight loss in control mice despite fluctuations in weight ($n = 11$, $R^2 = 0.000$, $p = 0.996$, statistics by t test) (**Figure 4.4c**). This signal strongly correlates with weight loss in mice that underwent thermal dehydration ($n = 47$, $R^2 = 0.616$, $p < 1 \times 10^{-10}$, statistics by t test) (**Figure 4.4d**). Residuals of the linear fits do not show any trends with weight loss and are normally distributed (CTL: $n = 11$, $p = 0.6742$; DHY: $n = 47$, $p = 0.3625$, Lilliefors test for normality) (**Figure 4.4e-g**). These results show that the MR signal originating from the lean muscle tissue alone is sufficient to identify and estimate the degree of dehydration.

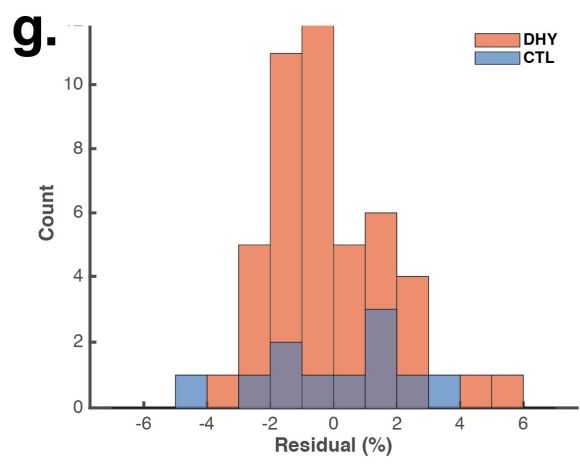
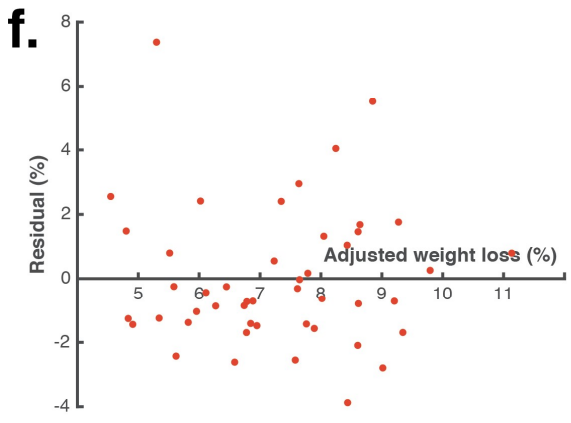
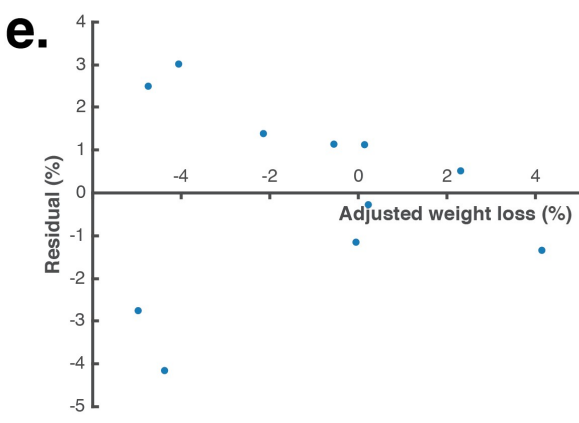
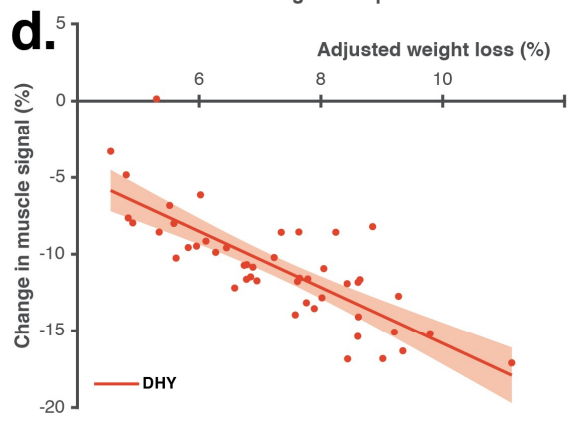
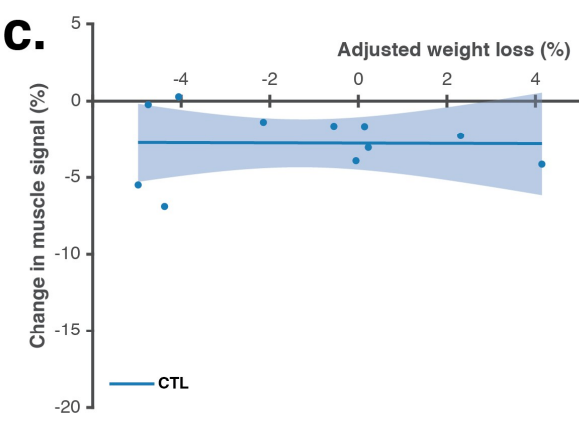
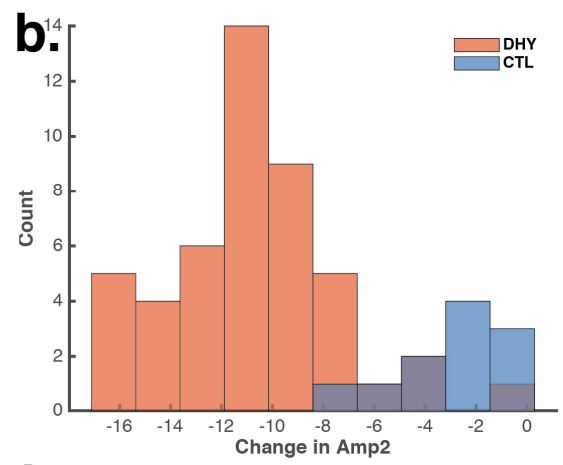
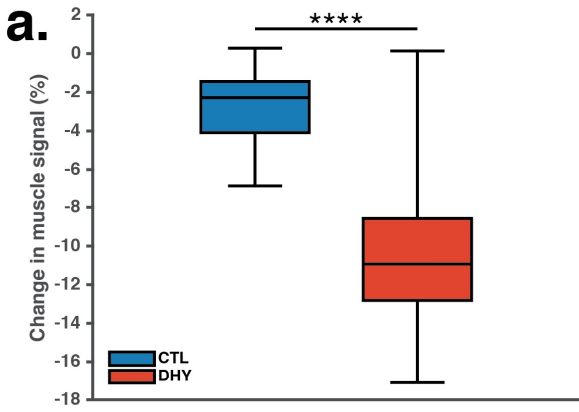


Figure 4.4. Whole animal NMR T2 relaxometry quantifies fluid loss. **a)** The change in MR amplitude corresponding to the muscle signal is significantly greater among dehydration versus control animals. ($n = 58$, $p < 1 \times 10^{-8}$, statistics by t test). **b)** The change in this amplitude from before to after dehydration is also approximately normally distributed (DHY: $n = 47$, $p = 0.6320$; CTL: $n = 11$, $p = 0.7042$). All statistics are by Lilliefors test for normality. **c)** There is no significant correlation between the change in muscle signal amplitude and weight loss in control animals ($n = 11$, $R^2 = 0.000$, $p = 0.996$, statistics by t test). **d)** The change in muscle signal amplitude demonstrates sensitivity towards weight loss induced by dehydration ($n = 47$, $R^2 = 0.616$, $p < 1 \times 10^{-10}$, statistics by t test). Shaded regions indicate 95% confidence intervals for linear fit. **e-f)** Residuals of the linear fits on control and dehydration mice do not show any trends with weight loss. **g)** Residuals are normally distributed (CTL: $n = 11$, $p = 0.6742$; DHY: $n = 47$, $p = 0.3625$, Lilliefors test for normality).

The ultimate goal was to develop a portable sensor to measure dehydration rather than requiring a whole body measurement. The ability to perform a localized measurement towards a specific tissue compartment was essential to allow for miniaturization of the MR sensor. Therefore, we explored the potential to localize a similar MR measurement solely towards the muscle tissue via MRI.

4.4 Muscle localization via MRI

Quantitative T2 relaxometry measurements localized to the skeletal muscle were performed before and after dehydration with a standard MRI scanner. MRI scans were performed with a 7T/310/ASR (Agilent, formerly Varian) scanner with vnmrj software (version 3.2b), equipped with a 38 mm whole body coil. Mice were first anesthetized with 2% isoflurane, then oriented in a supine position, and maintained on 1-2% isoflurane throughout data collection. Warm air (37 C) was delivered to maintain body temperature of animals. T2 weighted anatomical scans were performed with FSEMS (fast spin echo multi slice) with repetition time (TR) 2000 ms, echo time (TE) 12 ms, echo train length (ETL) 4, kzero 2, effective TE 24 ms, 2 averages, 2 dummy scans, 128 x 128 x 5 acquisition matrix, and 40 x 40 x 5 mm field of view. A series of spin echo images for T2 relaxometry were acquired with MEMS (multi echo multi slice) with TR 7600 ms, TE 10 ms, 2 averages, 64 x 32 x 5 acquisition matrix, and 40 x 40 x 5 mm field of view. Slice acquisition order was interleaved using standard two-pass interleaving for both scans. All images were acquired along the coronal plane of the animal.

T2-weighted MRI scans of the upper leg of each mouse were used to draw regions of interest on muscle (ROIs) tissue (**Figure 4.5a**). The upper leg was selected as it is the largest site of skeletal muscle in the extremities. A ROI was drawn on each image to isolate voxels comprised principally of muscle tissue (**Figure 4.5b**).

Regions of interest (ROI) were drawn manually on T2 weighted (T2w) images in Adobe Photoshop (Adobe, USA) to include skeletal muscle within the upper leg while excluding voxels primarily containing fat (high intensity on T2 weighted image). The operator was blinded to the identity and experimental group of each mouse while drawing each ROI to reduce bias.

Voxels containing echoes of very low signal to noise ratio (<30) were excluded to improve the signal to noise ratio of the mean signal. Voxels comprised of a slowly decaying (>100 ms) echo train were excluded as these indicated contamination of the signal from voxels containing a substantial proportion of fat ^{111,112}. The series of spin echoes corresponding to the voxels included within the ROI were averaged to form a single T2 weighted decay for each image.

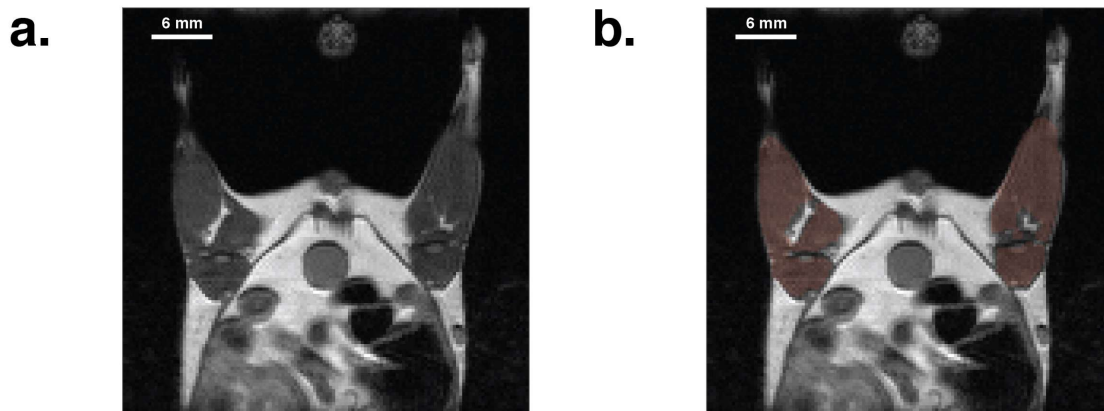


Figure 4.5. ROIs on T2 weighted images of mouse leg muscle. **a)** T2-weighted MRI of the upper leg muscle in a mouse oriented along the coronal plane. **b)** A representative region of interest drawn to include the muscle on a T2-weighted MRI.

The series of spin echo images provide a T2 decay curve capable of quantitatively identifying variation in relaxation rate (**Figure 4.6**).

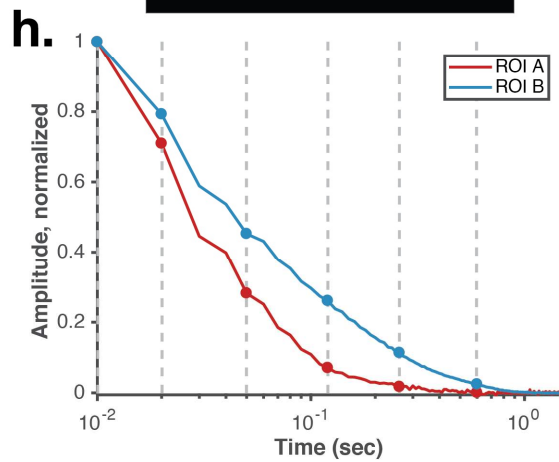
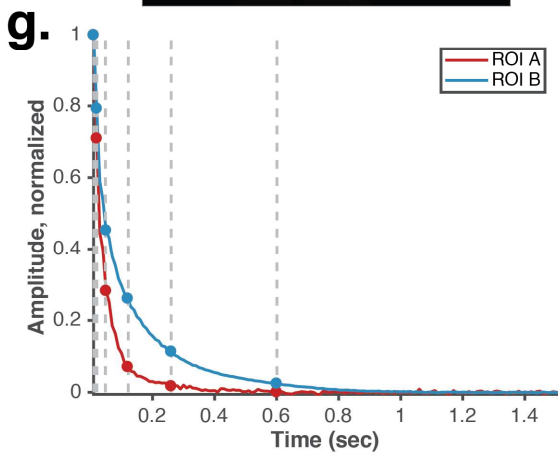
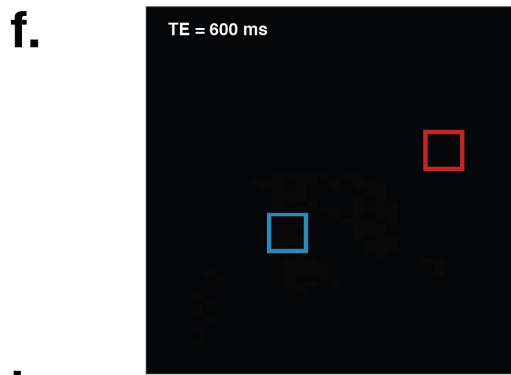
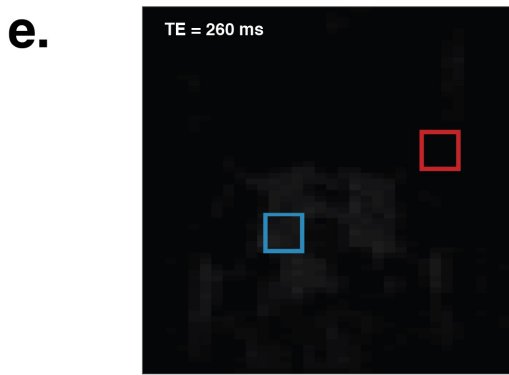
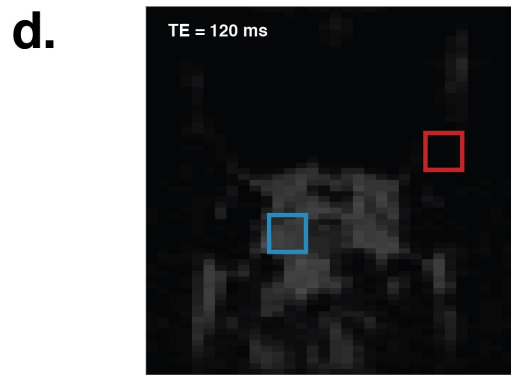
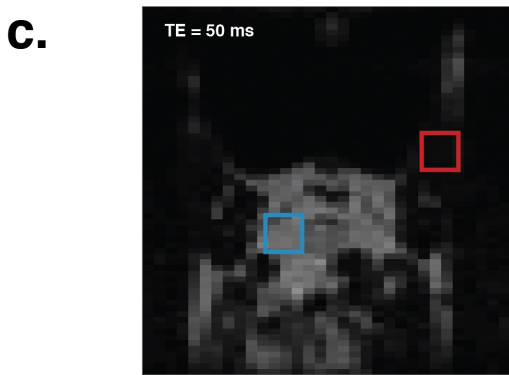
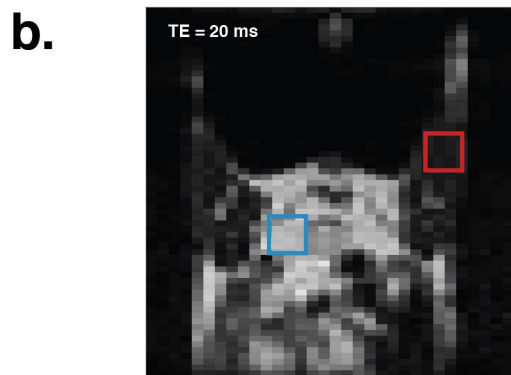
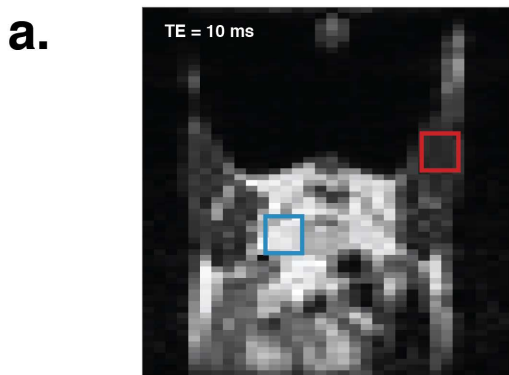


Figure 4.6 Illustration of T2 relaxometry via a series of spin echo MRI images. **a-f**) Spin echo images acquired at increasing echo times (TE) show increased signal attenuation due to T2 relaxation. Voxels corresponding to tissues with a longer T2 (e.g. fat) lose brightness at a slower rate than those corresponding to a shorter TE (e.g. muscle). **g-h**) Acquiring images at many TEs provides a sufficient number of echoes to visualize distinct decay curves and extract relaxation parameters for each tissue. Decay curves corresponding to the sum of all echoes within each ROI across all TEs are shown on **g**) linear and **h**) log plots. Dashed lines indicate the TEs to which the images (**a-f**) correspond.

A composite T2 decay signal was formed from voxels corresponding to muscle tissue (**Figure 4.7**). These signals indicate a decrease in decay time (pre: 58 ms; post: 47 ms) after dehydration.

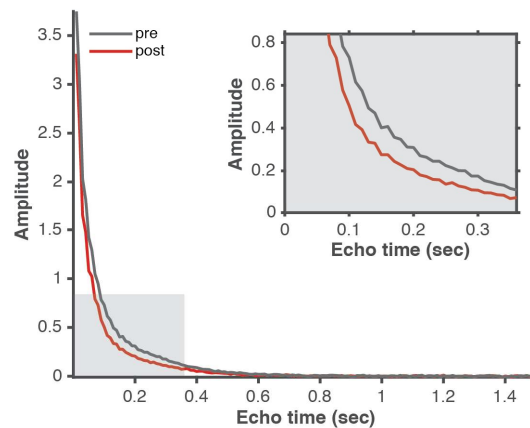


Figure 4.7. T2 relaxometry decay curves from MRI. Decay curves from T2 relaxometry acquired via MRI before and after dehydration show a difference in decay rate. Inset highlights this difference as greatest between 80 and 300 ms.

The noise distribution in each decay curve was transformed from Rician to Gaussian to reduce bias in estimation of the relaxation times (**Figure 4.8**)¹¹³. The MRI data are acquired as magnitude images; therefore, the noise distribution is best approximated as a Rician distribution. This biases parameter extraction algorithms, such as those fitting a multicomponent decaying exponential, as they typically assume a Gaussian noise distribution¹¹⁴. Therefore, we transform the noise distribution of each multi-echo signal from Rician to Gaussian by iteratively estimating the variance of the noise, extracting an estimate of the contribution from noise to each echo, then mapping between the cumulative distribution functions of a Rician distribution to a Gaussian distribution^{113,115}. The noise variance is estimated

iteratively until the absolute value of the median of the echo magnitude in the noise tail is minimized as this was shown to reduce the estimation error in simulated signals.

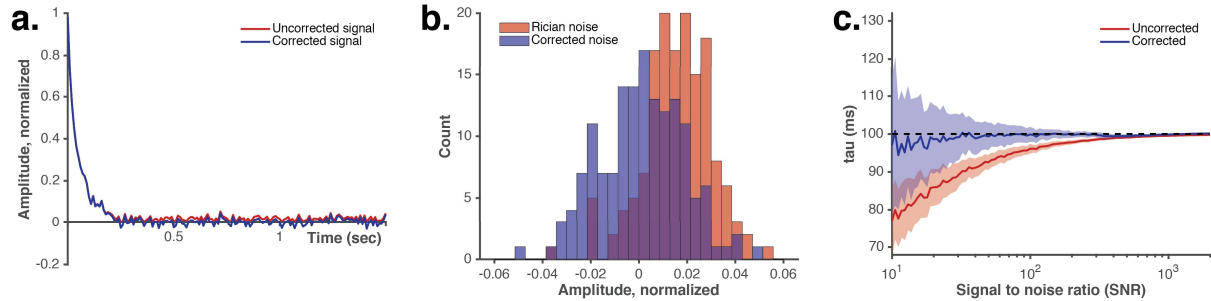


Figure 4.8. Correction of Rician noise from MRI echoes improves accuracy of parameter estimates from exponential fits. **a)** Representative uncorrected and corrected T2 decays from a series of spin echo images with an MRI. **b)** Histograms of the noise amplitude in uncorrected and corrected decays shows a positive bias before correction. **c)** A monoexponential fit performed on uncorrected and corrected synthetic decay curves shows a significant improvement in relaxation time estimation accuracy for corrected data. The shaded regions correspond to 95% confidence intervals upon repeated trials ($n = 100$ trials per SNR level).

A biexponential fit with fixed relaxation times (as in **Eq. (6)** with $\tau_1 = 21$ ms and $\tau_2 = 75$ ms) was performed to extract the relative amplitudes of fast (A_1) and slow (A_2) components. These relaxation times correspond to the mean relaxation times when performing a biexponential fit as in **Eq. (5)** jointly across all images. The long component of the biexponential T2 signal corresponds to the intramuscular ECF compartment ^{68,72–74}. The estimated fluid volume attributed to the intramuscular ECF decreases significantly after dehydration ($n = 33$, $p < 1 \times 10^{-6}$, statistics by t test) while not changing significantly among control animals ($n = 9$, $p < 0.5820$, statistics by t test) (**Figure 4.9a**). A binary classifier of measurements performed before (pre) and after (post) dehydration via logistic regression demonstrates strong performance. The AUROC is 0.85 [95% C.I., 0.77 to 0.90]. (**Figure 4.9b**). The amplitude of the second component is approximately normally distributed for (**Figure 4.9c**) before dehydration (pre) (DHY: $n = 33$, $p = 0.4598$; CTL: $n = 9$, $p = 0.9344$, Lilliefors test for normality) and (**Figure 4.9d**) after dehydration (post) (DHY: $n = 33$, $p = 0.5782$; CTL: $n = 9$, $p = 0.6636$, Lilliefors test for normality) measurements.

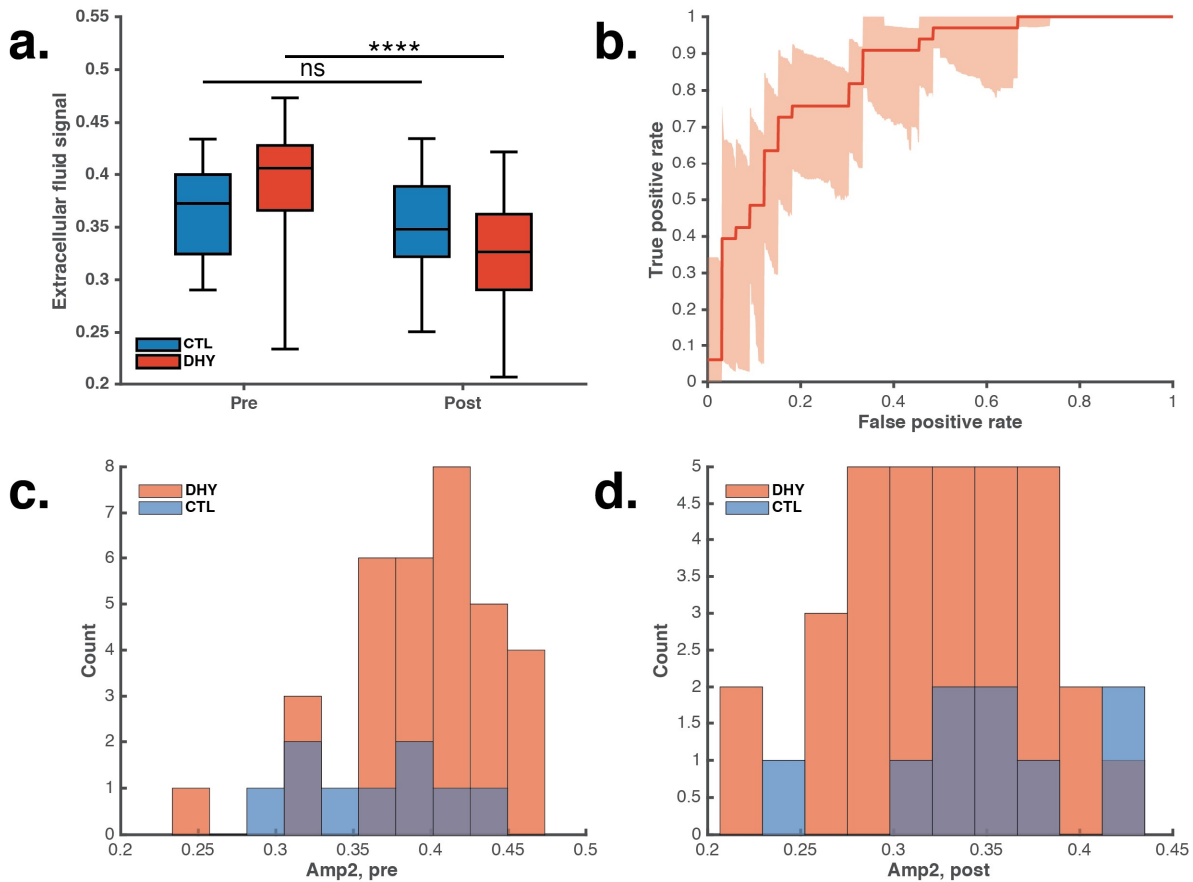


Figure 4.9. T2 relaxometry with MRI localized to the muscle identifies fluid depletion. **a)** The amplitude of the second peak in a biexponential fit with fixed time constants, corresponding to the intramuscular ECF signal, significantly decreases after dehydration ($n = 33$, $p < 1 \times 10^{-6}$, statistics by t test). Control animals did not exhibit a significant change ($n = 9$, $p < 0.5820$, statistics by t test). **b)** A ROC curve of a classifier of pre versus post measurements among dehydrated animals via logistic regression demonstrates an AUROC of 0.85 [95% C.I., 0.77 to 0.90]. Shaded region indicates 95% confidence intervals. The amplitude of the second component is approximately normally distributed for **c)** before dehydration (pre) (DHY: $n = 33$, $p = 0.4598$; CTL: $n = 9$, $p = 0.9344$) and **d)** after dehydration (post) (DHY: $n = 33$, $p = 0.5782$; CTL: $n = 9$, $p = 0.6636$) measurements. All statistics are by Lilliefors test for normality.

We analyze the change in the muscle ECF signal from before to after dehydration to isolate the effect of fluid depletion while compensating for variability in the initial hydration state of each animal. The change in this signal is significantly greater among dehydration versus control animals ($n = 42$, $p < 0.0011$, statistics by t test) (**Figure 4.10a**). The change in this amplitude from before to after dehydration is approximately normally distributed (DHY: $n = 33$, $p = 0.6062$; CTL: $n = 9$, $p = 0.4246$, Lilliefors test for normality) (**Figure 4.10b**). The estimated change in fluid

volume attributed to the intramuscular ECF compartment does not show a significant correlation with weight loss in control mice ($n = 9$, $R^2 = 0.035$, $p = 0.632$, statistics by t test) (**Figure 4.10c**). This signal strongly correlates with weight loss in mice that underwent thermal dehydration ($n = 33$, $R^2 = 0.713$, $p < 1 \times 10^{-9}$, statistics by t test) (**Figure 4.10d**). Residuals of the linear fits do not show any trends with weight loss and are normally distributed (**Figure 4.10e-g**). These results show that the MR signal originating from muscle tissue alone is sufficient to identify and estimate the degree of dehydration. We utilized the change in the MR amplitude corresponding to the muscle ECF in order to quantify fluid loss due to dehydration (**Figure 4.10d**). The use of the change in amplitude accounted for the baseline variability observed in the initial hydration state of each animal.

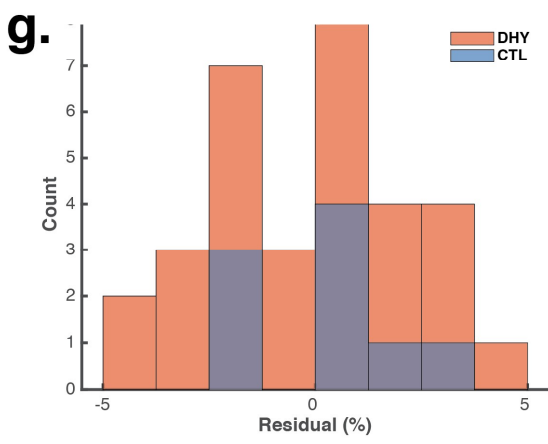
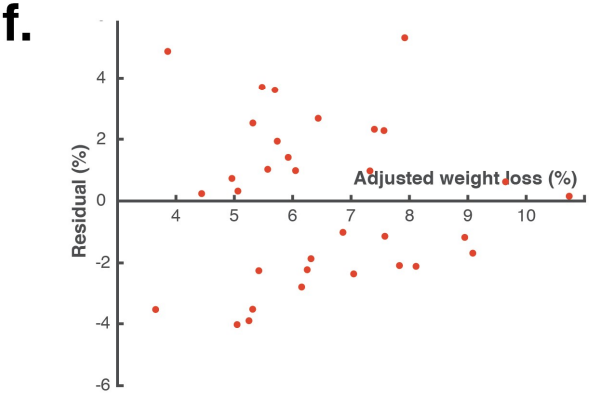
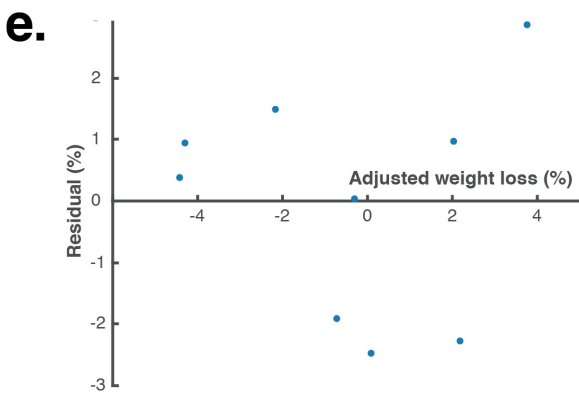
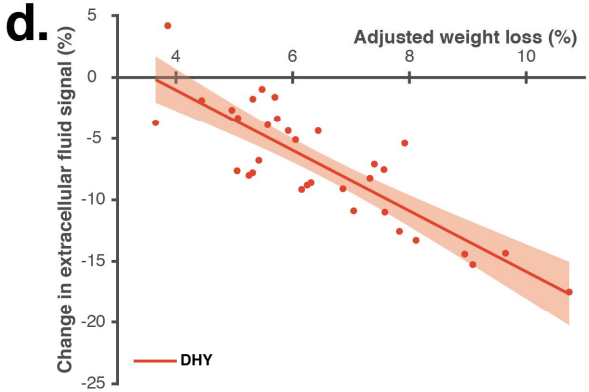
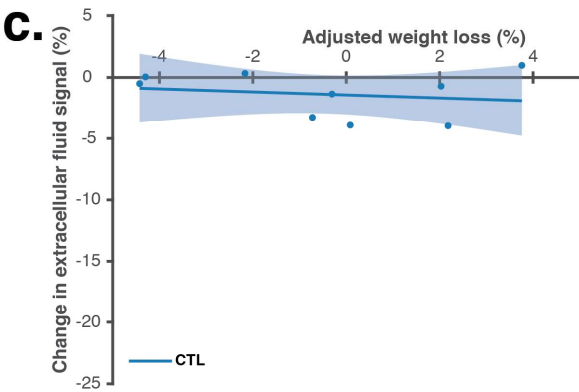
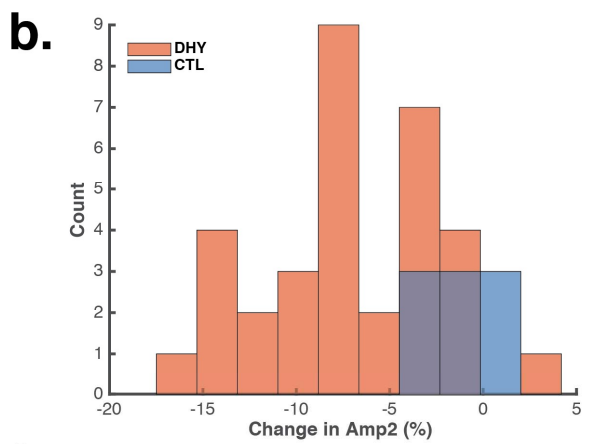
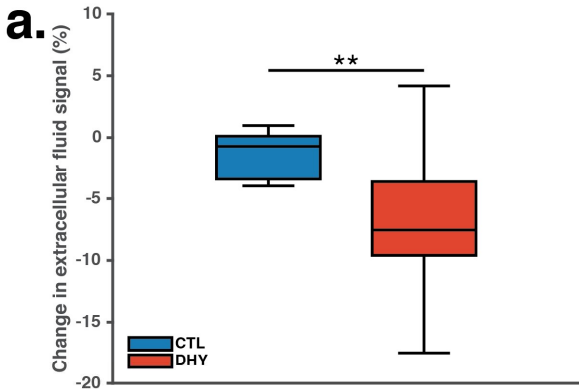


Figure 4.10 T2 relaxometry with MRI localized to the muscle quantifies fluid depletion due to thermal dehydration. **a)** The change in MR amplitude corresponding to the intramuscular ECF signal is significantly greater among dehydration versus control animals. ($n = 42$, $p < 0.0011$, statistics by t test). **b)** The change in the amplitude of the second component from before to after dehydration is approximately normally distributed (DHY: $n = 33$, $p = 0.6062$; CTL: $n = 9$, $p = 0.4246$, Lilliefors test for normality). **c)** There is no significant correlation between the change in the intramuscular ECF signal amplitude and weight loss in control animals ($n = 9$, $R^2 = 0.035$, $p = 0.632$, statistics by t test). **d)** The change in this signal significantly correlates with weight loss induced by dehydration ($n = 33$, $R^2 = 0.713$, $p < 1 \times 10^{-9}$, statistics by t test). Shaded regions indicate 95% confidence intervals for linear fit. Residuals for linear fits for control (CTL) and dehydration (DHY) T2 relaxometry scans with MRI on muscle **e-f)** do not show any trends dependent on weight loss and **g)** are approximately normally distributed (CTL: $n = 9$, $p = 0.5190$; DHY: $n = 33$, $p = 0.4031$, Lilliefors test for normality).

Despite this variability, the initial ECF amplitude was moderately correlated with weight loss and the rate of weight loss (**Figure 4.11**). Features were extracted from the weight loss time series data to explore their correlation with the initial ECF amplitude measured via MRI. The final weight loss (**Figure 4.11a**) was defined as the weight loss each mouse experienced from the start to the end of the experiment. The time to reach 6% weight loss (**Figure 4.11b**) was defined as the period of time until each mouse lost 6% of its initial body weight. Weight loss at 2 hours and 6 hours (**Figure 4.11c-d**) was defined as the weight loss each mouse reached at the specified time from the start of the experiment.

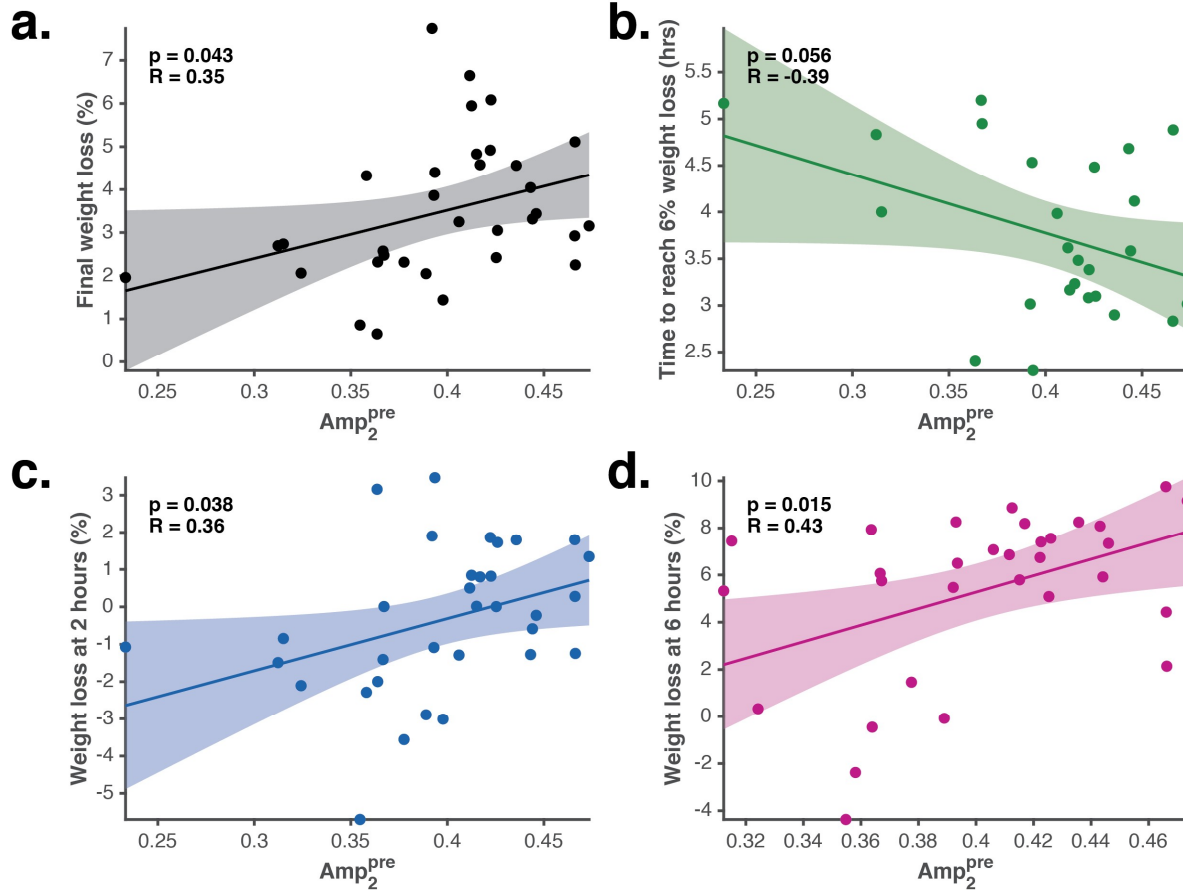


Figure 4.11 Predicting weight loss with initial MRI muscle ECF amplitude. **a-d)** The correlation between the muscle ECF amplitude from MRI before dehydration and each weight loss feature. The initial muscle ECF amplitude is correlated with each of the respective features derived from the weight loss time series data. The positive correlations with weight loss (a,c,d) indicate an increased capacity for fluid loss in animals exhibiting large values for initial muscle ECF amplitude. The negative correlation with time (b) indicates an increased weight loss rate in animals exhibiting large values for initial muscle ECF amplitude.

We demonstrate that a multicomponent T2 measurement localized to the muscle tissue is capable of quantifying whole body dehydration. The utility of MRI as a diagnostic measure of dehydration is limited by its complexity, long measurement time, manual interpretation, high cost, and lack of portability. Therefore, we aimed to show that a comparable measurement performed by our portable MR sensor could similarly identify fluid loss induced by dehydration while overcoming the limitations of MRI.

4.5 Portable MR measurements

Our portable MR sensor is able to perform a T2 measurement of the skeletal muscle, similarly to the MRI, which enables isolation and analysis of the signal originating from each tissue fluid compartment. The Unilateral Linear Halbach magnet geometry allows the sensor to perform a highly localized measurement on a remote region located within the skeletal muscle of the mouse leg. T2 relaxometry was performed using our portable MR sensor on the upper leg of a mouse (**Figure 4.12a**). The signal originated primarily from the muscle tissue with some contribution from subcutaneous tissue and bone (**Figure 4.12b**).

Anesthetized (2% isoflurane) mice were placed on top of the portable MR sensor in a prone position. The upper leg was positioned directly on top of the RF coil and secured with tape to minimize motion during signal acquisition. The RF impedance matching circuit was tuned and matched to achieve a reflection coefficient of less than 1% at the RF excitation frequency (B_1 frequency). A series of CPMG scans were acquired to perform T2 relaxometry (11.61 MHz B_1 frequency, 65 μ s echo time, number of echoes 8192, 1 dummy echo, 1 MHz acquisition bandwidth, 12 μ s pulse duration, 1.517 sec repetition time) until the signal to noise ratio of the resultant mean signal exceeded 150. The majority of the signal from this measurement originates in the vastus medialis, vastus lateralis, and rectus femoris muscles.

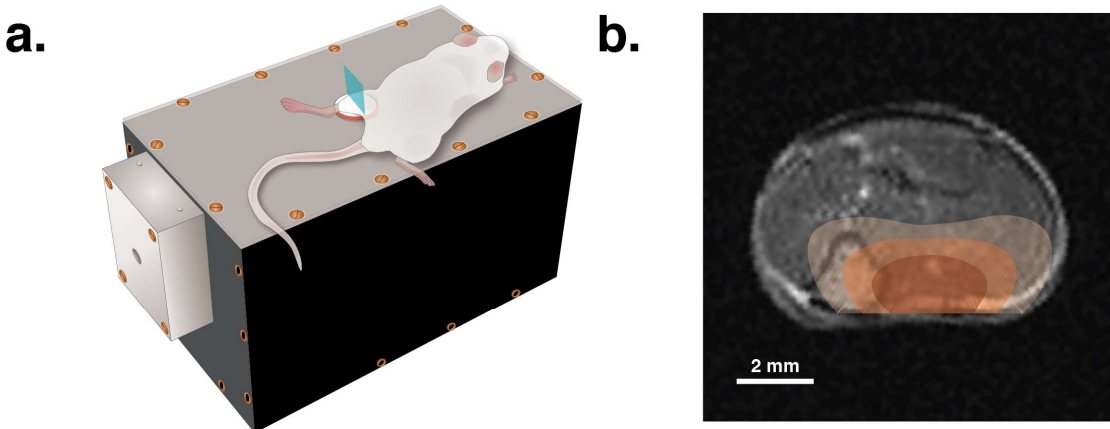


Figure 4.12 Portable MR sensor localized to the skeletal muscle. **a)** Illustration of portable MR sensor with upper leg of mouse positioned over sensitive region. Blue plane indicates approximate

orientation of MRI image shown in (b). **b)** T2-weighted axial MRI of a mouse leg with overlaid sensitivity profile from portable MR sensor. Yellow, orange, and red contours indicate 25%, 50%, and 75% of max sensitivity, respectively.

The time-domain relaxometry signal shows a decrease in decay time (pre: 67.1 ms; post: 45.4 ms) after dehydration, similarly to that seen in T2 relaxometry performed with an MRI (**Figure 4.13a**). The component corresponding to the ECF was most responsive to fluid depletion (**Figure 4.13b**). The muscle ECF compartment amplitude was three times as important as the respective relaxation time in predicting weight loss when assessed via binary decision regression tree analysis (**Figure 4.13c**). The amplitude of the second component of portable MR sensor measurements, corresponding to ECF, was an approximately 3.2 times more important predictor of weight loss than the respective relaxation time. Predictor importance was calculated by estimating the change in mean squared error attributed to the inclusion of each predictor in the binary decision regression tree. Error bars indicate standard error of the mean across all models generated via 10-fold cross validation.

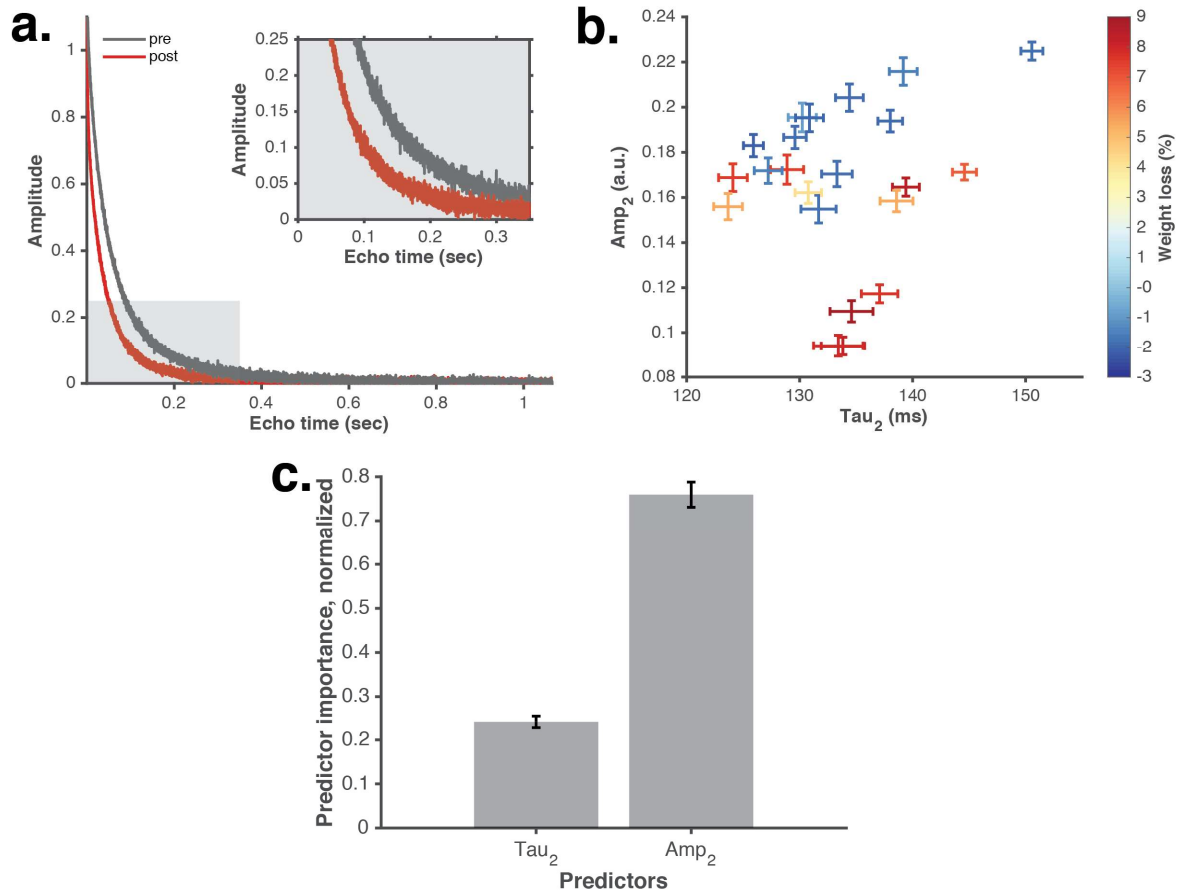


Figure 4.13 Multicomponent T2 relaxometry on skeletal muscle via portable MR sensor. **a)** T2 relaxometry decay curves localized towards muscle with portable MR sensor before and after dehydration show a difference in decay rate. Inset highlights greatest difference between 40 and 200 ms. **b)** Dehydration induces a shift in the amplitude of the third peak in a triexponential fit (**Eq. (5)**). Colors indicate weight loss induced by dehydration. **c)** Identification of strongest predictor of weight loss from portable MR sensor measurements.

A triexponential fit with fixed relaxation times (**Eq. (6)** with $\tau_0 = 1$ ms, $\tau_1 = 50$ ms, $\tau_2 = 150$ ms) was performed to extract the relative amplitudes of fast (A_0), medium (A_1), and slow (A_2) components. These relaxation times correspond to the mean relaxation times when performing a triexponential fit as in **Eq. (5)** jointly across all scans.

The estimated fluid volume attributed to the intramuscular ECF decreases significantly after dehydration ($n = 11$, $p < 0.0104$, statistics by Mann–Whitney U test) while not changing significantly among control animals ($n = 14$, $p < 0.8630$, statistics by t test) (**Figure 4.14a**). A binary classifier of measurements performed

before (pre) and after (post) dehydration via logistic regression demonstrates strong performance. The AUROC is 0.83 [95% C.I., 0.65 to 0.93] (**Figure 4.14b**). The amplitude of the second component is approximately normally distributed for (**Figure 4.14c**) before dehydration (pre) (DHY: $n = 11$, $p = 0.4558$; CTL: $n = 14$, $p = 0.8013$, Lilliefors test for normality) and (**Figure 4.14d**) after dehydration (post) for only control measurements (DHY: $n = 11$, $p = 0.0308$; CTL: $n = 14$, $p = 0.7398$, Lilliefors test for normality) measurements.

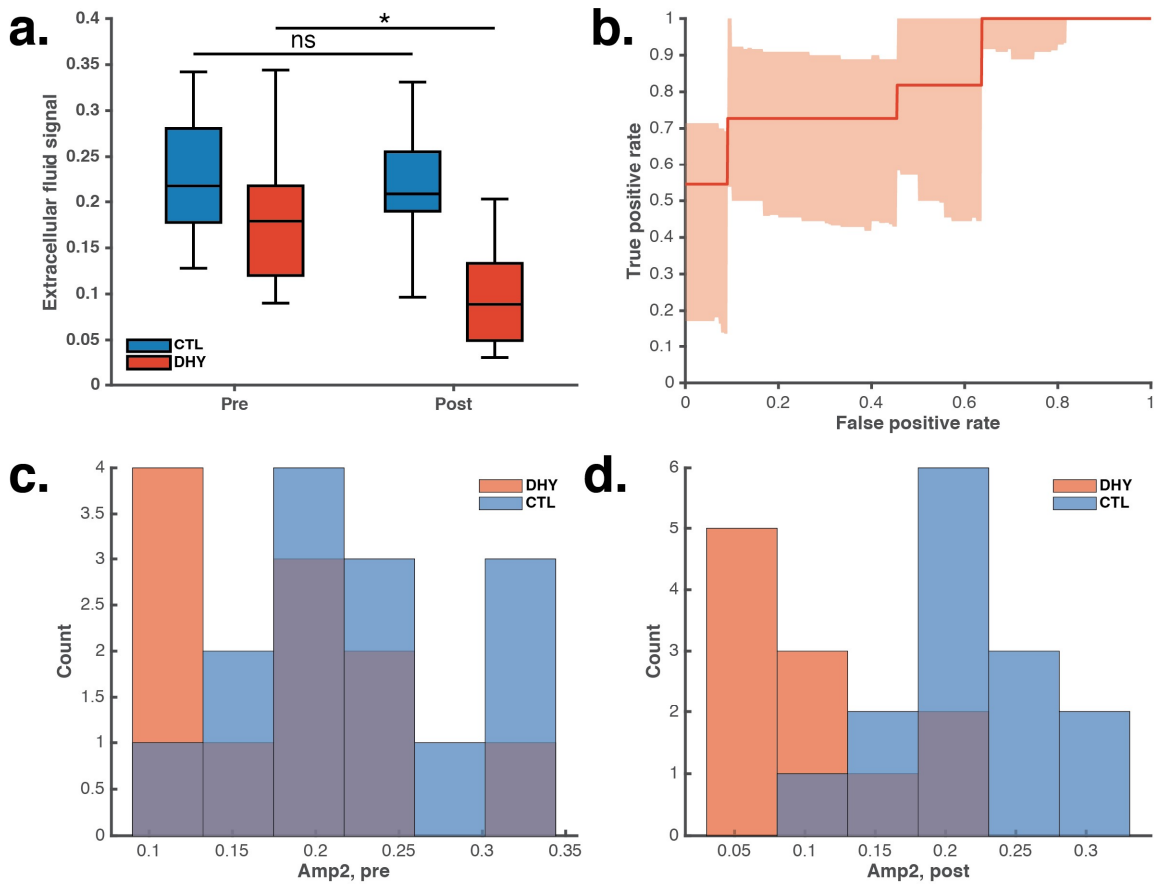


Figure 4.14 T2 relaxometry with portable MR sensor identifies fluid depletion due to thermal dehydration. **a**) The amplitude of the second peak, corresponding to the intramuscular ECF signal, significantly decreases after dehydration ($n = 11$, $p < 0.0104$, statistics by Mann–Whitney U test). Control animals did not exhibit a significant change ($n = 14$, $p < 0.8630$, statistics by t test). **b**) A ROC curve of a classifier of pre versus post measurements among dehydrated animals via logistic regression demonstrates an AUROC of 0.83 [95% C.I., 0.65 to 0.93]. Shaded region indicates 95% confidence intervals. The amplitude of the second component is approximately normally distributed for **c**) before dehydration (pre) (DHY: $n = 11$, $p = 0.4558$; CTL: $n = 14$, $p = 0.8013$, Lilliefors test for normality) and **d**) after dehydration (post) for only control measurements (DHY: $n = 11$, $p = 0.0308$; CTL: $n = 14$, $p = 0.7398$, Lilliefors test for normality) measurements.

We, once again, analyzed the change in the intramuscular ECF signal from before to after dehydration to isolate the effect of fluid depletion while compensating for variability in the initial hydration state of each animal. The change in this signal is significantly greater among dehydration versus control animals ($n = 25$, $p < 0.0047$, statistics by t test) (**Figure 4.15a**). The change in this amplitude from before to after dehydration is also approximately normally distributed (DHY: $n = 11$, $p = 0.5397$; CTL: $n = 14$, $p = 0.8306$, Lilliefors test for normality) (**Figure 4.15b**). The estimated change in fluid volume attributed to this compartment does not show a significant correlation with weight loss in control mice ($n = 14$, $R^2 = 0.044$, $p = 0.471$, statistics by t test) (**Figure 4.15c**). This signal strongly correlates with weight loss ($n = 11$, $R^2 = 0.732$, $p < 0.001$, statistics by t test) in mice that underwent thermal dehydration (**Figure 4.15d**). Residuals of a linear fit do not show any trends with weight loss (**Figure 4.15e-f**). Residuals are approximately normally distributed (CTL: $n = 14$, $p = 0.7755$; DHY: $n = 11$, $p = 0.3801$, Lilliefors test for normality) (**Figure 4.15g**). This shows that a localized measurement within the muscle tissue performed by a single sided portable MR sensor can identify and predict fluid loss induced by thermal dehydration.

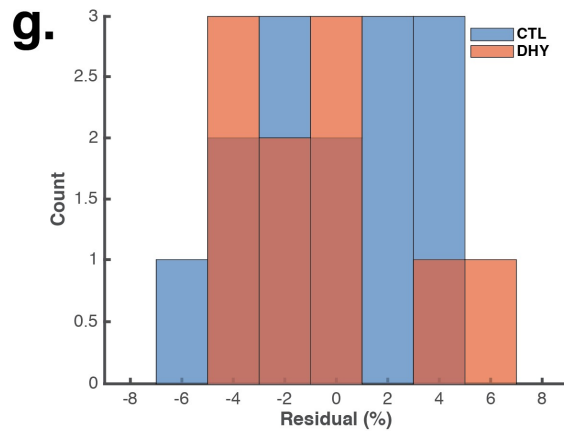
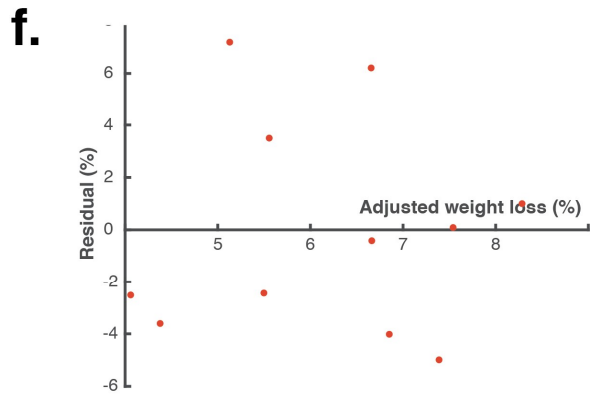
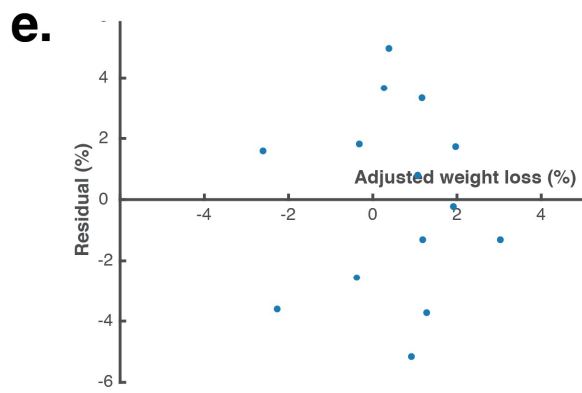
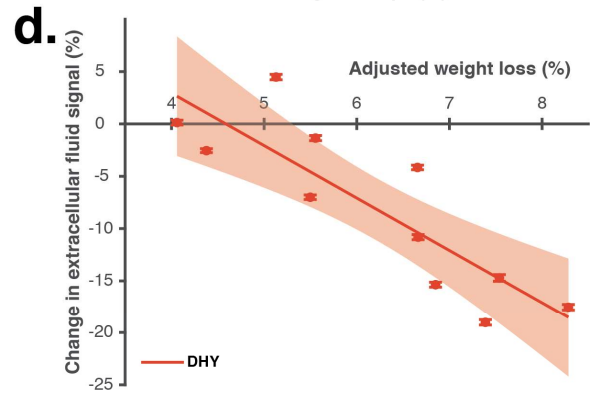
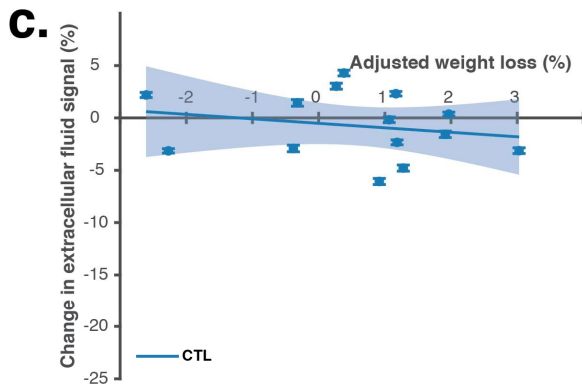
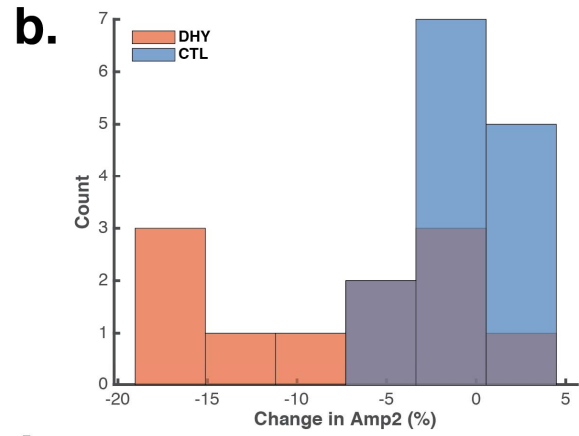
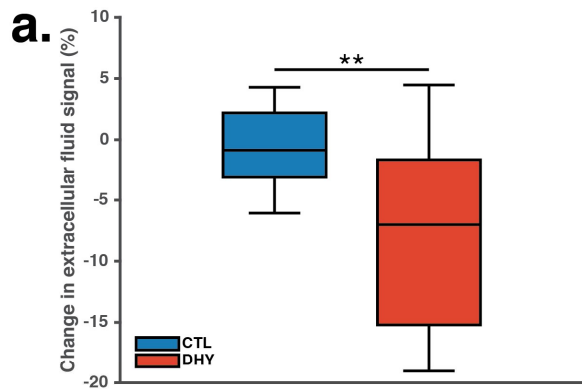


Figure 4.15 T2 relaxometry with portable MR sensor quantifies fluid depletion due to thermal dehydration. **a)** The change in MR amplitude corresponding to the intramuscular ECF signal is significantly greater among dehydration versus control animals. ($n = 25$, $p < 0.0047$, statistics by t test). **b)** The change in this amplitude from before to after dehydration is also approximately normally distributed (DHY: $n = 11$, $p = 0.5397$; CTL: $n = 14$, $p = 0.8306$, Lilliefors test for normality). **c)** There is no significant correlation between the change in the intramuscular ECF signal amplitude and weight loss in control animals ($n = 14$, $R^2 = 0.044$, $p = 0.471$, statistics by t test). **d)** The change in this signal significantly correlates with weight loss induced by dehydration ($n = 11$, $R^2 = 0.732$, $p < 0.001$, statistics by t test). Shaded regions indicate 95% confidence intervals for linear fit.

4.6 Discussion

A non-invasive, portable, reliable measurement of fluid volume status would have broad implications for human health ¹¹⁶. Unmanaged disruption of euvoemia is associated with negative health outcomes. The ability to accurately estimate fluid volume status would allow for improved fluid management across diverse patient populations. These include those experiencing dehydration due to limited fluid intake, environmental exposure, or physical activity; critically ill patients in the intensive care unit; elderly and neonatal patients; and those presenting to the emergency department ^{1,2,15,16,7-14}. For example, a real-time measure of fluid volume status could inform fluid management in ICU patients, especially those contraindicated for invasive measures such as right heart catheterization. Magnetic resonance based measurements of local disruptions of tissue fluid distribution have proven clinical utility ^{68,117,118}. Our work extends this to measure systemic fluid depletion from a localized measurement of tissue fluid distribution.

We demonstrate the ability to estimate fluid volume depletion through three independent magnetic resonance relaxometry-based measurement techniques: whole animal NMR, MRI, and portable MR. We show that a localized MR measurement performed both via MRI and a portable MR sensor can identify systemic fluid volume status. Our results provide preclinical support of the results from our prior human study ⁶³. This suggests the potential to use this technology for diagnosing dehydration.

We hypothesized that an MR measurement of intramuscular ECF depletion could identify dehydration. The accepted physiological model of fluid shifts due to thermal dehydration supports this. Thermal dehydration causes ECF space contraction in humans and rodents ^{58,119–121}. The change in the relative volume of the extracellular versus total fluid within muscle tissue forms the basis for the MR signal measured with both MRI and the portable MR sensor. The shift in fluids from the extracellular space into the vascular space is driven by osmotic forces and, therefore, the concentration of solutes within the ISF remains approximately unchanged ^{119,121}. We observed a larger change in the MR amplitude of the intramuscular ECF compared to that of the relaxation rate. This supports the hypothesis that this measurement is sensitive towards changes in the relative volume of these tissue fluid compartments as solute concentration more strongly affects relaxation rate.

The combination of fluid restriction and exposure to a high temperature environment provided rapid fluid loss to directly test our hypothesis while reducing the influence of confounding factors present in other methods of inducing dehydration such as physical activity ^{122,123}. Control animals experienced mean weight loss of 3% body weight during experiments despite no exposure to elevated temperature and access to food and water. This deviation in weight was likely due to voiding of urine and feces, inter-animal variability of food and fluid intake, and changes in metabolism due to disruption of regular diurnal cycle and stress due to handling ^{107–109}. These animals maintained euvolemia throughout the experiment as we provided unrestricted access to food and water. No change in MR signal was observed before and after the experiment across all MR measurement techniques (i.e. NMR, MRI, and portable MR). These results support the hypothesis that the intramuscular ECF compartment signal exhibits a decrease when homeostasis is disturbed and the animal must rely upon this fluid compartment to maintain plasma volume.

Existing clinical diagnostics of dehydration typically rely on blood chemistry, urinalysis, and blood pressure. These values deviate from normal due to contraction of the intramuscular ECF space. Direct measurements of systemic fluid loss, such as body weight change, are insufficient as there is significant variability in the size of the fluid reservoir used to maintain euvolemia. Dehydration can occur in patients who have lost widely varying amounts of fluid due to body composition variability. A more direct measurement of changes in intramuscular fluid distribution would provide a highly specific measure of dehydration. We observed strong correlations between the intramuscular ECF MR signals and weight loss in this study due to the high degree of similarity in body mass and muscle mass among experimental animals. These findings agree with the physiological model that the intramuscular ECF depletes in proportion to fluid loss after a particular threshold of weight loss (2-4%). A diagnostic of dehydration capable of guiding treatment may only need to identify intramuscular ECF depletion rather than quantify fluid loss. A further clinical study in humans that builds on this work is needed to demonstrate that intramuscular ECF depletion correlates with clinical signs and outcomes associated with dehydration.

Our prior study in HD patients presented results that show that excess fluid in these hypervolemic patients can be observed by T2 relaxometry localized to the skeletal muscle⁶³. Interestingly, changes in weight and blood chemistry indicated that two healthy control subjects experienced dehydration during this study. MRI performed on those subjects before and after the experiment showed a decrease in the intramuscular ECF signal corresponding to dehydration. The current study was designed to corroborate these initial results and demonstrate the utility of a portable MR sensor via a preclinical model of hyperosmotic dehydration. Notably, although the values of relaxation times cannot be directly compared due to the physical differences between MR devices (e.g. magnetic field strength and homogeneity) and differences in pulse sequence parameters (e.g. echo time, RF pulse duration, number of echoes, repetition time), we observe similar changes in

the amplitude associated with the ECF within muscle. These similarities underscore the robustness and reproducibility of this measurement technique. These results support the proposed explanation from the prior study and suggest that portable MR measurements of intramuscular fluid can identify both dehydration and volume overload in humans.

Limited control over the position of the mouse leg above the sensitive region in portable MR measurements likely increased variability of estimates of tissue fluid compartment amplitudes. The sensitive region was larger than necessary and of a similar scale to that of the mouse leg. A shift in the position of the mouse leg may, therefore, have changed the relative signal contribution of distinct tissues (e.g. muscle, subcutaneous, adipose, osseous) with different relaxation properties within the leg. This source of variability will be resolved when measuring human subjects as the volume of muscle tissue available for measurement will be much larger compared to the sensor sensitive region. A sensor capable of performing a deeper measurement through improved magnet design would reduce the potential for confounding signals from more proximal tissue layers such as the dermis and subcutaneous tissue. Other strategies to overcome confounding signal from the proximal subcutaneous tissue include first measuring its thickness and then estimating the signal contribution originating from the muscle. Further characterization of the sensor may enable isolation of the muscle tissue through improved pulse sequences. For example, the addition of diffusion-weighted scans may help isolate the muscle tissue for further analysis. These improvements may allow a future sensor to perform an absolute measure of fluid volume status in subjects with variability in subcutaneous thickness. This would obviate the need for a baseline measurement at euhydration allowing for use as both a monitor of changes in hydration state and an absolute diagnostic of dehydration. A clinical study in a human model of dehydration with an improved sensor would allow this technology to demonstrate clinical utility in a relevant patient population.

In summary, we demonstrate that a localized measure of tissue fluid distribution using a portable MR device is capable of identifying systemic changes in fluid volume status associated with fluid depletion. We validate these findings via whole animal MR measurements and a standard MRI scanner capable of localizing its measurement towards the muscle tissue. Our measurement provides a noninvasive indicator of the fluid volume of distinct fluid compartments and their differential volume contractions during fluid depletion. This method of identifying fluid volume status has the potential to serve as a versatile and portable point of care monitoring technique for dehydration.

This page intentionally left blank

Chapter 5

Techniques to enable clinical translation of portable MR sensors

5.1 Introduction

Portable, non-invasive sensors of tissue fluid distribution would aid in diagnosis of fluid volume disorders and inform therapeutic decisions across diverse patient populations. Existing techniques are inaccurate, invasive, or easily confounded by patient physiology. Single-sided MR devices could provide a portable, low-cost platform for localized measurements of fluid distribution. Subcutaneous tissue proximal to the sensor confounds measurements of intramuscular fluid distribution via single sided MR sensors.

We demonstrate a single-sided MR sensor based on the Unilateral Linear Halbach magnet design capable of identifying intramuscular fluid shifts via a localized measurement. This sensor is capable of performing depth-resolved measurements by tuning the RF excitation frequency. We demonstrate quantification of the relative fractions of tissues within heterogeneous samples via multicomponent T2 relaxometry. The sensor exhibits contrast dependent on the diffusivity of the sample. We leverage this capability to isolate and characterize tissues with otherwise similar MR relaxation properties. We then apply these techniques in combination to show that a depth-resolved, diffusion-weighted, multicomponent T2 relaxometry measurement can identify and track the onset and progression of

muscle edema despite the presence of a confounding proximal subcutaneous tissue layer.

We primarily utilize a portable MR sensor realized through the use of a Unilateral Linear Halbach magnet geometry ¹⁰⁴. Briefly, this sensor consists of an array of 180 permanent magnets arranged to produce a static magnetic field (0.28 Tesla) with <2% field variation over a volume spanning approximately 12 x 6 x 6 mm. Bashyam et al. provides detailed descriptions of the design, construction, and characterization of the MR sensor ¹²⁴.

These innovations enable miniaturized, single-sided MR sensors to perform measurements of fluid distribution in the muscle tissue, the tissue that is most responsive to disruptions in fluid volume status. This non-invasive, portable, point of care technique has the potential to help diagnose and manage conditions involving disruptions in fluid distribution such as congestive heart failure, end-stage renal disease, and dehydration. The work in this chapter was performed in collaboration with Chris J. Frangieh.

5.2 Tuning RF excitation frequency enables slice selection

The measurement depth of single-sided MR sensors, including our sensor based on the Unilateral Linear Halbach magnet array, is limited due to the rapid decay of the static magnetic field strength away from the surface of the sensor.

Our device is designed to perform a non-invasive scan of the skeletal muscle tissue within the lower leg of patients (**Figure 5.1**). These measurements are easily confounded by subcutaneous tissue despite selection of a measurement location with minimal subcutaneous thickness due to limitations in penetration depth ⁷⁸. A measurement technique localized towards the muscle tissue would allow isolation of the muscle signal from nearby confounding tissues.

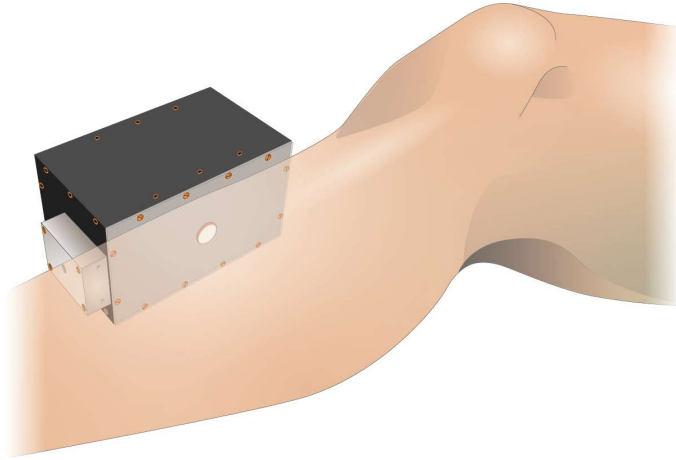


Figure 5.1. Illustration of portable MR sensor adjacent to lower leg of human subject.

We show that tuning the RF excitation frequency of the portable MR sensor allows for spatial selection of the position of the sensitive region. We demonstrate this by measuring the sensitivity of the sensor towards a thin, planar sample as a function of both distance from the sensitive region and RF excitation frequency (B_1) (**Figure 5.2**).

A thin, planar sample was oriented parallel to the surface of the sensor and scanned along a line perpendicular to its surface. The sample consisted of a $380 \mu\text{m} \times 6 \text{ mm} \times 6 \text{ mm}$ pocket machined into PEEK (polyether ether ketone) stock filled with aqueous solution of a paramagnetic species (CuSO_4). PEEK was used as it produced a negligible MR signal. MR measurements via the CPMG pulse sequences were performed with the center of the sample located between 0.690 mm and 6.59 mm from the surface of the sensor.

Measurements were performed with the CPMG pulse sequence with 2000 echoes, an echo time of $65 \mu\text{s}$, a repetition time of 240 ms, a pulse duration of $12 \mu\text{s}$, an acquisition bandwidth of 1 MHz (dwell time of $1 \mu\text{s}$), and 16 acquired points per echo with a Kea2 spectrometer (Magritek, Wellington, New Zealand). The RF excitation frequency was varied across the following range (11.43, 11.49, 11.54, 11.6,

11.63, 11.66, 11.69, 11.72, 11.75, 11.78, 11.81, and 11.83 MHz) in order to identify changes in sensitivity as a function of RF excitation frequency. The amplitude in a triexponential fit (**Eq. (6)**) corresponding to the relaxation peak of the aqueous solution indicated the sensitivity of the sensor.

The sensitivity of the system was characterized as the relative signal strength produced by the sample at each depth position and RF excitation frequency.

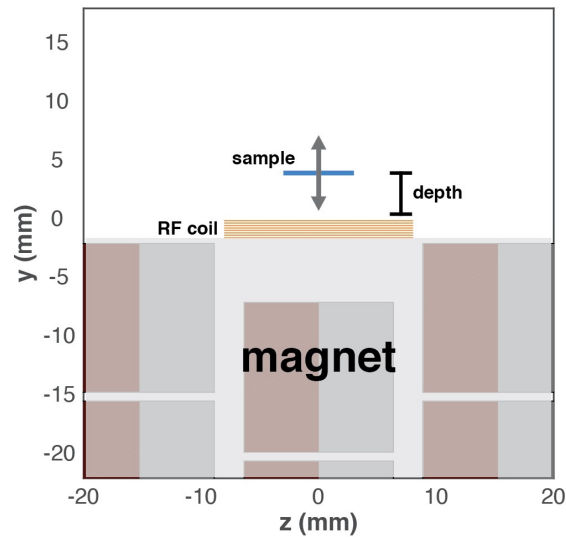


Figure 5.2. Experimental schematic to characterize the sensitivity profile versus depth.

This sensitivity profile varies as a function of depth and exhibits a distinct region of peak sensitivity that is unique to each RF excitation frequency (**Figure 5.3a**). The use of smaller RF excitation frequencies enables localization of the measurement to regions located at a greater distance from the surface of the sensor. The effective slice thickness by a given RF excitation frequency decreases with distance from the sensor at a fixed excitation pulse bandwidth due to the increasing gradient of the static magnetic field (**Figure 5.3b**). We show that an RF pulse bandwidth of 0.7% excites slices 0.6 to 1.3 mm thick with slice thickness decreasing with depth.

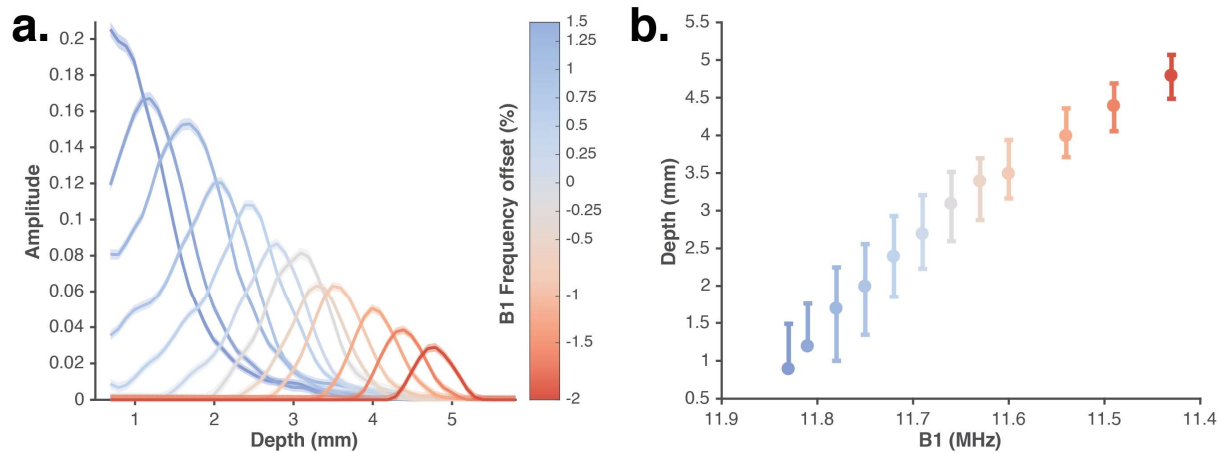


Figure 5.3 Sensitivity profile of portable MR sensor versus depth. **a)** The sensitivity of the sensor as a function of sample depth and RF excitation frequency shows that tuning the RF pulse frequency allows for adjustable sensitivity along the depth axis. Decreased B1 frequency enables deeper measurements remote from the surface of the sensor. Shaded regions indicate 95% confidence intervals of amplitude estimates. **b)** The projection of each curve onto the depth axis shows an RF pulse bandwidth of $\sim 0.7\%$ excites slices 0.6 to 1.3 mm thick with slice thickness decreasing further from the surface of the sensor. Circles indicate the depth of the peak of each sensitivity profile. Whiskers indicate slice thickness defined as full width at half maximum.

The thickness of the effective slice can be tuned by adjusting pulse parameters (e.g. RF excitation bandwidth, pulse duration (**Figure 5.4**), pulse shape, RF excitation frequency).

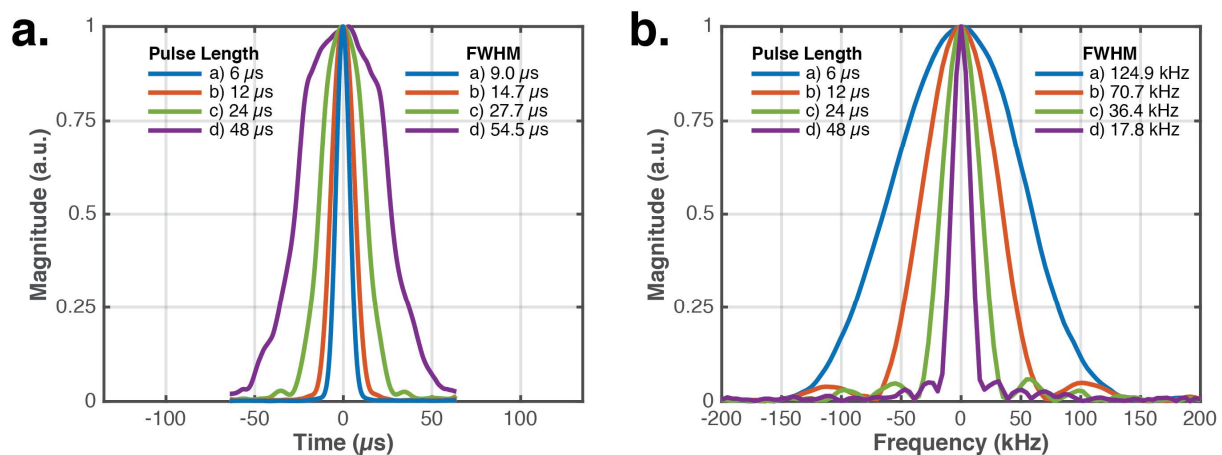


Figure 5.4. Spin echo duration and bandwidth versus pulse length. **a)** time domain and **b)** frequency domain representations of spin echoes from portable MR sensor versus excitation and refocusing pulse length.

A decrease in spin echo duration with decreasing RF excitation frequency indicates a decrease in T2-star due to increased field inhomogeneity with depth (**Figure 5.5**). The sensitivity decreases with increased depth due to increased attenuation of the RF field produced by the transceiver coil.

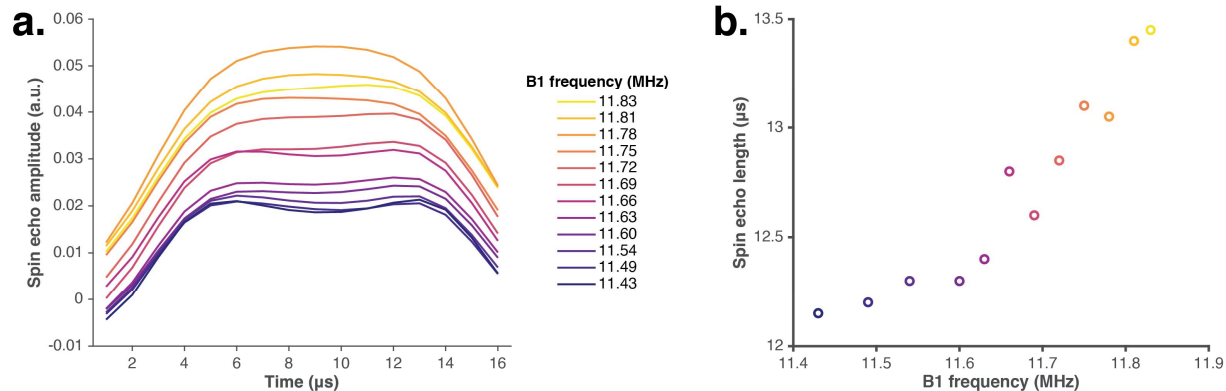


Figure 5.5. Spin echo duration versus RF excitation frequency. **a)** Spin echo amplitude versus time for varying B1 frequencies. **b)** Spin echo length (defined as full-width at half max) versus B1 frequency.

Tuning the RF excitation pulse frequency offers control over the fraction of proximal subcutaneous versus more distal muscle tissue in the acquired signal. This capability enables targeting of the measurement towards a tissue of interest.

5.3 Multicomponent T2 relaxometry enables tissue fraction estimation

The presence of signals from multiple tissues, especially when each produces a distinct multicomponent T2 decay signal, can confound the analysis of a single tissue. Identifying the contribution from each tissue to the measurement allows isolation of each of their signals and further analysis of their relaxation properties.

We demonstrate the identification of tissue fractions from an MR signal acquired with the portable MR sensor. Muscle and fat tissue were extracted from a rat and measured with the CPMG pulse sequence on the sensor to establish reference

signals (**Figure 5.6a**). Tissue was extracted from a Sprague Dawley rat immediately after euthanasia via carbon dioxide inhalation. Muscle and fat tissue was excised from the lower hind limb. Tissue was gently blotted dry with a paper towel to remove excess moisture. Tissue samples were placed into sealed containers to avoid evaporation during MR measurements. In order to prepare the hybrid sample, fresh tissue samples were cut into small (~ 1 mm) pieces, weighed, combined into a heterogeneous mixture, and placed into a sealed container. Portable MR sensor measurements were performed with the CPMG pulse sequence with 8192 echoes, an RF excitation frequency of 11.60 MHz, an echo time of 65 μ s, a repetition time of 1517 ms, a pulse duration of 12 μ s, an acquisition bandwidth of 1 MHz (dwell time of 1 μ s), and 16 acquired points per echo with a Kea2 spectrometer (Magritek, Wellington, New Zealand).

The signals from fat and muscle decay at different rates. The MR signal from each tissue was modeled as a triexponential signal (**Eq. (5)**) allowing the unique relaxation times and amplitudes of each tissue to be identified. Triexponential fits (**Eq. (5)**) of these decay curves show that the relaxation peaks are distinct between muscle and fat (**Figure 5.6b**). A hybrid sample was prepared as a heterogeneous mixture of small (~ 1 mm) pieces of muscle and fat tissue. The hybrid sample has a decay rate between that of its constituent signals (**Figure 5.6a**).

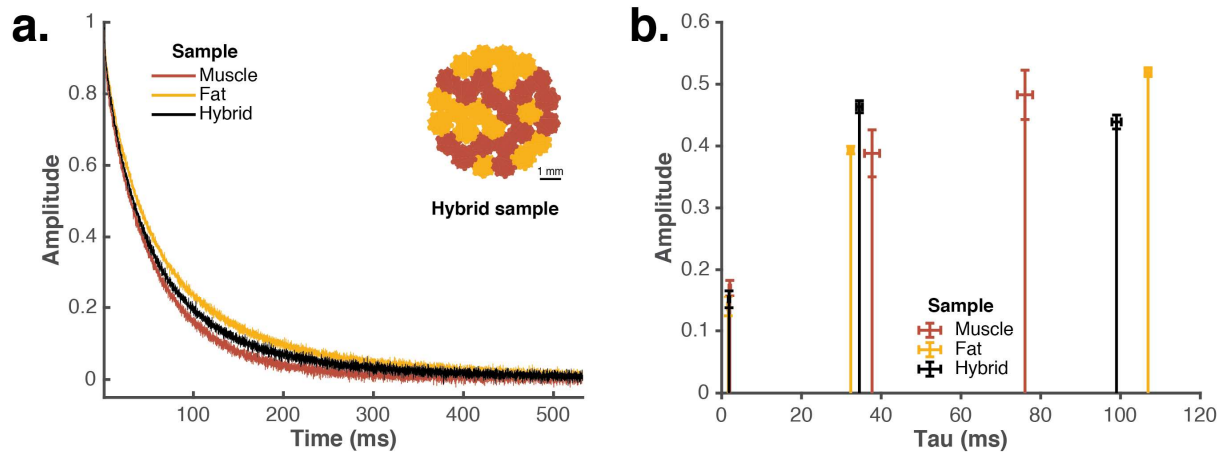


Figure 5.6. Multicomponent T2 relaxometry allows estimation of tissue fraction from a heterogeneous sample. **a)** Time domain CPMG decay curves and **b)** triexponential relaxation peaks of signal acquired from ex vivo muscle, fat, and hybrid sample. Inset in **(a)** illustrates a cross-section of the hybrid sample. Error bars in **(b)** indicate 95% confidence intervals on parameter estimates.

A multiexponential fit of all of the relaxation times from both muscle and fat fails to appropriately assign amplitudes to each of the six constituent relaxation peaks.

Parameter extraction from multiexponential decays is an ill-posed problem, especially when some decay rates are similar. This problem is further exacerbated by the presence of noise. Furthermore, a triexponential fit is sufficient to fully model the multiexponential nature of the hybrid signal, as its residuals are very similar to those of a six exponential fit (**Figure 5.7**). The relaxation peaks of the hybrid sample are each between those of muscle and fat when fit as a triexponential signal (**Figure 5.6b**). Attempting to use the amplitudes produced by the triexponential fit as an estimate of the relative fraction of muscle and fat within the hybrid signal is not possible as each relaxation peak has an unknown contribution from both constituent signals.

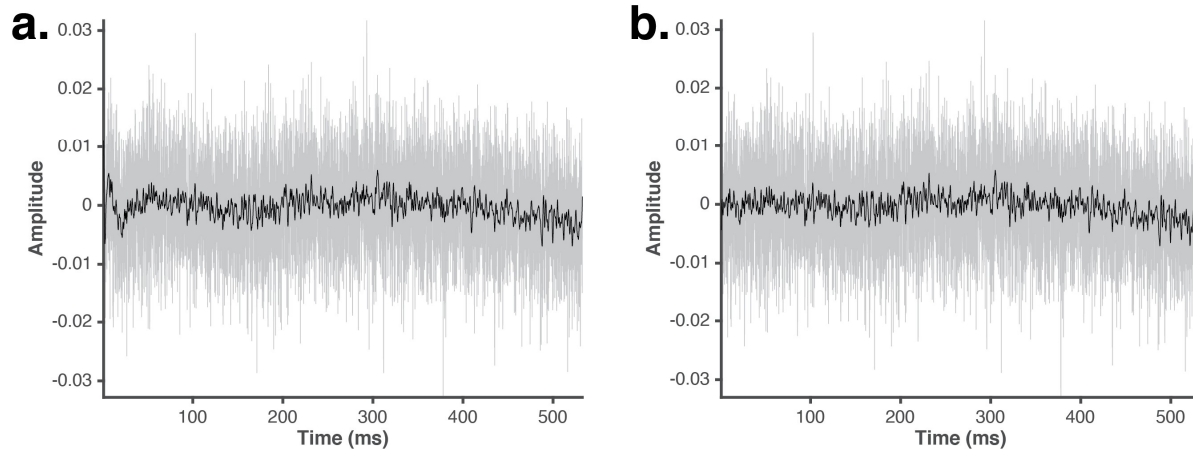


Figure 5.7. Residuals of ex vivo tissue hybrid sample. Residuals from **a)** triexponential and **b)** 6 exponential model. Light grey lines correspond to the raw residuals. Black lines correspond to a low pass filtered (moving average, window size of 15 samples) residual signal.

We developed an algorithm to estimate the fraction of tissues within the hybrid signal through an iterative approach that minimizes the error between the measured signal and a synthetic signal based on an estimated ratio of constituent tissues. This algorithm seeks to identify the tissue fractions (e.g. muscle and fat fractions) within the heterogeneous hybrid sample. A multiexponential fit (**Eq. (5)**) is performed on the hybrid signal to identify the relaxation times, τ , for the algorithm to utilize. A synthetic signal, $\hat{y}_{hy}(t, f)$, is produced as a linear combination of the MR signals from constituent tissues at a specified ratio as shown in (**Eq. (7)**):

$$\hat{y}_{hy}(t, f_{mu}) = f_{mu} * y_{mu}(t) + (1 - f_{mu}) * y_{fa}(t) \quad (7)$$

where f_{mu} indicates the fraction of the signal correspond to muscle, $y_{mu}(t)$ represents the acquired signal from pure muscle tissue, and $y_{fa}(t)$ represents the acquired signal from pure fat tissue. This signal is then fit (**Eq. (6)**) with the previously identified relaxation times to identify the amplitudes, $A_{\tau}^{pred}(f_{mu})$, corresponding to each relaxation time. Similarly, the amplitudes, A_{τ}^{meas} , corresponding to the same relaxation times are found via a multiexponential fit (**Eq. (6)**) with the same previously identified relaxation times. The algorithm seeks to minimize the error between the amplitudes from the measured and synthetic by

adjusting the ratio of constituent signals (i.e. pure muscle, pure fat) used to generate synthetic signal, as shown in **(Eq. (8))**:

$$f_{mu}^{opt} = \underset{f_{mu}}{\operatorname{argmin}} \|A_{\tau}^{pred}(f_{mu}) - A_{\tau}^{meas}\|_2 \quad (8)$$

The error is minimized through the use of an iterative gradient descent algorithm. This technique could be extended towards more than two constituent signals.

This algorithm recovers the fractions of muscle and fat within the hybrid signal to within a 2% error **(Figure 5.8)**. This algorithm performs successfully despite the triexponential nature of each of the constituent signals.

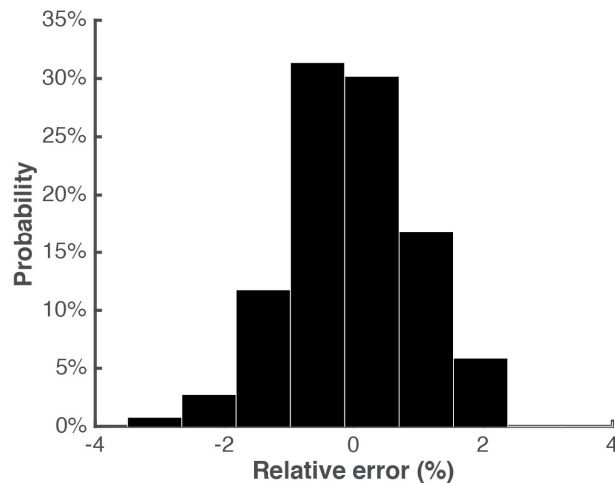


Figure 5.8. Estimation errors from hybrid sample. Histogram indicating the distribution of estimation errors of the constituent tissue fractions within the hybrid sample upon repeated trials.

Our algorithm allows for isolation and further analysis of a signal corresponding to a single tissue despite corruption of the acquired signal by another tissue with similar relaxation peaks. The acquired hybrid signal is unsuitable for standard exponential fitting based analysis methods due to the overlap of the constituent relaxation peaks. This problem is unique to inverse problems comprised of decaying exponentials due to their ill-posed nature ¹²⁵. We demonstrate this algorithm with multiexponential signals acquired from ex vivo fat and muscle tissue. This approach can be applied in other settings, such as estimating the change in relaxation

properties of a single tissue due to a disease or pathology that causes a relaxation time shift within a tissue exhibiting a multiexponential MR signal.

This technique could be extended to consider multiple signals from each constituent tissue in order to improve its robustness, especially towards complex samples. Two measurements could be performed with different sensitivities towards spin diffusivity, for example, for each constituent tissue and for the hybrid sample. The addition of the second signal would increase the orthogonality of the basis signals, if the constituent samples have differences in diffusivity, and, therefore, may increase the accuracy and/or robustness of the technique in the presence of noise or other confounding signals. This same approach could also be applied with other pulse sequences (e.g. inversion recovery, saturation recovery, stimulated echoes, pulsed gradient echo, etc.) to take advantage of differences in T1, T2, and/or diffusivity in combination.

5.4 Depth sensitivity profile and tissue fraction estimation improves muscle measurement localization

The MR signal originating from the more distal muscle tissue is most relevant to the diagnosis of fluid disorders. The optimal measurement with our portable MR sensor would select an RF excitation frequency that sufficiently localizes the measurements towards the muscle tissue without unnecessarily sacrificing sensitivity. Smaller RF excitation frequencies enable increased measurement penetration depth at the expense of sensitivity (**Figure 5.3a**). The optimal choice of RF excitation frequency should be informed by the local variation in subcutaneous thickness where regions with increased thickness will require a decreased frequency to achieve sufficient measurement penetration.

We demonstrate estimation of proximal subcutaneous tissue thickness with the portable MR sensor. We first fabricated synthetic tissue phantoms mimicking the relaxation properties of subcutaneous tissue and muscle tissue via aqueous solutions with varying concentrations of a paramagnetic species (CuSO_4). Synthetic tissue phantoms were fabricated from PEEK film (0.005-inch thickness) and nylon annular rings with an inner diameter of 6 mm and thickness of 1, 1.3, 1.5, and 3 mm with a tolerance of 0.3 mm. Each nylon ring was first bonded to a disk of PEEK film of identical outer diameter. The resultant cylindrical cavity was filled with fluid mimicking the MR relaxation properties of subcutaneous fat (i.e. soybean oil, CuSO_4). Then a second disk of PEEK film was used to seal each phantom.

The phantoms were designed to fully span the sensitive region of the sensor (**Figure 5.9a**). Portable MR sensor measurements were performed with the CPMG pulse sequence with the following parameters common to all scans: 8192 echoes, 1 dummy echo, an echo time of 65 μs , a measurement time of 1065 ms, a repetition time of 1517 ms, a pulse duration of 12 μs , an acquisition bandwidth of 1 MHz (dwell time of 1 μs), and 16 acquired points per echo. RF excitation frequencies of 11.43, 11.53, 11.58, 11.66, 11.73, and 11.83 MHz were acquired. The relaxation times of the synthetic subcutaneous tissue phantom were similar to that of ex vivo tissue while allowing for precise control over sample geometry (**Figure 5.9b**).

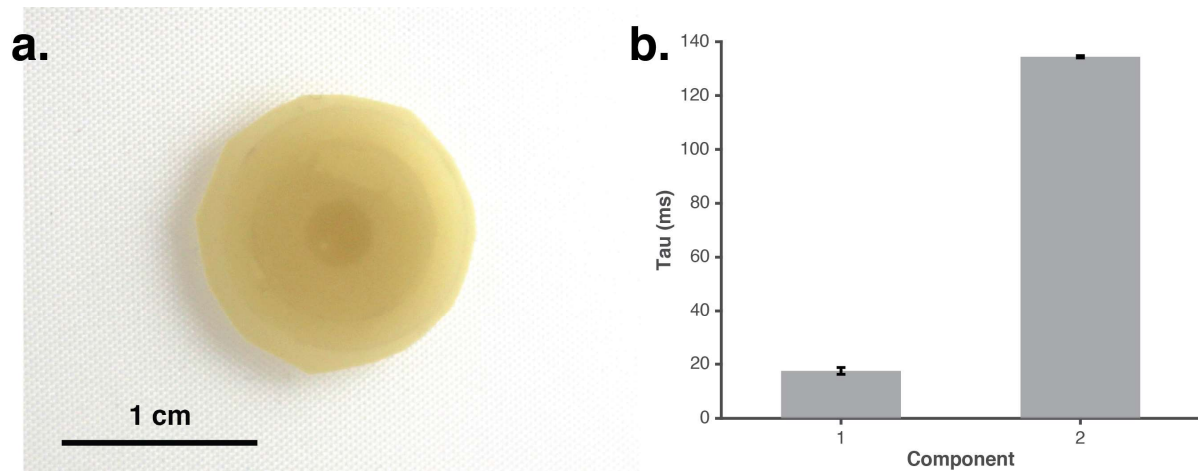


Figure 5.9. Synthetic subcutaneous tissue phantom. **a)** Photograph of phantom shows soybean oil cavity surrounded by a PEEK housing. **b)** A biexponential fit of CPMG signal of soybean oil acquired on portable MR sensor produces two distinct relaxation times. Error bars represent 95% confidence intervals on relaxation time estimates.

The phantoms were then arranged with the subcutaneous tissue directly in contact with the RF coil of the portable MR sensor and the muscle tissue placed against the subcutaneous tissue phantom (**Figure 5.10**). The thickness of the subcutaneous tissue was varied (1, 1.3, 1.5, and 3 mm) to mimic natural variability both within and between patients.

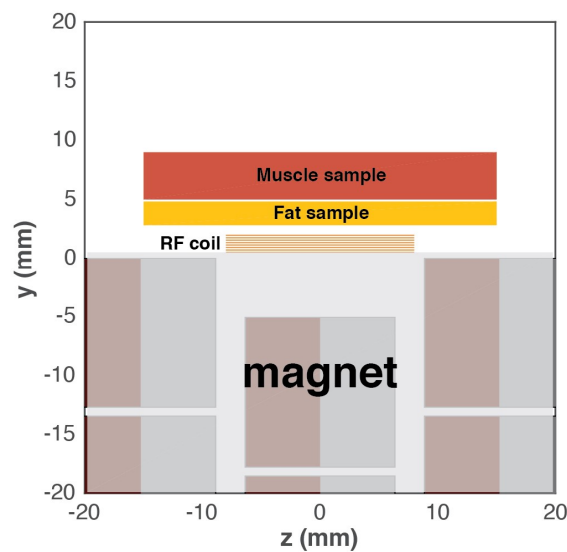


Figure 5.10. Experimental schematic identifying planar subcutaneous and muscle tissue samples on top of portable MR sensor.

We measured each configuration of phantoms with the CPMG pulse sequence with six unique RF excitation frequencies. Simulations were performed to identify the necessary signal to noise ratio (SNR) to accurately estimate the muscle fraction from a heterogeneous signal (**Figure 5.11**). Muscle to fat ratios of 20:80, 50:50, and 80:20 were considered. Signal to noise ratios of each constituent signal (i.e. muscle, fat) of 25, 50, 75, 100, 125, 150, 175, 200, 225, and 250 were considered for a total of 100 pairwise combinations of signal to noise ratios. For each pair of SNRs at each muscle to fat ratio, a synthetic muscle and fat signal at the corresponding SNR was generated based on the relaxation times and amplitudes observed in triexponential fits (**Eq. (6)**) of ex vivo measurements of isolated tissue. A resultant hybrid signal was created as the sum of these two signals. The muscle to fat ratio was estimated using the previously described algorithm. Error was computed as the absolute difference of this estimate from the true muscle to fat ratio. 120 trials were performed for each combination of SNRs and muscle to fat ratios.

The results of this simulation guided measurements of phantoms. The fraction of the signal corresponding to each constituent tissue was estimated using the previously described algorithm.

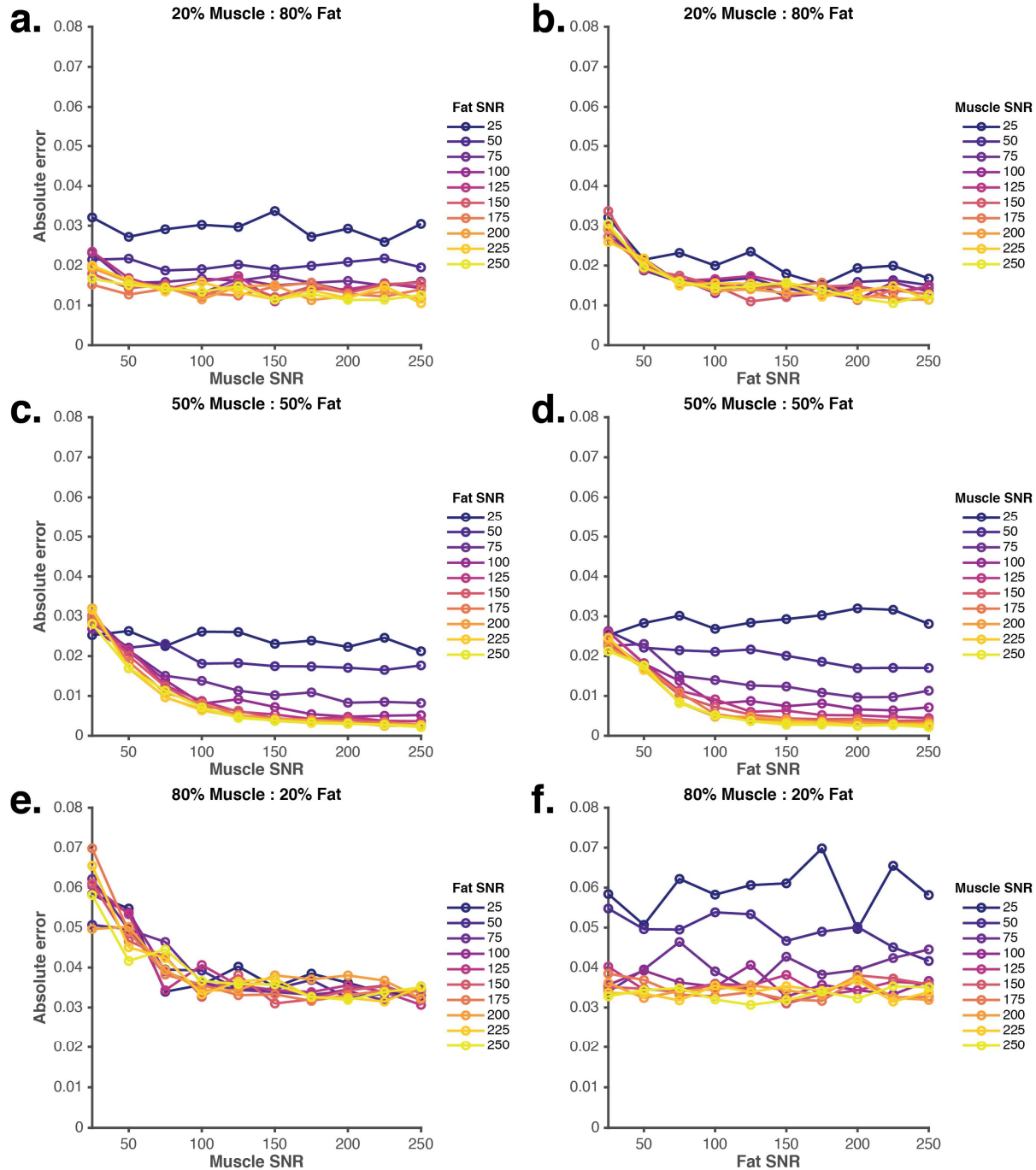


Figure 5.11. Simulation of error in estimating muscle and fat fractions versus signal SNR. Simulations were performed at three muscle to fat ratios: **a-b)** 20:80, **c-d)** 50:50, **e-f)** 80:20.

The expected signal amplitude originating from the distal muscle tissue for a given subcutaneous thickness (e.g. 2 mm) can be estimated as the integral of the sensor sensitivity profile taken across the expected depth of the muscle tissue (e.g. greater than 2 mm) for each RF excitation frequency (**Figure 5.12a**). This can be converted

to an estimate of the muscle tissue fraction by dividing it by the integral of the entire sensitivity profile at the given RF excitation frequency.

The muscle fraction, $f_{mu}^{meas}(B_1)$, was estimated at each RF excitation frequency, B_1 , for each phantom thickness from these measured signals using the previously described algorithm. The relaxation times used for each tissue were derived from monoexponential fits on the synthetic subcutaneous and muscle tissue solutions used within the synthetic tissue phantoms. Muscle fraction, $f_{mu}^{pred}(B_1, z)$, was similarly derived from the depth sensitivity profile data, $A(B_1, z)$, for each RF excitation frequency given a guess of the phantom thickness, z , as shown in **(Eq. (9))**:

$$f_{mu}^{pred}(B_1, z) = \frac{\int_z^{\infty} A(B_1, z) dz}{\int_0^{\infty} A(B_1, z) dz} \quad (9)$$

The thickness of the synthetic fat layer, z^{opt} , was estimated by minimizing the error between the estimated muscle fraction derived from the measured data and the predicted muscle fraction derived from the depth sensitivity profile data, as shown in **(Eq. (10))**:

$$z^{opt} = \underset{z}{\operatorname{argmin}} \|f_{mu}^{meas}(B_1) - f_{mu}^{pred}(B_1, z)\|_2 \quad (10)$$

This technique can be used to precisely quantify subcutaneous tissue thickness from measurements of a muscle sample with a more proximal layer of subcutaneous tissue. Estimates of muscle fraction from experimentally acquired signals show strong agreement with estimated muscle fractions for the same subcutaneous thickness across a wide range of RF excitation frequencies **(Figure 5.12b)**.

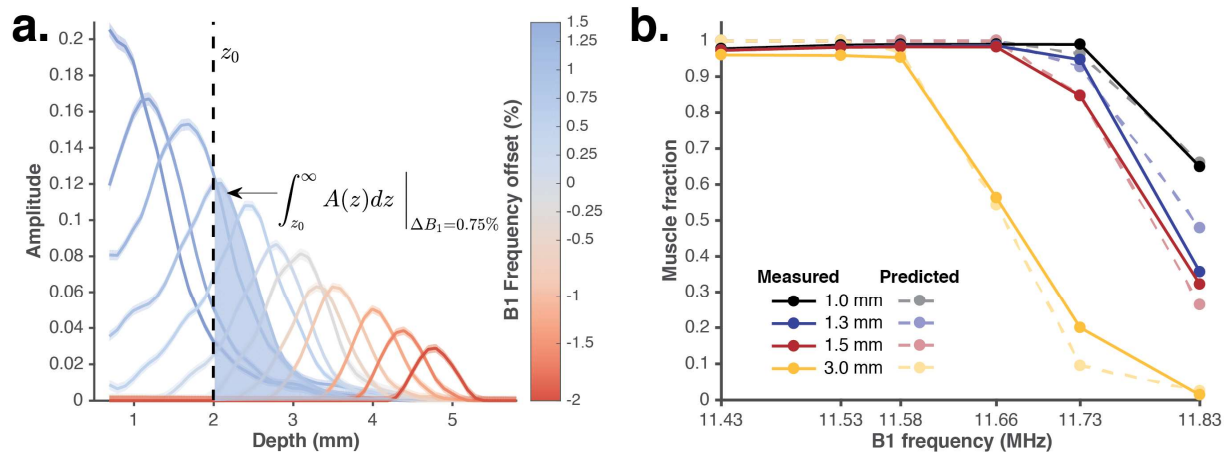


Figure 5.12 Method for estimating proximal subcutaneous tissue thickness. **a)** A schematic illustrating the use of the depth sensitivity profiles to estimate the thickness of a tissue layer. **b)** Experimentally measured and predicted muscle signal fractions from each unique subcutaneous tissue thickness versus RF excitation frequency.

Sensor sensitivity as a function of depth can be used for precise estimation of the thickness of the subcutaneous tissue. The muscle fractions generated by integrating the sensitivity profiles for a candidate thickness can be compared with muscle fractions from experimentally acquired signals. We then identify the optimal candidate thickness by minimizing the error between muscle fraction estimates and those from the measured signal. This optimal thickness represents the actual thickness of each phantom (**Figure 5.13**). Estimation of phantom thickness using this approach is accurate to within 0.1 mm, which is smaller than the tolerance on the construction of the phantoms (0.3 mm). More precisely estimating the depth profile with thinner planar samples could improve phantom thickness estimation accuracy.

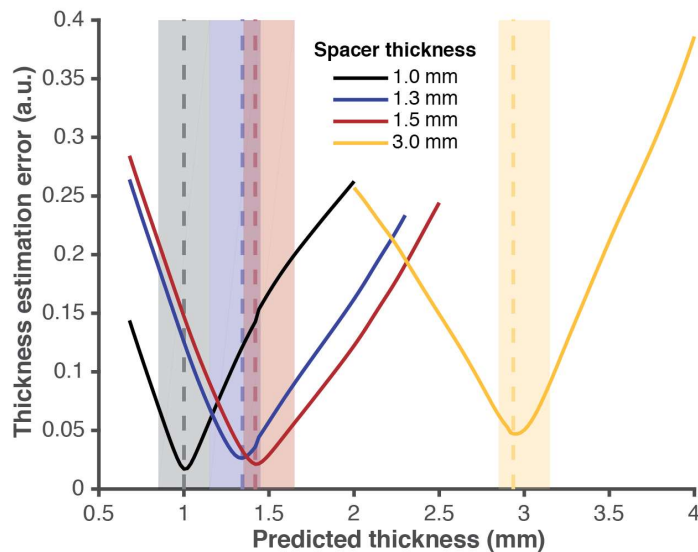


Figure 5.13. Thickness estimation error versus predicted thickness for each unique subcutaneous tissue thickness. Dotted lines indicate the estimated synthetic tissue thickness, corresponding to the minima of each error curve. Shaded regions indicate 0.3 mm uncertainty in the true thickness of each subcutaneous tissue layer.

An algorithm to perform acquisition at the optimal RF excitation frequency could be implemented by utilizing this method. The optimal RF excitation frequency would be sufficiently low as to ensure a significant fraction of the sensitive region is located within the target tissue without being so low as to unnecessarily sacrifice sensitivity. This optimal frequency would be dependent on the subcutaneous tissue thickness, geometry of the portable MR sensor, and pulse parameters (e.g. excitation pulse bandwidth). Estimation of the optimal RF excitation frequency is made more robust and accurate by performing measurements of a tissue geometry at multiple RF excitation frequencies.

5.5 Varying echo time enables sensitivity towards sample diffusivity

Distinct tissues can have very similar relaxation properties (e.g. times and amplitudes) making identification and further characterization of changes in relaxation properties difficult ^{79,126,127}. Measurements of relaxation properties via

CPMG are inherently affected by the diffusivity of spins (e.g. water in tissue) within the sample ¹²⁸. Here we demonstrate that explicitly manipulating the echo time within CPMG allows control over the effect of diffusivity on the relaxation properties of the signal with our portable MR sensor.

Varying the echo time between excitation and subsequent refocusing pulses provides control over the magnitude of signal attenuation induced by sample diffusivity ¹²⁸. Signal attenuation between sequential refocusing pulses in CPMG is driven by both T2 decay and the motion of spins within the magnetic field. The T2 decay term is proportional to the echo time while the diffusion term is proportional to the echo time cubed. Therefore, by controlling the echo time, the relative signal attenuation due to each factor can be varied.

Four aqueous solutions of polyethylene glycol (PEG) and gadolinium were prepared with identical T2 relaxation time and distinct diffusion coefficients. Samples consisted of aqueous solutions of varying concentrations of gadolinium trichloride (Gd) and polyethylene glycol (PEG) (mw: 4000 g/mol). Four samples (A, B, C, and D) were prepared with 126, 57, 28.5, and 0.17 mM of PEG and 0.42, 0.5, 0.5, and 0.5 mM of Gd, respectively. The relaxation data from the benchtop NMR spectrometer were acquired via CPMG with 25000 echoes, an echo time of 100 μ s, a repetition time of 60 seconds, an RF excitation frequency of 19.95 MHz, an excitation pulse duration of 1.9 μ s, an inversion pulse duration of 3.8 μ s, an acquisition bandwidth of 1 MHz (dwell time of 3 μ s), and 1 acquired point per echo with a (minispec mq20, Bruker, USA). The diffusion NMR data was acquired from a Bruker Avance III HD 400 NMR spectrometer with a pulsed gradient spin echo pulse sequence. Estimation of diffusivity was performed with MestReNova v12.0.4 (Mestrelab Software S.L.).

PEG concentration primarily affected the diffusivity of water while gadolinium primarily affected relaxation properties. T2 relaxation times were estimated via measurements on a benchtop NMR spectrometer via CPMG. The time domain signals and T2 relaxation times, estimated via a monoexponential fit, were nearly

identical across all samples (**Figure 5.14a-b**). The diffusivity of water within the samples, estimated via pulsed gradient spin echo pulse sequence on a Bruker NMR spectrometer, varies significantly with PEG concentration (**Figure 5.14c**).

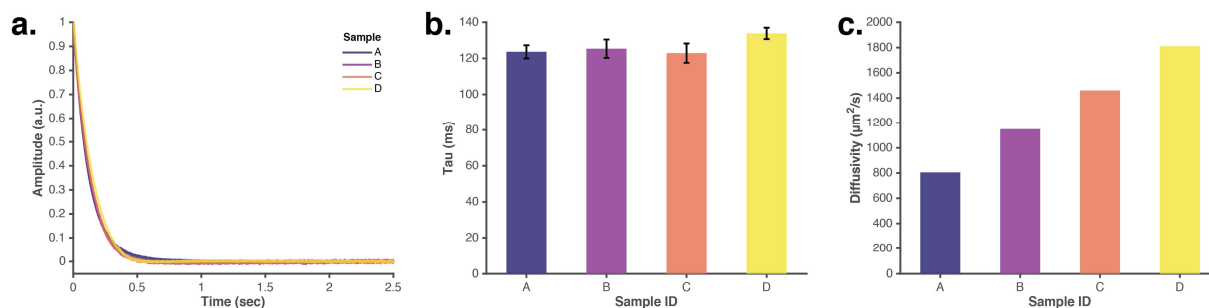


Figure 5.14. Relaxation time and diffusivity of aqueous samples. **a)** Time domain decay curves and **b)** extracted relaxation times from measurement of samples with distinct diffusivities acquired with CPMG on benchtop NMR spectrometer. Error bars represent 95% confidence intervals on relaxation time estimates. **c)** Diffusivity estimated via pulsed gradient spin echo measurements of these samples with an NMR spectrometer.

Measurements of the aqueous solutions were performed with CPMG with varying echo time with the portable MR sensor (**Figure 5.15a**). The data from the portable MR sensor were acquired with the CPMG pulse sequence with the following parameters common to all measurements: a measurement time of 1.065 sec, an RF excitation frequency of 11.66 MHz, a repetition time of 452 ms, a pulse duration of 12 μ s, an acquisition bandwidth of 1 MHz (dwell time of 1 μ s), and 16 acquired points per echo. Echo times of 206, 223, 260, 368, 520, 735, and 1040 μ s were utilized. All relaxation times were extracted by fitting the decay curves with a monoexponential model (**Eq. (5)**).

The change in decay rate in the time domain (**Figure 5.15a**) and estimated relaxation time extracted from a monoexponential fit (**Eq. (5)**) (**Figure 5.15b**) of each sample differs as a function of echo time. Increased echo time leads to a decrease in relaxation time. The magnitude of this decrease is more pronounced with increased sample diffusivity. The relative change in relaxation time as a function of echo time clearly stratifies samples by diffusivity (**Figure 5.15c**). For example, the sample with the highest diffusivity exhibits an 88% decrease in

relaxation time while the sample with the lower diffusivity exhibits only a 19% decrease in relaxation time between the fastest and slowest echo time acquired.

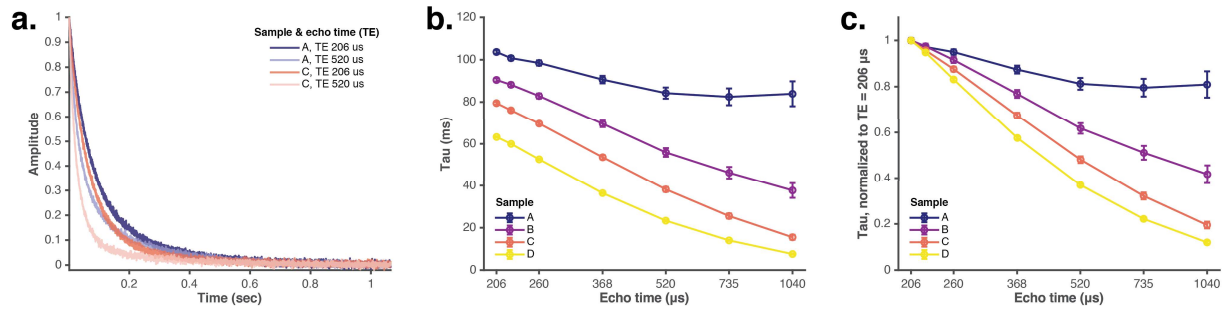


Figure 5.15. Varying echo time provides portable MR sensor with sensitivity towards sample diffusivity in vitro. **a)** Time domain decay curves, **b)** relaxation times, and **c)** relaxation times normalized to the relaxation time at TE = 206 μs from measurements of these samples on portable MR sensor with CPMG with varying echo time. Error bars represent 95% confidence intervals on the relaxation time estimates.

We then measured three distinct ex vivo tissues on the portable MR sensor to demonstrate that this technique is capable of identifying differences in diffusivity within complex samples producing multiexponential signals. Fat, skeletal muscle, and skin are excised from a rat and measured with CPMG with varying echo times. Each tissue was measured with the portable MR sensor with the CPMG pulse sequence with an RF excitation frequency of 11.60 MHz, a repetition time of 1517 ms, a measurement time of 1.065 sec, a pulse duration of 12 μs , an acquisition bandwidth of 1 MHz (dwell time of 1 μs), and 16 acquired points per echo. Echo times of 65, 103, 164, 260, and 520 μs were used in order to identify changes in estimated relaxation time as a function of echo time.

The change in decay rate of each signal is dependent on echo time (**Figure 5.16a**). We then performed a biexponential fit to identify the effect of varying echo time on the amplitude corresponding to the slower, more highly diffusive fluid compartment of each tissue. First, the signals from each tissue across all echo times were summed and fit with a biexponential model (**Eq. (5)**) to identify average two component relaxation times for each tissue. Then for each tissue, each signal at each echo time was fit with a biexponential model (**Eq. (6)**) with the respective relaxation times

corresponding to the tissue. This allowed differences between signals to be identified as changes in the relative amplitudes of the slow versus fast relaxation peaks.

The second amplitude from the biexponential fit of the muscle signal decreases more quickly with echo time than that of the skin or fat signals (**Figure 5.16b**). This shows that the relative diffusivity of water within the slow component of muscle is greater than that of skin and fat ^{129–131}. Furthermore, the relative change in this amplitude as a function of echo time clearly stratifies each tissue which allows for straightforward identification of each tissue despite similarities in relaxation properties (**Figure 5.16c**).

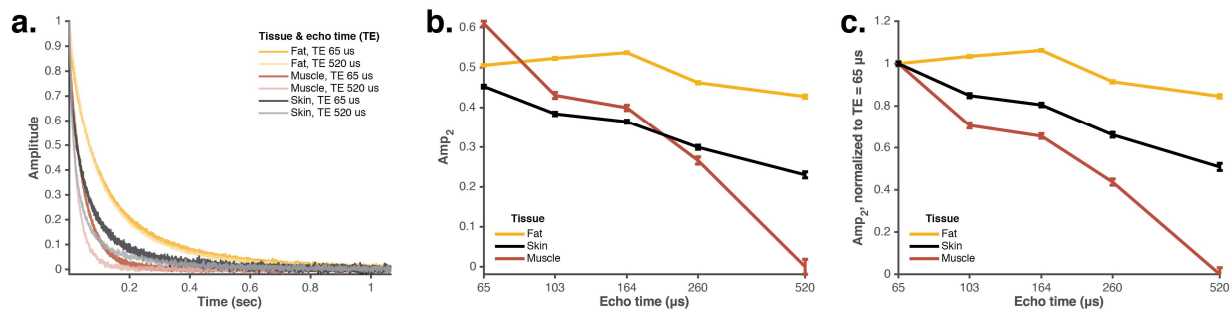


Figure 5.16 Varying echo time provides portable MR sensor with sensitivity towards sample diffusivity ex vivo. **a)** time domain CPMG decay curves of ex vivo tissue measured with portable MR sensor at two echo times. **b)** Slow amplitude (amp₂) and **c)** slow amplitude normalized to slow amplitude at TE = 65 μs of a biexponential fit on these measurements. Error bars represent 95% confidence intervals on amplitude.

We demonstrate sensitivity towards diffusivity with the portable MR sensor by taking advantage of its highly inhomogeneous static magnetic field. This measurement is performed by varying the echo time which serves a similar purpose as the switchable gradient fields found in more traditional implementations of diffusion-weighted pulse sequences. The relatively high static magnetic field inhomogeneity, a characteristic of most single-sided MR sensors, enables strong diffusion weighting to be achieved with relatively short echo times. The dependency of relaxation time on both echo time and sample diffusivity can be used to identify the T₂ and diffusivity of a sample.

5.6 Muscle edema induces shift in multicomponent T2 relaxometry MR signal

We induced acute, focal muscle edema to expand the intramuscular interstitial fluid compartment via injection of λ -carrageenan into the biceps femoris muscle in the lower leg of a rat ^{68,132}. Acute muscle edema was induced via an injection of 200 μ L of 1% λ -carrageenan solution into the biceps femoris of the lower hind leg of a 400 g, male Sprague-Dawley rat. Injections were performed with a 26 gauge needle with the tip of the needle inserted perpendicularly and approximately 4 mm into the skin. The injection was performed at an approximate flow rate of 10 μ L/sec. The needle was held in place for approximately 30 seconds before removing it from the leg to reduce backflow and bleeding. Rats were administered 1 mg/kg of Buprenorphine SR via thoracic subcutaneous injection immediately prior to injection to minimize discomfort. Rats were anesthetized with 2% isoflurane during the injection.

We confirmed the presence of muscle edema via hematoxylin and eosin (H&E) staining of muscle tissue adjacent to the site of injection (**Figure 5.17a-b**). For H&E histology, biceps femoris muscle tissue was excised from a freshly euthanized rat and fixed in formalin for 24 hours at 4 C° and stored in 70% ethanol until paraffin-embedding, sectioning, and staining. Muscle tissue after λ -carrageenan injection shows increased white blood cell infiltration and an expanded interstitial space causing edema.

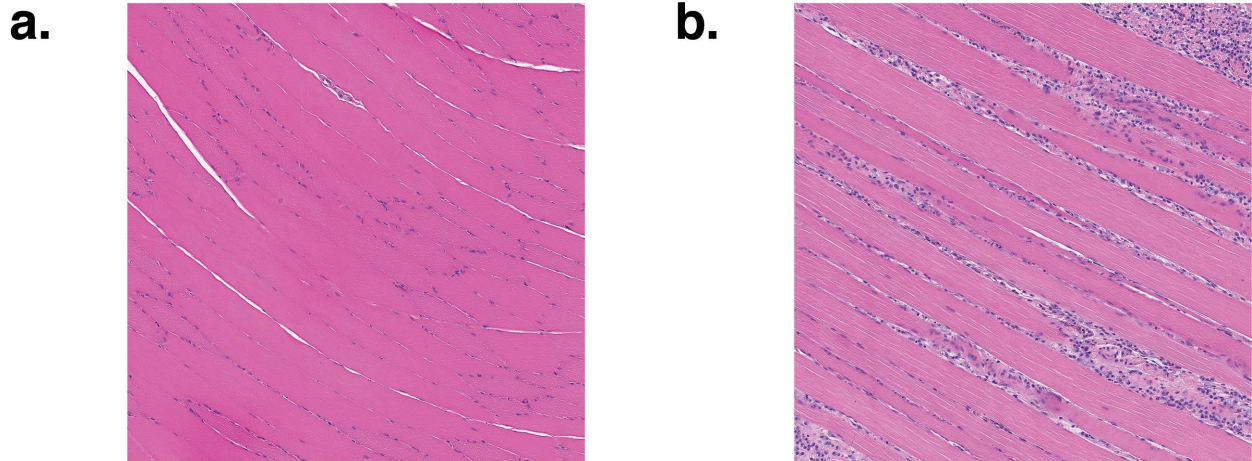


Figure 5.17. Intramuscular muscle edema is evident on H&E staining. **a-b)** H&E stains of biceps femoris muscle **(a)** before and **(b)** after intramuscular injection of λ -carrageenan shows acute inflammation and interstitial expansion.

We further establish the presence of muscle edema via T2-weighted MRI of the lower leg before (**Figure 5.18a**) and after (**Figure 5.18b**) injection. MRI scans were performed with a 7T/310/ASR (Agilent, formerly Varian) scanner with vnmrj software (version 3.2b), equipped with a 63mm/108mm quadrature birdcage coil. Rats were first anesthetized with 2% isoflurane, then oriented in a supine position, and maintained on 1-2% isoflurane throughout data collection. Warm air (37 C) was delivered to maintain body temperature of animals. T2 weighted anatomical scans were performed with FSEMS (fast spin echo multi slice) with repetition time 2000 ms, echo time 20 ms, echo train length 4, kz zero 2, 2 averages, 2 dummy scans, 256 x 256 acquisition matrix, 40 x 40 mm field of view, and 1 mm slice thickness. Slice acquisition order was interleaved using standard two-pass interleaving. All images were acquired along the sagittal plane of the animal.

The region of hyperintensity in the biceps femoris muscle, visible in the image 24 hours after injection, indicates fluid accumulation in the interstitial space (**Figure 5.18b**).

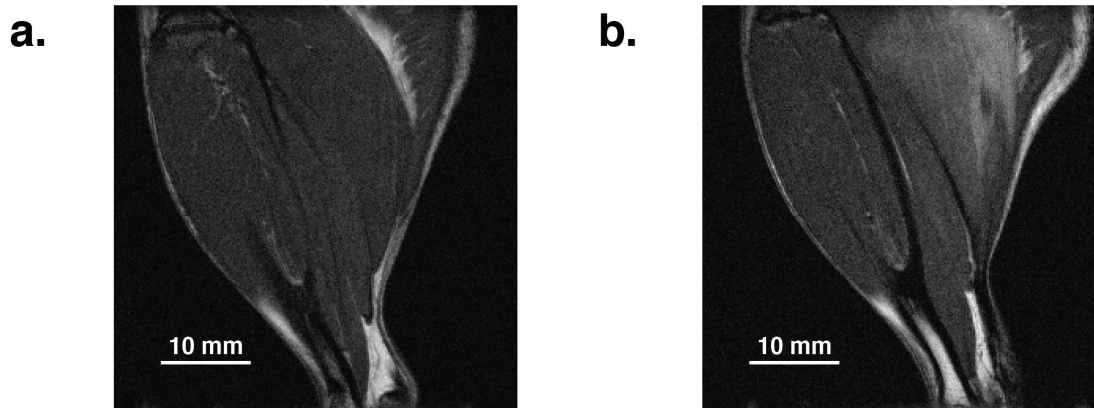


Figure 5.18. Intramuscular muscle edema induces T2weighted hyperintensity. **a-b)** T2 weighted MRI images of rat lower leg **(a)** before and **(b)** after onset of acute muscle edema.

A series of spin echo MRI images were acquired to provide a T2 decay curve for quantitative characterization of muscle edema (**Figure 5.19a-b**). A series of spin echo images for T2 relaxometry were acquired with MEMS (multi echo multi slice) with TR 7600 ms, TE 10 ms, 151 echoes, 4 averages, 64 x 32 x 5 acquisition matrix, 40 x 40 mm field of view, and 1 mm slice thickness. The MRI data are acquired as magnitude images; therefore, the noise distribution is best approximated as a Rician distribution. We transform the noise distribution of each multi-echo signal from Rician to Gaussian by iteratively estimating the variance of the noise, extracting an estimate of the contribution from noise to each echo, then mapping between the cumulative distribution functions of a Rician distribution to a Gaussian distribution^{113,115}. The noise variance is estimated iteratively until the absolute value of the median of the echo magnitude in the noise tail is minimized.

Composite T2 decay signals formed from voxels corresponding to muscle tissue indicate an increase in decay time from before to 24 hours after injection (**Figure 5.19a**). A biexponential fit demonstrates an increase in signal amplitude corresponding to the intramuscular ECF (**Figure 5.19b**).

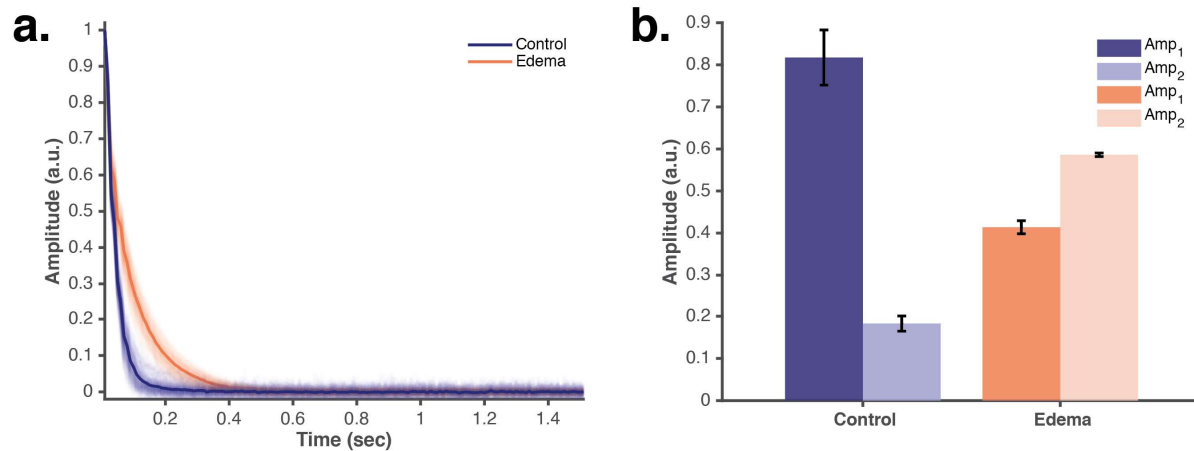


Figure 5.19. Intramuscular muscle edema shifts multicomponent T2 relaxometry signal. **a)** Decay curves from T2 relaxometry acquired via MRI before and after onset of muscle edema show a difference in decay rate. Shaded regions indicate variance in signal generated through bootstrapping. **b)** Relative amplitudes of biexponential fits (**Eq. (6)**) on control and edema echoes. Relaxation times are derived from a biexponential fit (**Eq. (5)**) on the mean of all echoes.

5.7 Measurement of muscle edema despite proximal subcutaneous tissue

We show that the portable MR sensor can identify these changes in intramuscular fluid distribution induced by muscle edema despite the presence of a confounding signal from proximal subcutaneous tissue. We achieved this by localizing the signal via tuning of the RF excitation frequency and by isolating the muscle signal via diffusion-weighted measurements and T2 multicomponent relaxometry.

The hind leg of the rat was placed on top of the RF transceiver coil of the portable MR sensor (**Figure 5.20**). A synthetic subcutaneous tissue phantom, located between the sensor and the rat leg, simulated the presence of a substantial subcutaneous tissue layer. The subcutaneous tissue phantom consisted of a cylindrical volume of soybean oil enclosed in a thin plastic housing (**Figure 5.9a**). The subcutaneous tissue phantom appears as a biexponential signal when measured with the portable MR sensor with relaxation times of 58 and 226 ms (**Figure 5.9b**).

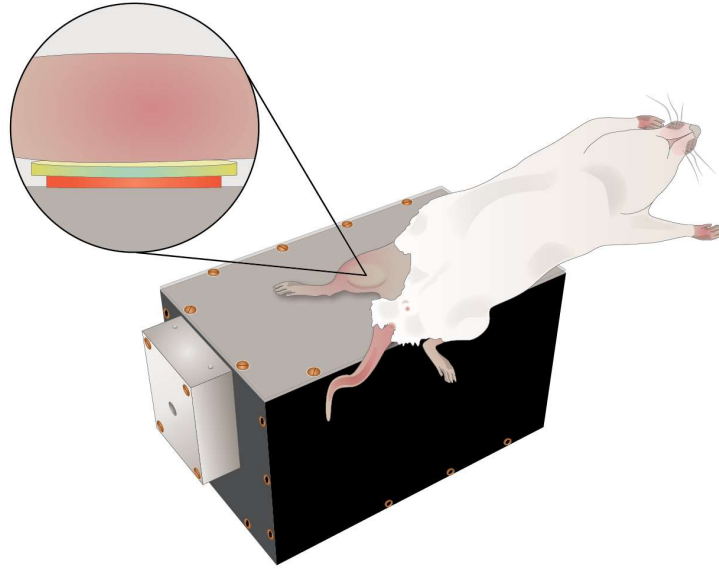


Figure 5.20. Illustration of portable MR sensor with synthetic subcutaneous tissue phantom placed between RF transceiver coil and rat lower leg.

MR measurements were performed before injection and longitudinally at regular intervals for a total period of 121 hours. Anesthetized (2% isoflurane) rats were placed on top of the portable MR sensor in a supine position. The lower leg was positioned on top of the RF coil and secured with tape to minimize motion during signal acquisition. A synthetic subcutaneous tissue phantom was located between the sensor and the rat leg. The phantom consisted of a 2 mm thick cylindrical volume of soybean oil enclosed in a thin PEEK housing. Four measurements were performed with the CPMG pulse sequence with following parameters common to all scans: a repetition time of 1517 ms, a measurement time of 1065 ms, a pulse duration of 12 μ s, an acquisition bandwidth of 1 MHz (dwell time of 1 μ s), and 16 acquired points per echo. The first, second, third and fourth scans were performed with an RF excitation frequency of 11.43 MHz, 11.60 MHz, 11.60 MHz, and 11.83 MHz, respectively. The first, second, and fourth scans were performed with an echo time of 65 μ s, 8192 echoes, and 1 dummy echo. The third scan was performed with an echo time of 260 μ s, 4096 echoes, and 0 dummy echoes. These four measurements were repeated at -4, 5, 17, 29, 45, 72, 93, and 117 hours relative to the time of injection for a total of eight time points.

The first set of MR measurements demonstrates the utility of achieving target localization via tuning RF excitation frequency. A series of MR measurements acquired at a high RF excitation frequency (11.83 MHz) are unable to resolve changes in the signal originating from the muscle tissue as the signal is largely localized towards the proximal subcutaneous tissue (**Figure 5.21a**). Identical measurements performed at a lower RF excitation frequency (11.43 MHz) clearly identify an increase in decay rate associated with onset of muscle edema, followed by a reversion towards the baseline signal (**Figure 5.21b**).

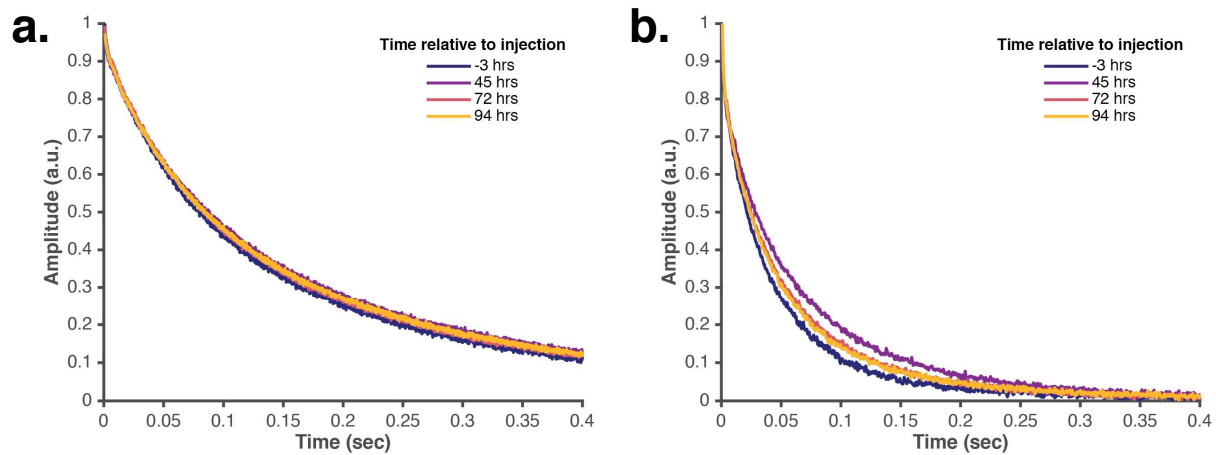


Figure 5.21. Portable MR sensor identifies onset and recovery of acute muscle edema (time domain). Time domain decay curves from portable MR measurement of rat leg at an RF excitation frequency of **B**) 11.83 MHz and **C**) 11.43 MHz.

A triexponential fit (**Eq. (5)**) was performed on the sum of these signals to identify a set of mean relaxation times (2, 40, and 121 ms). A triexponential fit with fixed relaxation times (**Eq. (6)**) was then performed using these relaxation times to identify changes in the amplitude of the slow component that may be attributed to muscle edema. The 11.43 MHz and 11.83 MHz signals at each time point were fit with a triexponential model (**Eq. (6)**) with the relaxation times set to that of muscle tissue. The slowest component was attributed to the extracellular fluid within the muscle tissue (**Figure 5.22a**). The same two signals at each time point were then fit with a five component model (**Eq. (6)**) with the relaxation times set to that of both muscle tissue and subcutaneous tissue. The amplitudes of the two components

corresponding to the subcutaneous tissue were summed and attributed to the subcutaneous tissue. The slowest remaining component was attributed to the extracellular fluid within the muscle tissue (**Figure 5.22b**).

These fits showed that the 11.83 MHz signals for all time points solely comprise the slow component corresponding to the subcutaneous tissue (**Figure 5.22a**). This precludes the use of these measurements to identify muscle edema. In contrast, the amplitude of the same component in the 11.43 MHz signal responds to intramuscular interstitial fluid shifts concomitant with muscle edema. This signal shows a significant response to the onset of edema ($n = 42$ and 41 , $p < 0.0001$, statistics by t test), its consistent progression ($n = 5$, $p < 0.01$, statistics by significance of Spearman rank correlation), and its ultimate recovery towards baseline ($n = 52$ and 45 , $p < 0.0001$, statistics by t test). This process was then repeated with a five exponential model (tau: 2, 40, 58, 121, and 226 ms) to capture the triexponential signal corresponding to the muscle and the biexponential signal corresponding to the subcutaneous fat tissue (**Figure 5.22b**). The subcutaneous fat signal comprises the majority of the 11.83 MHz signal with a negligible fraction being assigned towards the muscle extracellular fluid (ECF). The muscle ECF signal in the 11.43 MHz signal responds to intramuscular fluid shifts while the amplitude of the subcutaneous fat signal remains approximately constant. This signal, once again, shows a significant response to the onset of edema ($n = 42$ and 41 , $p < 0.0001$, statistics by t test), its consistent progression ($n = 5$, $p < 0.01$, statistics by significance of Spearman rank correlation), and its ultimate recovery towards baseline ($n = 52$ and 45 , $p < 0.0001$, statistics by t test). A small increase in the subcutaneous fat signal at 29 and 45 hours was likely leakage of the muscle ECF signal due to both increased amplitude and relaxation time as a result of the onset of edema.

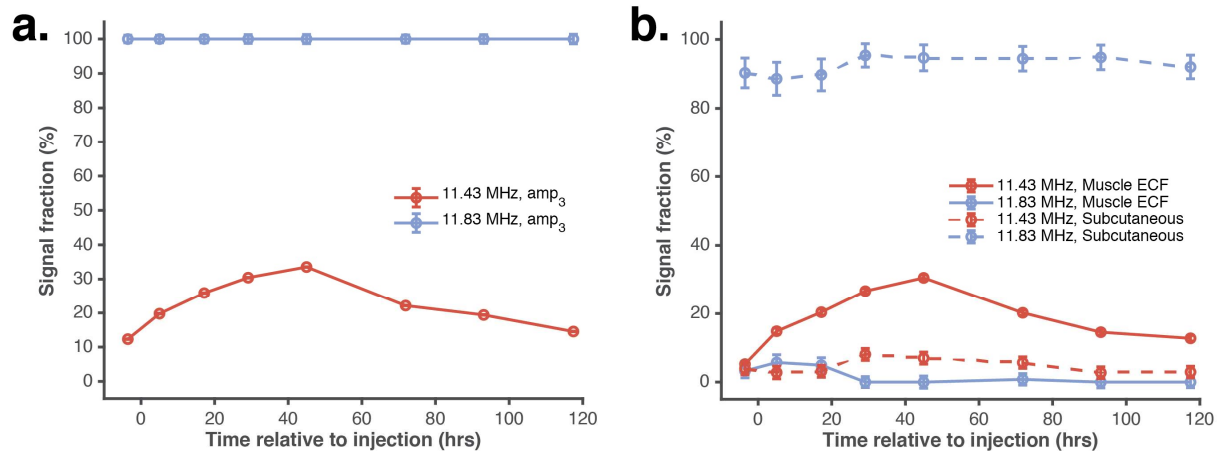


Figure 5.22. Portable MR sensor identifies onset and recovery of acute muscle edema. **a)** Slow amplitude of triexponential fit on 11.43 MHz and 11.83 MHz measurements. **b)** Amplitude attributed to muscle ECF and subcutaneous signal from a five exponential fit on 11.43 MHz and 11.83 MHz measurements. All error bars indicate 95% confidence intervals on amplitude estimates.

The measurement of a region with a considerable fraction of subcutaneous tissue may be unavoidable, even with tuning of the RF excitation frequency, in cases of substantial subcutaneous thickness. In addition, it may be desirable to select a higher RF excitation frequency to decrease total acquisition time though the measurement may include some subcutaneous signal. In these cases, the aforementioned technique may be unable to resolve changes in the relaxation properties of the muscle. The use of a diffusion-weighted signal can help resolve signals originating from tissues or fluid compartments with distinct diffusivities. Measurements during the onset and recovery of muscle edema were performed at an RF excitation frequency of 11.60 MHz, representing a target region spanning both the subcutaneous tissue and the muscle tissue. These measurements were performed at an echo time of 65 μs , similarly to previous measurements, and an additional echo time of 260 μs which applied increased diffusion weighting. The amplitudes of the slow component in a triexponential fit, corresponding primarily to the muscle ECF signal, at an echo time of 65 μs did not vary appreciably in response to muscle edema (**Figure 5.23**). This signal fails to identify the onset of edema ($n = 40$ and 39 , $p = 1.0000$, statistics by t test) or its progression ($n = 5$, $p = 0.1167$, statistics by significance of Spearman rank correlation) though it does

identify the recovery towards baseline (n = 47 and 39, p < 0.0001, statistics by t test).

The amplitudes of this muscle ECF signal at an echo time of 260 μ s decreased in response to muscle edema due to the increased diffusivity of water within the interstitial space ¹³². This diffusion-weighted signal can enhance the signal corresponding to the muscle ECF without bias from the subcutaneous tissue signal (**Figure 5.23**). We first identify the expected muscle ECF signal fraction at an echo time of 260 μ s based on the known sensitivity profile of the MR sensor at 11.60 MHz. The deviation from this baseline muscle ECF signal fraction observed in the 260 μ s signal is due to the increased diffusivity of the muscle ECF in response to muscle edema, which we observe as signal attenuation. The difference of the 260 μ s muscle ECF signal amplitude from the reference value is used to enhance the 65 μ s muscle ECF amplitude.

In order to estimate the degree of diffusion attenuation, Δ , a baseline value, $A_{260\mu s}^{baseline}$, for muscle ECF fraction in the 11.60 MHz 260 μ s signal is first established. The deviation from this baseline of the muscle ECF amplitude of the 11.60 MHz 260 μ s signal, $A_{260\mu s}$, is used to establish an estimate of the signal attenuation due to increased diffusivity of the muscle ECF, as shown in (**Eq. (11)**):

$$\Delta = \frac{A_{260\mu s}^{baseline} - A_{260\mu s}}{A_{260\mu s}^{baseline}} \quad (11)$$

This estimate of increased diffusivity is used to enhance the muscle ECF amplitude from the 11.60 MHz 65 μ s signal. The relative decrease in the signal is used to scale the muscle ECF amplitude of the 11.60 MHz 65 μ s signal (**Figure 5.23**) to produce an adjusted estimate of the muscle ECF amplitude, $A_{65\mu s}^{adj}$, as shown in (**Eq. (12)**):

$$A_{65\mu s}^{adj} = A_{65\mu s} * (1 + \Delta) \quad (12)$$

This adjusted signal more strongly identifies the expected expansion ($n = 5$, $p < 0.05$, statistics by significance of Spearman rank correlation) and subsequent depletion ($n = 49$ and 41 , $p < 0.0001$, statistics by t test) of the muscle ECF in response to muscle edema.

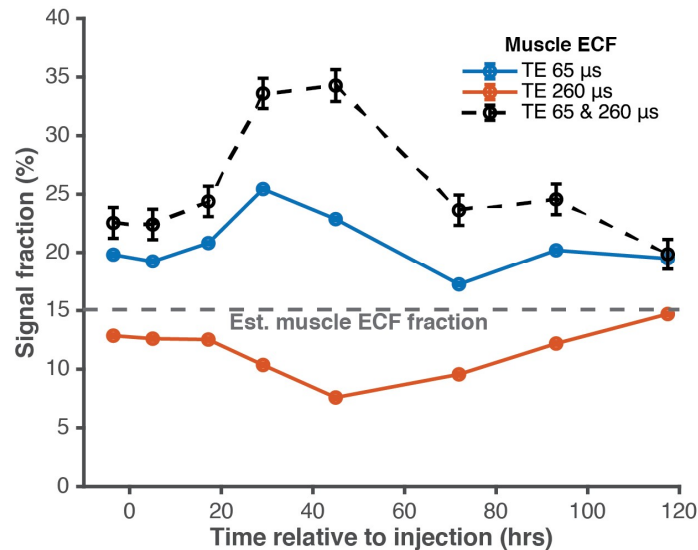


Figure 5.23. Muscle signal enhancement with diffusion weighting. Amplitude attributed to muscle ECF from 11.60 MHz measurements at echo times of 65 μ s (blue) and 260 μ s (orange). Black dashed line indicates estimated muscle edema derived from both measurements. All error bars indicate 95% confidence intervals on amplitude estimates.

The portable MR sensor can identify the progression of acute muscle edema, which is utilized here as a model for fluid accumulation in the intramuscular ECF. In cases of moderate subcutaneous tissue thickness, the increased penetration depth offered by varying the RF excitation frequency serves to localize the measurement completely within the muscle tissue. In circumstances where the subcutaneous thickness is more substantial and localization by tuning the RF excitation frequency is insufficient, a diffusion-weighted measurement can help identify changes in the signal that are associated with fluid shifts within the intramuscular ECF. The combination of diffusion-weighted, depth-resolved multicomponent T2 relaxometry with a single-sided MR sensor offers the unique ability to identify shifts in tissue fluid distribution despite the presence of confounding tissue layers.

5.8 Discussion

The ability to accurately monitor the volume status of end-stage renal disease patients during hemodialysis would inform fluid removal and improve treatment outcomes ^{22,42,45,53}. Excess fluid removal induces intradialytic hypotension, which is associated with adverse outcomes including increased mortality and decreased long-term compliance with hemodialysis prescription ^{43,45,133}. The majority of patients undergoing hemodialysis will experience intradialytic hypotension ¹⁶. Improved identification of overload in these patients may better inform fluid removal during hemodialysis to achieve dry weight while avoiding intradialytic hypotension ⁵⁰. A portable, non-invasive MR sensor of tissue fluid distribution can provide information on systemic volume status via measurements localized to the muscle ^{63,124}. Our prior clinical study demonstrated the need for improved measurement localization within the muscle to make an absolute determination of volume status.

We demonstrate the combination of three techniques – multicomponent T2 relaxometry, measurement localization by tuning RF excitation frequency, and diffusion weighting by varying echo time – to improve the ability of portable, single-sided MR sensors to identify shifts in intramuscular fluid distribution. We first introduce the implementation of these techniques via *in vitro* and *ex vivo* tissue models. We then exhibit the utility of these techniques in an *in vivo* model of localized muscle edema in a rat. These measurement techniques have the potential to improve the management of patients undergoing HD through real-time monitoring of fluid volume status.

We utilized a model of acute, local inflammatory muscle edema in a rat to investigate fluid shifts within muscle expected in patients experiencing volume overload. An intramuscular λ -carrageenan injection is known to induce inflammation followed by subsequent hyperemia and edema ^{68,132,134}. This leads to expansion of the interstitial space within the muscle due to an influx of free fluid

^{73,132}. We validate this model by observing an increase in relaxation time within the muscle with T2-weighted MRI.

This model of acute muscle edema induced intramuscular ECF expansion. The techniques demonstrated here to measure localized edema can be applied towards other disorders which manifest as intramuscular ECF imbalances, such as fluid overload and fluid depletion (dehydration). Fluid overload causes intramuscular ECF expansion as excess fluid shifts from the vasculature to the interstitial space ^{60,135}. Similarly, fluid depletion in the form of dehydration leads to intramuscular ECF depletion as fluid shifts from the interstitial to the vascular space to maintain electrolyte and osmotic balance ^{1,58}.

We use this model to demonstrate that a portable MR sensor can identify changes in intramuscular fluid distribution. Our method interrogates the underlying physiology as multicomponent T2 relaxometry directly resolves the extracellular and intracellular fluid spaces ^{71,72,74}. This differs from other methods currently used to manage patients with fluid disorders. In hemodialysis patients, for example, blood pressure is commonly used to assess volume status. Blood pressure measurements are unable to specifically identify systemic fluid shifts as they cannot distinguish between changes in systemic volume status and in cardiovascular function due to disease. Similarly, dehydration is often assessed via body weight change, but variability in body composition between patients prevents this simple measure from accurately identifying the onset of clinical dehydration. Ultimately, these techniques do not interrogate the status of the muscle, which serves as the primary fluid reservoir in both fluid overload and depletion. Our method overcomes these limitations and, therefore, has the potential to serve as a useful diagnostic of disorders in fluid volume status.

We demonstrate techniques to enable the use of single-sided MR sensors to interrogate muscle tissue across diverse patient populations. The single-sided MR device utilized here is based on the Unilateral Linear Halbach magnet array ¹⁰⁴.

This design enables high sensitivity, remote MR measurements via compact permanent magnet array. Subcutaneous tissue confounds our measurement of the muscle and its thickness varies between patients. The tuning of RF excitation frequency enables measurements at an increased depth to avoid more proximal subcutaneous tissue. Additionally, the use of diffusion weighted measurements allows for further isolation of the signal towards the muscle.

Several improvements to the MR sensor and the described methods could improve its ability to perform measurements of tissue fluid distribution. Diffusivity was not directly quantified in these measurements because of the presence of a spatially varying static magnetic field gradient and restricted diffusion within tissues^{128,136-139}. Additional characterization of the sensor would be necessary to extract an accurate estimate of diffusivity. The CPMG pulse sequence was utilized to take advantage of its high sensitivity, robustness to field inhomogeneity and simplicity. Hardware limitations prevented implementation of more sophisticated pulse sequences that more directly enable estimation of sample diffusivity versus T2¹⁴⁰. An improved pulse sequence could simultaneously acquire depth-resolved, diffusion-weighted T2 measurements. In this work, we used an acute model of muscle edema in rodents. This served to provide an appropriate model to demonstrate the utility of these measurements. Future studies could investigate the physiology of systemic fluid overload in rodents or humans. Additionally, we simulated variability in subcutaneous tissue thickness with synthetic tissue phantoms. A subsequent study could assess this technology in human subjects with naturally varying subcutaneous thickness. We did not quantify water diffusivity or T2 within samples as this would require precise characterization of the static and RF magnetic fields of the sensor. Furthermore, restricted diffusion as observed in tissues creates a complex multiexponential decay that further complicates quantitative analysis^{137-139,141}. Quantitative parameter extraction is not necessary for this technology to provide diagnostic value as empirical thresholds can be derived through further clinical studies.

In summary, we demonstrate that the combination of depth-resolved, diffusion-weighted multicomponent T2 relaxometry can enable a portable, single-sided MR sensor to measure disruptions in intramuscular fluid distribution. Identification of muscle edema in an in vivo rat model shows that this approach can overcome proximal subcutaneous tissue and isolate the muscle tissue signal. These techniques can be applied to provide a non-invasive measure of fluid volume status in humans despite highly variable subcutaneous tissue thickness. This approach may ultimately serve as a real-time, point-of-care indicator of euvolemia and improve the management of end-stage renal disease patients during hemodialysis.

Chapter 6

Perspectives and future directions

6.1 Introduction

Unmanaged volume overload and volume depletion are significant health challenges to the modern healthcare system. The challenge of accurate, timely, straightforward diagnosis and identification of volume imbalances extends beyond hospitals and includes outpatient facilities and community healthcare settings. Fluid depletion is associated with worsened health outcomes in patients affected by chronic diseases, elderly and intensive care patients, and patients recovering from surgery²⁻¹⁰. Unmanaged volume overload increases mortality of patients experiencing organ failure, especially end-stage renal disease (ESRD). Clinicians and patients lack a simple and reliable tool to measure the extent of fluid imbalance to assist with long-term fluid management.

This thesis first outlined a new concept and design framework for permanent magnets within single sided magnetic resonance sensors in Chapter 2. This design allows for high sensitivity, sweet-spot measurements in a region remote from the surface of the sensor. This allows a compact portable sensor to make measurements of a larger sample such as a portion of skeletal muscle within a human leg.

A portable MR sensor for human clinical use was then designed and fabricated based on this framework in Chapter 3. The sensor was characterized and shown to accurately measure the relaxation properties of both single component and multi

component samples via T2 relaxometry. Furthermore the sensor performed this measurement in a highly localized region remote from its surface.

Chapter 3 builds on this work and shows that multicomponent T2 relaxometry localized to the skeletal muscle can identify and, in some cases, quantify fluid loss induced by dehydration. This is demonstrated with both gold-standard MR techniques as well as our portable MR sensor. This work supports the existing literature and shows that the interstitial fluid within the muscle compartment is the most highly responsive to fluid imbalances.

We then turn towards clinical translation of this technology in Chapter 3. The primary challenge in using a miniaturized MR sensor in humans is penetration depth. We demonstrate increased penetration depth and isolation of the muscle signal by leveraging the unique geometry of the portable MR sensor along with new applications of MR pulse sequences. We show that by combining multicomponent T2 relaxometry, tuning of the RF excitation frequency and control over echo time, we can increase penetration depth and enhance the signal from the muscle tissue despite a confounding subcutaneous tissue layer.

There are three primary directions for future directions in advancing portable MR sensors into the clinic for the measurement of fluid volume status. The first is a new design for a portable MR sensor that allows for increased penetration depth and higher sensitivity. The second direction is applying new acquisition strategies to more efficiently and specifically identify the distribution of fluid within the muscle compartment. Finally, the critical next step for this technology is a human clinical study in a representative patient population to understand how this technology might ultimately demonstrate clinical utility.

6.2 New portable MR sensor design

A new portable MR sensor could be designed which will allow for increased sensitivity towards human skeletal muscle tissue. A larger magnet could be designed that would straightforwardly allow for increased penetration depth. Further optimization of the Unilateral Linear Halbach array would allow increases in penetration depth. Allowing the magnet to have a concave surface that better conforms to the contour of the lower leg would increase the amount of magnetic material near the muscle tissue and, therefore, increase the field strength. A series of magnets could be designed with curvatures matched to that of the range of anatomy expected in the target population. Alternatively, a deformable magnet geometry could be utilized that allows a single magnet to adapt to the anatomy of each patient. The geometry could be unilateral or circular to allow for more precise design of the field profile and strength at the tissue of interest.

This new magnet could include adjustment shims in its design. This would enable minor imperfections in the magnetization of the constituent permanent magnets to be compensated. This would result in increased field homogeneity, an increased $T2^*$ and ultimately higher sensitivity measurements. A magnet could also be fabricated from a few very large permanent magnets to increase the density of magnetic material within the housing. This is challenging due to variability in the manufacturing process, the safety risks posed by working with large magnets, and limited ability for shimming during magnet construction. The shimming could be tunable in real-time to allow for shimming of the main magnetic field during scanning. This would allow for precision tuning of the sensor sensitive region based on patient physiology, patient disease status, or environmental factors.

The new sensor should include the ability to adjust its excitation and acquisition frequency with minimal latency and user interaction. Currently, the matching circuit requires manual adjustment when the RF frequency is changed since it only provides a very narrowband match. A new circuit could either provide for a broadband match across a wider range of frequencies or the ability to be rapidly tuned in an automated fashion.

The new sensor could include gradient encoding coils to enable stronger diffusion-weighted acquisition. Existing single sided sensors typically rely on the gradient within the static magnetic field. This provides limited control over the magnitude of diffusion encoding and no control over its direction.

The new sensor could include multiple coils, either separate transmit and receive coils or multiple transceiver coils. Multiple transceiver coils would allow for parallel acquisition of a single patient at different points along their physiology. Parallel scanning of patients would allow for decreased acquisition time without a loss of signal.

6.3 New acquisition strategies

The ultimate goal of this system is to perform a measurement of the distribution of fluid within the muscle compartment in order to detect systemic fluid imbalances. Efforts to date have focused on multicomponent T2 relaxometry because it provides a tractable design goal for an MR system, is straightforward to relate to physical changes in fluid distribution, and is amenable to efficient MR acquisition strategies. Future work should consider the use of both traditional pulse sequences outside of CPMG as well as new approaches based on compressed sensing, dictionary-based approaches, and adaptive acquisition strategies.

Additional parameters of interest for new acquisition strategies include T1, proton density, diffusivity, and magnetization transfer. Although there are well established pulse sequences available to interrogate these properties with single sided MR systems, they often require additional capabilities that our existing spectrometer could not provide and negatively impact acquisition time. A new sensor design optimized for sensitivity in the muscle tissue will alleviate some of these considerations.

Multidimensional NMR provides a promising avenue for exploration as it allows the relationship between two or more of these MR parameters to be characterized ¹⁴². This increased specificity towards fluid compartments could allow for improved characterization of each of their distinct MR properties. The downside of multidimensional NMR techniques is their significantly increased acquisition time. Traditional approaches can increase acquisition time by orders of magnitude limiting their utility in a clinical diagnostic.

New approaches in magnetic resonance that rely upon sparsely sampling parameter space and highly regularized reconstruction offer a path towards highly accelerated multidimensional measurements ^{143,144}. These techniques rely on the fact that the signal generated by a magnetic resonance sensor redundantly represents data when transformed into particular domains or bases.

For example, a dictionary-based approach could be used with a single sided portable MR sensor to identify fluid imbalances. A simulated dictionary could be generated given a particular sensor geometry, range of possible MR parameters and anatomies expected from the target patient population, and pseudorandom pulse sequences. The dictionary could be designed to allow identification of tissue MR parameters or to directly estimate fluid volume status. An acquired signal could then be matched to a simulated signal from the dictionary to identify the best approximation of the MR parameters and/or fluid volume status of the tissue. This could result in a more robust or more efficient acquisition strategy.

Adaptive acquisition strategies could be employed to more efficiently learn the anatomy and MR parameters of the target tissue (e.g. muscle). These methods could be designed to optimize for a particular metric (e.g. muscle fraction within the signal) and then iteratively adjust acquisition parameters (e.g. RF excitation frequency) in order to maximize this metric. Direct optimization using standard gradient descent algorithms may become unfeasible in more complex settings. This could occur if there are multiple metrics or acquisition parameters. New techniques

from machine learning, such as reinforcement learning, are designed to learn optimal policies, or sequences of decisions, to achieve a particular goal with a dynamic environment. These methods have been successfully applied to MRI acquisition problems ¹⁴⁵. A reinforcement learning approach towards dynamic signal acquisition could improve the efficiency and robustness of parameter extraction via signal sided MR measurements.

6.4 Clinical study in ESRD patients

6.4.1 Clinical motivation

A human clinical study in a representative patient population will help improve our understanding of this technology might ultimately demonstrate clinical utility. End stage renal disease (ESRD) patients represent a patient population that both experiences significant fluctuations in volume status regularly and would benefit from improved measurement of fluid volume status. Long-term volume overload and poorly managed ultrafiltration rates are also common ^{48,49}. Clinical assessments are subjective and, in many cases, unable to predict fluid overload ⁵⁴. Clinicians and patients lack a simple and reliable tool to measure the extent of fluid overload to assist with long-term fluid management.

A next-generation portable MR sensor would used in the proposed study to perform a rapid measurement of volume overload in ESRD patients during hemodialysis (HD). These miniature MR devices will perform measurements localized exclusively to the muscle tissue while avoiding the subcutaneous space. This may enable clinicians to quickly assess the volume status of patients during HD which allows for more accurate and rapid control over ultrafiltration volume. We envision our technology serving as the benchmark for the quality of clinical care administered during HD.

This could enable substantial improvements in fluid management for HD patients by providing a real-time assessment of volume status to clinicians. This information could enable improved control over volume status by allowing more accurate estimation of ultrafiltration and dry weight goals. Errors in dry weight estimation can leave patients in either a hypovolemic or hypervolemic state after a HD session. This approach would provide a quantitative indicator of volume status and can be used to estimate dry weight by estimating the intramuscular interstitial space.

6.4.2 Clinical study design

The primary clinical question of the proposed clinical study will focus on the ability of the sensor to measure fluid volume status prior to and after HD. This could be assessed via three distinct experimental aims. The first would test the ability of this approach to assess interstitial volume depletion in stable HD patients. The second group would assess the robustness of the portable MR sensor measurements to solute filtration by recruiting patients on HD with no ultrafiltration volume. The third would recruit healthy control patients to establish a euvolemic signal. These capabilities would be assessed in collaboration with the Nephology Division at Massachusetts General Hospital (MGH) through a clinical study recruiting stable ESRD patients regularly undergoing HD.

The overarching hypothesis of the study would be as follows: We expect the MR signal amplitude to associate with interstitial volume depletion across individual treatments of subjects. We further expect no signal change in the subjects not receiving volume removal. Studying healthy controls using a portable MR device will establish a ‘normal’ reference range for the portable MR signal.

The patient recruitment and screening could proceed as follows: ESRD patients undergoing HD admitted to MGH and scheduled for a dialysis treatment would be screened. We would recruit relatively stable inpatient ESRD patients. The inclusion criteria would be: age between 18 and 80 years old, BMI between 18-30, and at least

8 weeks of stability on HD. The exclusion criteria would be patients admitted for cardiovascular events within 2 months, prior kidney transplant, severe anemia (Hgb < 7.5g/dL), pacemaker, implanted electrical devices, metal implants, limb amputations, and pregnancy/breastfeeding. We would select both patients undergoing routine dialysis with ultrafiltration as well as patients undergoing routine dialysis with no ultrafiltration.

The measurement with our sensor could be performed as follows: Our sensor would be used to measure fluid volume in the upper gastrocnemius muscle via standard CPMG pulse sequence scans until adequate signal quality is reached for accurate feature extraction. The operating frequency would be set to ensure sufficient penetration depth. Measurements would not interfere with or inform the HD protocol. Each scan would be expected to require approximately 5 minutes.

Measurements recorded before and after HD sessions would be used to assess the association between signal change and interstitial volume removal. Weight, blood pressure, routine lab results, and any acute dialysis events would also be recorded at the beginning and end of each session. Measurements from the portable MR sensor would be processed using a triexponential model. The time constants would represent the T2 decay rates of each fluid compartment. Their associated amplitudes would represent the relative amount of water in each compartment. The amplitude of the second component would indicate the relative amount of fluid present within the intramuscular ECF space.

The healthy control subject recruitment and screening could proceed as follows: Healthy volunteers would be admitted for a short four-hour stay at MGH. The subjects would undergo MR sensor evaluation as described previously. We would compare the healthy control signals to post dialysis readings to establish a baseline 'normal' signal against which to compare ESRD patients after HD. Healthy controls would be subject to bedrest for a 4 hour period to control for any confounding factors between ambulatory and bedbound patients.

The proposed approach of using portable MR sensors to identify fluid volume status via intramuscular measurements could help nephrologists differentiate euvolemia from hypervolemia or hypovolemia. A “dry” or euvolemic signal could be established with the healthy control population allowing for identification of patients who may benefit from additional ultrafiltration or who should avoid additional dry weight challenges. This signal could be incorporated into the decision making workflow when administering hemodialysis to ESRD patients (**Figure 6.1**).

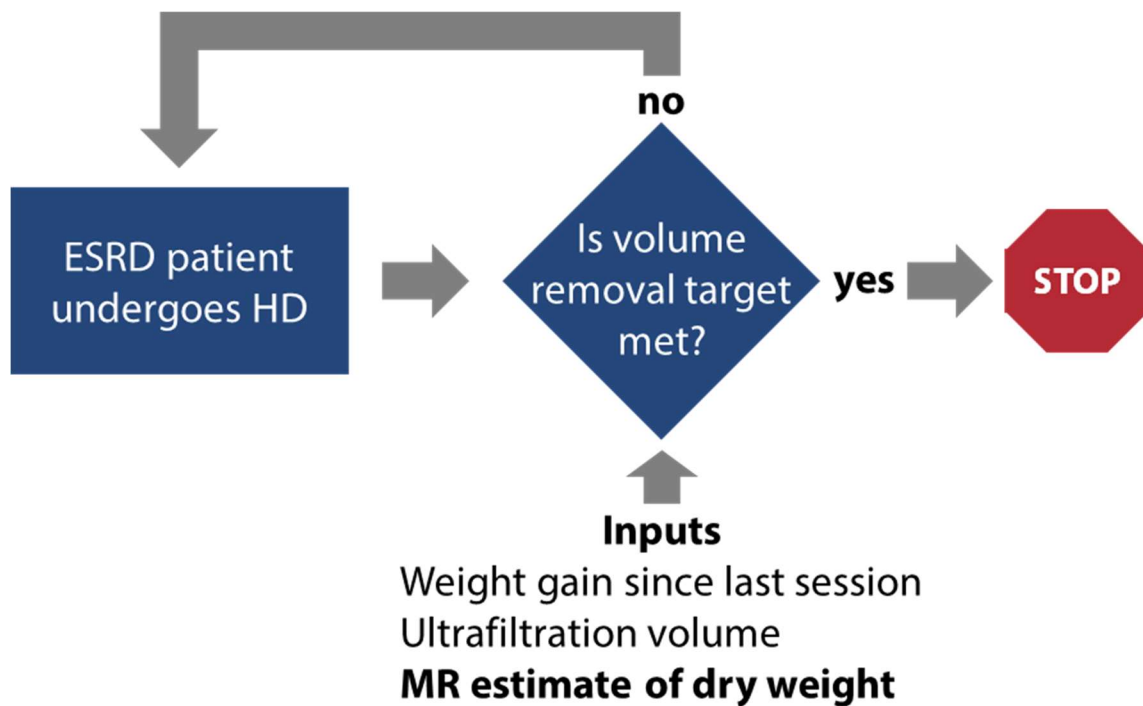


Figure 6.1. Schematic illustration of decision-support via portable MR measurement for ESRD patients. An ESRD patient undergoing HD will continue to receive HD until fluid removal and volume targets are met. Clinical signs such as weight gain and ultrafiltration volume currently guide these. An MR-based estimate of dry weight could aid in this decision making process.

Ultimately, this approach could provide a real-time measure of fluid volume status to guide the fluid removal target. The measurement would provide actionable information to avoid intradialytic hypotension and its adverse effects such as bowel ischemia, stroke, fistula thrombosis, myocardial infarction and stunning. Adaptive fluid removal protocols are critical to reduce incidence of adverse events such as hypotension. This could serve as a leading indicator of adverse events (e.g.

intradialytic hypotension) which we hope to evaluate in the future. The technology would improve long-term HD treatment by providing clinicians with a quantitative metric of patients' progress over multiple HD sessions. This technology could ultimately serve as a patient-based quality assessment tool.

6.5 Conclusions

This thesis broadly lays the foundation for next generation portable magnetic resonance sensors designed to interrogate tissue fluid distribution. The assessment of fluid depletion induced by dehydration highlights the utility of this approach. MR sensor-based advances towards clinical translation were explored and directions for continued development defined. In all, this work shows that portable magnetic resonance sensors have potential utility as clinical diagnostic devices for fluid volume imbalances.

Bibliography

1. Cheuvront, S. N. & Kenefick, R. W. Dehydration: Physiology, assessment, and performance effects. *Compr. Physiol.* **4**, 257–285 (2014).
2. Seymour, D. G., Henschke, P. J., Cape, R. D. T. & Campbell, A. J. Acute confusional states and dementia in the elderly: the role of dehydration/volume depletion, physical illness and age. *Age Ageing* **9**, 137–146 (1980).
3. Chan, H. Y. L. *et al.* Association between dehydration on admission and postoperative complications in older persons undergoing orthopaedic surgery. *J. Clin. Nurs.* (2018).
4. Lavizzo-Mourey, R., Johnson, J. & Stolley, P. Risk factors for dehydration among elderly nursing home residents. *J. Am. Geriatr. Soc.* **36**, 213–218 (1988).
5. Thomas, D. R. *et al.* Understanding clinical dehydration and its treatment. *J. Am. Med. Dir. Assoc.* **9**, 292–301 (2008).
6. Creditor, M. C. Hazards of hospitalization of the elderly. *Ann. Intern. Med.* **118**, 219–223 (1993).
7. Wakefield, B. J., Mentes, J., Holman, J. E. & Culp, K. Risk Factors and Outcomes Associated with Hospital Admission for Dehydration. *Rehabil. Nurs.* **33**, 233–241 (2008).
8. Marik, P. E. & Lemson, J. Fluid responsiveness: an evolution of our understanding. (2014).
9. Maughan, R. J. & Shirreffs, S. M. Development of hydration strategies to optimize performance for athletes in high-intensity sports and in sports with repeated intense efforts. *Scand. J. Med. Sci. Sports* **20**, 59–69 (2010).
10. Lindner, G. *et al.* Hypernatremia in the critically ill is an independent risk factor for mortality. *Am. J. Kidney Dis.* **50**, 952–957 (2007).
11. Xiao, H., Barber, J. & Campbell, E. S. Economic burden of dehydration among hospitalized elderly patients. *Am. J. Heal. Pharm.* **61**, 2534–2540 (2004).
12. Bolat, F. *et al.* What Is the Safe Approach for Neonatal Hypernatremic Dehydration?: A Retrospective Study From a Neonatal Intensive Care Unit. *Pediatr. Emerg. Care* **29**, 808–813 (2013).

13. Lindseth, P. D., Lindseth, G. N., Petros, T. V, Jensen, W. C. & Caspers, J. Effects of hydration on cognitive function of pilots. *Mil. Med.* **178**, 792–798 (2013).
14. Luippold, A. J. *et al.* Update: Efficacy of Military Fluid Intake Guidance. *Mil. Med.* (2018).
15. Messaris, E. *et al.* Dehydration is the most common indication for readmission after diverting ileostomy creation. *Dis. Colon Rectum* **55**, 175–180 (2012).
16. Sands, J. J. *et al.* Intradialytic hypotension: frequency, sources of variation and correlation with clinical outcome. *Hemodial. Int.* **18**, 415–422 (2014).
17. Warren, J. L. *et al.* The burden and outcomes associated with dehydration among US elderly, 1991. *Am. J. Public Health* **84**, 1265–1269 (1994).
18. Rolls, B. J. & Phillips, P. A. Aging and disturbances of thirst and fluid balance. *Nutr. Rev.* **48**, 137–144 (1990).
19. FAULL, C. M., HOLMES, C. & BAYLIS, P. H. Water balance in elderly people: is there a deficiency of vasopressin? *Age Ageing* **22**, 114–120 (1993).
20. Phillips, P. A. *et al.* Reduced thirst after water deprivation in healthy elderly men. *N. Engl. J. Med.* **311**, 753–759 (1984).
21. Hooper, L. *et al.* Clinical symptoms, signs and tests for identification of impending and current water-loss dehydration in older people. *Cochrane Database Syst. Rev.* (2015).
22. McGee, S., Abernethy III, W. B. & Simel, D. L. Is this patient hypovolemic? *Jama* **281**, 1022–1029 (1999).
23. Gross, C. R. *et al.* Clinical indicators of dehydration severity in elderly patients. *J. Emerg. Med.* **10**, 267–274 (1992).
24. Gorelick, M. H., Shaw, K. N. & Baker, M. D. Effect of ambient temperature on capillary refill in healthy children. *Pediatrics* **92**, 699–702 (1993).
25. McGarvey, J. *et al.* Sensitivity and specificity of clinical signs for assessment of dehydration in endurance athletes. *Br. J. Sports Med.* **44**, 716–719 (2010).
26. Gowans, E. M. & Fraser, C. G. Despite correlation, random spot and 24-h urine specimens are not interchangeable. *Clin. Chem.* **33**, 1080–1081 (1987).
27. Shephard, M. D., Penberthy, L. A. & Fraser, C. G. Short-and long-term biological variation in analytes in urine of apparently healthy individuals. *Clin. Chem.* **27**, 569–573 (1981).

28. Cheuvront, S. N., Kenefick, R. W. & Zambraski, E. J. Spot urine concentrations should not be used for hydration assessment: A methodology review. *Int. J. Sport Nutr. Exerc. Metab.* **25**, 293–297 (2015).
29. Harrison, M. H. Effects on thermal stress and exercise on blood volume in humans. *Physiol. Rev.* **65**, 149–209 (1985).
30. Cheuvront, S. N., Kenefick, R. W., Charkoudian, N. & Sawka, M. N. Physiologic basis for understanding quantitative dehydration assessment. *American Journal of Clinical Nutrition* **97**, 455–462 (2013).
31. Hori, S. S. & Gambhir, S. S. Mathematical model identifies blood biomarker-based early cancer detection strategies and limitations. *Sci. Transl. Med.* **3**, 109ra116 (2011).
32. Ely, B. R., Cheuvront, S. N., Kenefick, R. W. & Sawka, M. N. *Limitations of salivary osmolality as a marker of hydration status.* (ARMY RESEARCH INST OF ENVIRONMENTAL MEDICINE NATICK MA THERMAL AND MOUNTAIN MEDICINE DIVISION, 2011).
33. Ellis, K. J. *et al.* Bioelectrical impedance methods in clinical research: a follow-up to the NIH Technology Assessment Conference. *Nutrition* **15**, 874–880 (1999).
34. Buchholz, A. C., Bartok, C. & Schoeller, D. A. The validity of bioelectrical impedance models in clinical populations. *Nutr. Clin. Pract.* **19**, 433–446 (2004).
35. Kushner, R. F., Gudivaka, R. & Schoeller, D. A. Clinical characteristics influencing bioelectrical impedance analysis measurements. *Am. J. Clin. Nutr.* **64**, 423S–427S (1996).
36. Sieck, S. in *Short Stay Management of Acute Heart Failure* (ed. Peacock, W. F.) Chapter 2 (Humana Press, 2012). doi:10.1007/978-1-61779-627-2
37. Navas, J. P. & Martinez-Maldonado, M. Pathophysiology of Edema in Congestive Heart Failure. *Hear. Dis. Stroke* **2**, 325–329 (1993).
38. Patient, T. Congestive Heart Failure. 1–11 (2013).
39. Gheorghide, M., Filippatos, G., De Luca, L. & Burnett, J. Congestion in acute heart failure syndromes: an essential target of evaluation and treatment. *Am. J. Med.* **119**, S3–S10 (2006).
40. Albert, N. M. Fluid Management Strategies Heart Failure. *Crit. Care Nurse* **32**, 20–33 (2012).

41. Elixhauser, A. & Steiner, C. Readmissions to U.S. Hospitals by Diagnosis, 2010. *Healthc. Cost Util. Proj. Statistica*, 1–12 (2013).
42. Dekker, M. J. E. & Kooman, J. P. Fluid status assessment in hemodialysis patients and the association with outcome: Review of recent literature. *Curr. Opin. Nephrol. Hypertens.* **27**, 188–193 (2018).
43. Flythe, J. E. *et al.* Association of intradialytic blood pressure variability with increased all-cause and cardiovascular mortality in patients treated with long-term hemodialysis. *Am. J. Kidney Dis.* **61**, 966–974 (2013).
44. Chang, T. I. *et al.* Intradialytic Hypotension and Vascular Access Thrombosis. *J. Am. Soc. Nephrol.* 1526–1533 (2011). doi:10.1681/ASN.2010101119
45. Reilly, R. F. Attending rounds: A patient with intradialytic hypotension. *Clin. J. Am. Soc. Nephrol.* **9**, 798–803 (2014).
46. Zuidema, M. Y. & Dellsperger, K. C. Myocardial stunning with hemodialysis: clinical challenges of the cardiorenal patient. *Cardiorenal Med.* **2**, 125–133 (2012).
47. Murray, A. M. Cognitive impairment in the aging dialysis and chronic kidney disease populations: an occult burden. *Adv. Chronic Kidney Dis.* **15**, 123–132 (2008).
48. Jaeger, J. Q. & Mehta, R. L. Assessment of dry weight in hemodialysis an overview. *J. Am. Soc. Nephrol.* **10**, 392–403 (1999).
49. Flythe, J. E., Kimmel, S. E. & Brunelli, S. M. Rapid fluid removal during dialysis is associated with cardiovascular morbidity and mortality. *Kidney Int.* **79**, 250–257 (2011).
50. Agarwal, R. Volume Overload in Dialysis: The Elephant in the Room, No One Can See. *Am. J. Nephrol.* **38**, 75–77 (2013).
51. Ishibe, S. & Peixoto, A. J. Methods of Assessment of Volume Status and Intercompartmental Fluid Shifts in Hemodialysis Patients: Implications in Clinical Practice. in *Seminars in Dialysis* **17**, 37–43 (Wiley Online Library, 2004).
52. Dou, Y., Zhu, F. & Kotanko, P. Assessment of extracellular fluid volume and fluid status in hemodialysis patients: current status and technical advances. in *Seminars in dialysis* **25**, 377–387 (Wiley Online Library, 2012).
53. Weiner, D. E. *et al.* Improving clinical outcomes among hemodialysis patients: a proposal for a “volume first” approach from the chief medical officers of US

- dialysis providers. *Am. J. Kidney Dis.* **64**, 685–695 (2014).
54. Huang, S. H. S., Filler, G., Lindsay, R. & McIntyre, C. W. Euvolemia in Hemodialysis Patients: A Potentially Dangerous Goal? *Semin. Dial.* **28**, 1–5 (2015).
 55. Agarwal, R., Andersen, M. J. & Pratt, J. H. On the importance of pedal edema in hemodialysis patients. *Clin. J. Am. Soc. Nephrol.* **3**, 153–158 (2008).
 56. Chung, H.-M., Kluge, R., Schrier, R. W. & Anderson, R. J. Clinical assessment of extracellular fluid volume in hyponatremia. *Am. J. Med.* **83**, 905–908 (1987).
 57. Nose, H., Mack, G. W., Shi, X. R. & Nadel, E. R. Shift in body fluid compartments after dehydration in humans. *J. Appl. Physiol. (Bethesda, Md. 1985)* **65**, 318–324 (1988).
 58. Nose, H., Morimoto, T. & Ogura, K. Distribution of water losses among fluid compartments of tissues under thermal dehydration in the rat. *Jpn. J. Physiol.* **33**, 1019–29 (1983).
 59. Horowitz, M. & Samueloff, S. Plasma water shifts during thermal dehydration. *J. Appl. Physiol.* **47**, 738–744 (1979).
 60. Silverthorn, D. U., Ober, W. C., Garrison, C. W., Silverthorn, A. C. & Johnson, B. R. *Human physiology: an integrated approach*. (Pearson/Benjamin Cummings San Francisco, CA; 2004).
 61. Hackney, K. J., Cook, S. B., Fairchild, T. J. & Ploutz-Snyder, L. L. Skeletal muscle volume following dehydration induced by exercise in heat. *Extrem. Physiol. Med.* **1**, 3 (2012).
 62. Costill, D. L. & Fink, W. J. Plasma volume changes following exercise and thermal dehydration. *J. Appl. Physiol.* **37**, 521–525 (1974).
 63. Colucci, L. A. *et al.* Bedside magnetic relaxometry for fluid assessment in end-stage renal disease. *under Rev.* (2019).
 64. Fukushima, E. & Boden, N. *Experimental pulse NMR: A nuts and bolts approach*. *Biochemical Education* **10**, (Addison-Wesley, 1982).
 65. Bloch, F. Nuclear induction. *Phys. Rev.* **70**, 460–474 (1946).
 66. Björk, M., Zachariah, D., Kullberg, J. & Stoica, P. A multicomponent T2 relaxometry algorithm for myelin water imaging of the brain. *Magn. Reson. Med.* **75**, 390–402 (2016).

67. Cole, W. C., LeBlanc, a D. & Jhingran, S. G. The origin of biexponential T2 relaxation in muscle water. *Magn. Reson. Med.* **29**, 19–24 (1993).
68. Ababneh, Z. *et al.* Biexponential parameterization of diffusion and T2 relaxation decay curves in a rat muscle edema model: decay curve components and water compartments. *Magn. Reson. Med. An Off. J. Int. Soc. Magn. Reson. Med.* **54**, 524–531 (2005).
69. Juras, V. *et al.* Bi-exponential T2*analysis of healthy and diseased Achilles tendons: An in vivo preliminary magnetic resonance study and correlation with clinical score. *Eur. Radiol.* **23**, 2814–2822 (2013).
70. Li, M., Vassiliou, C. C., Colucci, L. A. & Cima, M. J. (1)H nuclear magnetic resonance (NMR) as a tool to measure dehydration in mice. *NMR Biomed.* **28**, 1031–9 (2015).
71. Saab, G., Thompson, R. T. & Marsh, G. D. Multicomponent T 2 Relaxation of In Vivo Skeletal Muscle. *Magn. Reson. Med.* **157**, 150–157 (1999).
72. Cole, W. C., LeBlanc, A. D. & Jhingran, S. G. The origin of biexponential T2 relaxation in muscle water. *Magn. Reson. Med.* **29**, 19–24 (1993).
73. Gambarota, G., Cairns, B. E., Berde, C. B. & Mulkern, R. V. Osmotic effects on the T2 relaxation decay of in vivo muscle. *Magn. Reson. Med. An Off. J. Int. Soc. Magn. Reson. Med.* **46**, 592–599 (2001).
74. Araujo, E. C. A., Fromes, Y. & Carlier, P. G. New insights on human skeletal muscle tissue compartments revealed by in vivo T2 NMR relaxometry. *Biophys. J.* **106**, 2267–2274 (2014).
75. Casanova, F., Perlo, J. & Blümich, B. *Single-sided NMR. Single-Sided NMR* (Springer Berlin Heidelberg, 2011). doi:10.1007/978-3-642-16307-4
76. Demas, V. & Prado, P. J. Compact Magnets for Magnetic Resonance. *Concepts Magn. Reson. Part A Bridg. Educ. Res.* (2009). doi:10.1002/cmr.a.20131
77. Marble, A. E., Mastikhin, I. V., Colpitts, B. G. & Balcom, B. J. A compact permanent magnet array with a remote homogeneous field. *J. Magn. Reson.* **186**, 100–104 (2007).
78. Möller, R., Tafeit, E., Pieber, T. R., Sudi, K. & Reibnegger, G. Measurement of subcutaneous adipose tissue topography (SAT-Top) by means of a new optical device, LIPOMETER, and the evaluation of standard factor coefficients in healthy subjects. *Am. J. Hum. Biol. Off. J. Hum. Biol. Assoc.* **12**, 231–239 (2000).

79. Graham, S. J., Stanchev, P. L. & Bronskill, M. J. Criteria for analysis of multicomponent tissue T2 relaxation data. *Magn. Reson. Med.* **35**, 370–378 (1996).
80. Kornetka, D., Trammer, M. & Zange, J. Evaluation of a mobile NMR sensor for determining skin layers and locally estimating the T2eff relaxation time in the lower arm. *Magn. Reson. Mater. Physics, Biol. Med.* **25**, 455–466 (2012).
81. Blümich, B. *et al.* Advances of unilateral mobile NMR in nondestructive materials testing. *Magn. Reson. Imaging* **23**, 197–201 (2005).
82. Danieli, E. & Blümich, B. Single-sided magnetic resonance profiling in biological and materials science. *J. Magn. Reson.* **229**, 142–154 (2013).
83. Guthausen, A. *et al.* Measurement of fat content of food with single-sided NMR. *J. Am. Oil Chem. Soc.* **81**, 727–731 (2004).
84. Dabaghyan, M. *et al.* A portable single-sided magnet system for remote NMR measurements of pulmonary function. *NMR Biomed.* **27**, 1479–1489 (2014).
85. Eidmann, G., Savelsberg, R., Blümmler, P. & Blümich, B. The NMR MOUSE, a mobile universal surface explorer. *J. Magn. Reson. Ser. A* **122**, 104–109 (1996).
86. Blümich, B. *et al.* Simple NMR-MOUSE with a bar magnet. *Concepts Magn. Reson. Part B Magn. Reson. Eng.* **15**, 255–261 (2002).
87. Chang, W. H., Chen, J. H. & Hwang, L. P. Single-sided mobile NMR with a Halbach magnet. *Magn. Reson. Imaging* **24**, 1095–1102 (2006).
88. Prado, P. J., Blümich, B. & Schmitz, U. One-Dimensional Imaging with a Palm-Size Probe. *J. Magn. Reson.* **144**, 200–206 (2000).
89. Landeghem, M. Van, Danieli, E., Perlo, J., Blümich, B. & Casanova, F. Low-gradient single-sided NMR sensor for one-shot profiling of human skin. *J. Magn. Reson.* **215**, 74–84 (2011).
90. Utsuzawa, S. & Fukushima, E. Unilateral NMR with a barrel magnet. *J. Magn. Reson.* **282**, 104–113 (2017).
91. Fukushima, E. & Jackson, J. A. Unilateral magnet having a remote uniform field region for nuclear magnetic resonance. (2002).
92. Pulyer, Y. M. & Patz, S. MRI probe for external imaging. (1996).
93. Pulyer, Y. M. & Hrovat, M. I. Generation of remote homogeneous magnetic fields. *IEEE Trans. Magn.* **38**, 1553–1563 (2002).

94. Halbach, K. Design of permanent multipole magnets with oriented rare earth cobalt material. *Nucl. Instruments Methods* **169**, 1–10 (1980).
95. Landeghem, M. Van, Danieli, E., Perlo, J., Blümich, B. & Casanova, F. Low-gradient single-sided NMR sensor for one-shot profiling of human skin. *J. Magn. Reson.* **215**, 74–84 (2011).
96. Tayler, M. C. D. & Sakellariou, D. Low-cost, pseudo-Halbach dipole magnets for NMR. *J. Magn. Reson.* **277**, 143–148 (2017).
97. Hoult, D. I. & Richards, R. E. The signal-to-noise ratio of the nuclear magnetic resonance experiment. *J. Magn. Reson.* **24**, 71–85 (1976).
98. Kobzar, K., Skinner, T. E., Khaneja, N., Glaser, S. J. & Luy, B. Exploring the limits of broadband excitation and inversion pulses. *J. Magn. Reson.* **170**, 236–243 (2004).
99. Vassiliou, C. C. Biopsy-Implantable Chemical Sensor. (MIT, 2013).
100. Parker, A. J., Zia, W., Rehorn, C. W. G. & Blümich, B. Shimming Halbach magnets utilizing genetic algorithms to profit from material imperfections. *J. Magn. Reson.* **265**, 83–89 (2016).
101. Gottvald, A. Optimal magnet design for NMR. *IEEE Trans. Magn.* **26**, 399–402 (1990).
102. SONG, T. Subcutaneous tissue depth differences between males and females*1The need for gender based epinephrine needle. *J. Allergy Clin. Immunol.* **113**, S241 (2004).
103. Perlo, J., Casanova, F. & Blümich, B. Single-sided sensor for high-resolution NMR spectroscopy. *J. Magn. Reson.* **180**, 274–279 (2006).
104. Bashyam, A., Li, M. & Cima, M. J. Design and experimental validation of Unilateral Linear Halbach magnet arrays for single-sided magnetic resonance. *J. Magn. Reson.* **292**, 36–43 (2018).
105. Burstein, D. Stimulated echoes: Description, applications, practical hints. *Concepts Magn. Reson.* **8**, 269–278 (1996).
106. Pell, G. S. *et al.* Optimized clinical T2 relaxometry with a standard CPMG sequence. *J. Magn. Reson. Imaging* **23**, 248–252 (2006).
107. Deacon, R. M. J. Housing, husbandry and handling of rodents for behavioral experiments. *Nat. Protoc.* **1**, 936 (2006).
108. Ellacott, K. L. J., Morton, G. J., Woods, S. C., Tso, P. & Schwartz, M. W.

- Assessment of feeding behavior in laboratory mice. *Cell Metab.* **12**, 10–17 (2010).
109. NAKAMURA, Y. & SUZUKI, K. Tunnel use facilitates handling of ICR mice and decreases experimental variation. *J. Vet. Med. Sci.* **80**, 886–892 (2018).
 110. Hazlewood, C. F., Chang, D. C., Nichols, B. L. & Woessner, D. E. Nuclear magnetic resonance transverse relaxation times of water protons in skeletal muscle. *Biophys. J.* **14**, 583–606 (1974).
 111. Hardy, P. A., Henkelman, R. M., Bishop, J. E., Poon, E. C. S. & Plewes, D. B. Why fat is bright in RARE and fast spin-echo imaging. *J. Magn. Reson. imaging* **2**, 533–540 (1992).
 112. Bydder, M. *et al.* Relaxation effects in the quantification of fat using gradient echo imaging. *Magn. Reson. Imaging* **26**, 347–359 (2008).
 113. Bai, R., Koay, C. G., Hutchinson, E. & Basser, P. J. A framework for accurate determination of the T2 distribution from multiple echo magnitude MRI images. *J. Magn. Reson.* **244**, 53–63 (2014).
 114. Gudbjartsson, H. & Patz, S. The Rician distribution of noisy MRI data. *Magn. Reson. Med.* **34**, 910–914 (1995).
 115. Koay, C. G., Özarslan, E. & Basser, P. J. A signal transformational framework for breaking the noise floor and its applications in MRI. *J. Magn. Reson.* **197**, 108–119 (2009).
 116. Armstrong, L. E. & Armstrong, L. Assessing Hydration Status : The Elusive Gold Standard. *J. Am. Coll. Nutr.* **26**, 26 (14): 575-84 (2007).
 117. Garcia, J. MRI in inflammatory myopathies. *Skeletal Radiol.* **29**, 425–438 (2000).
 118. Meler, J. D. *et al.* The MR appearance of volume overload in the lower extremities. *J. Comput. Assist. Tomogr.* **21**, 969–73 (1997).
 119. Darrow, D. C. & Yannet, H. The changes in the distribution of body water accompanying increase and decrease in extracellular electrolyte. *J. Clin. Invest.* **14**, 266–275 (1935).
 120. Mange, K. *et al.* Language guiding therapy: the case of dehydration versus volume depletion. *Ann. Intern. Med.* **127**, 848–853 (1997).
 121. Nadal, J. W., Pedersen, S. & Maddock, W. G. A comparison between dehydration from salt loss and from water deprivation. *J. Clin. Invest.* **20**, 691–703 (1941).

122. Fleckenstein, J. L., Canby, R. C., Parkey, R. W. & Peshock, R. M. Acute effects of exercise on MR imaging of skeletal muscle in normal volunteers. *Am. J. Roentgenol.* **151**, 231–237 (1988).
123. Ploutz-Snyder, L. L., Convertino, V. A. & Dudley, G. A. Resistance exercise-induced fluid shifts: change in active muscle size and plasma volume. *Am. J. Physiol. Integr. Comp. Physiol.* **269**, R536–R543 (1995).
124. Bashyam, A., Frangieh, C., Li, M. & Cima, M. J. Dehydration assessment via a non-invasive, miniature, portable magnetic resonance sensor using multicomponent T2 relaxometry. *under Rev.* (2019).
125. Istratov, A. A. & Vyvenko, O. F. Exponential analysis in physical phenomena. *Rev. Sci. Instrum.* **70**, 1233–1257 (1999).
126. Fenrich, F. R. E., Beaulieu, C. & Allen, P. S. Relaxation times and microstructures. *NMR Biomed. An Int. J. Devoted to Dev. Appl. Magn. Reson. Vivo* **14**, 133–139 (2001).
127. Saab, G., Thompson, R. T. & Marsh, G. D. Multicomponent T2 relaxation of in vivo skeletal muscle. *Magn. Reson. Med. An Off. J. Int. Soc. Magn. Reson. Med.* **42**, 150–157 (1999).
128. Bendel, P. Spin-echo attenuation by diffusion in nonuniform field gradients. *J. Magn. Reson.* **86**, 509–515 (1990).
129. Le Bihan, D., Poupon, C., Amadon, A. & Lethimonnier, F. Artifacts and pitfalls in diffusion MRI. *J. Magn. Reson. Imaging An Off. J. Int. Soc. Magn. Reson. Med.* **24**, 478–488 (2006).
130. Richard, S. *et al.* Characterization of the skin in vivo by high resolution magnetic resonance imaging: water behavior and age-related effects. *J. Invest. Dermatol.* **100**, 705–709 (1993).
131. Heemskerk, A. M. & Damon, B. M. Diffusion tensor MRI assessment of skeletal muscle architecture. *Curr. Med. Imaging Rev.* **3**, 152–160 (2007).
132. Fan, R. H. & Does, M. D. Compartmental relaxation and diffusion tensor imaging measurements in vivo in λ -carrageenan-induced edema in rat skeletal muscle. *NMR Biomed. An Int. J. Devoted to Dev. Appl. Magn. Reson. vivo* **21**, 566–573 (2008).
133. Shoji, T., Tsubakihara, Y., Fujii, M. & Imai, E. Hemodialysis-associated hypotension as an independent risk factor for two-year mortality in hemodialysis patients. *Kidney Int.* **66**, 1212–1220 (2004).

134. Beloeil, H. *et al.* Effects of Bupivacaine and Tetrodotoxin on Carrageenan-induced Hind Paw Inflammation in Rats (Part 1) Hyperalgesia, Edema, and Systemic Cytokines. *Anesthesiol. J. Am. Soc. Anesthesiol.* **105**, 128–138 (2006).
135. Scallan, J., Huxley, V. H. & Korthuis, R. J. Capillary Fluid Exchange: Regulation, Functions, and Pathology. in *Colloquium Series on Integrated Systems Physiology: From Molecule to Function* **2**, 1–94 (Morgan & Claypool Publishers, 2010).
136. Sen, P. N., André, A. & Axelrod, S. Spin echoes of nuclear magnetization diffusing in a constant magnetic field gradient and in a restricted geometry. *J. Chem. Phys.* **111**, 6548–6555 (1999).
137. Axelrod, S. & Sen, P. N. Nuclear magnetic resonance spin echoes for restricted diffusion in an inhomogeneous field: Methods and asymptotic regimes. *J. Chem. Phys.* **114**, 6878–6895 (2001).
138. de Swiet, T. M. & Sen, P. N. Decay of nuclear magnetization by bounded diffusion in a constant field gradient. *J. Chem. Phys.* **100**, 5597–5604 (1994).
139. d'Eurydice, M. N. & Galvosas, P. Measuring diffusion–relaxation correlation maps using non-uniform field gradients of single-sided NMR devices. *J. Magn. Reson.* **248**, 137–145 (2014).
140. Rata, D. G., Casanova, F., Perlo, J., Demco, D. E. & Blümich, B. Self-diffusion measurements by a mobile single-sided NMR sensor with improved magnetic field gradient. *J. Magn. Reson.* **180**, 229–235 (2006).
141. Grebenkov, D. S. Multiexponential attenuation of the CPMG spin echoes due to a geometrical confinement. *J. Magn. Reson.* **180**, 118–126 (2006).
142. de Almeida Martins, J. P. & Topgaard, D. Multidimensional correlation of nuclear relaxation rates and diffusion tensors for model-free investigations of heterogeneous anisotropic porous materials. *Sci. Rep.* **8**, 2488 (2018).
143. Bipin Mehta, B. *et al.* Magnetic resonance fingerprinting: a technical review. *Magn. Reson. Med.* **81**, 25–46 (2019).
144. Geethanath, S. *et al.* Compressed sensing MRI: a review. *Crit. Rev. Biomed. Eng.* **41**, (2013).
145. Jin, K. H., Unser, M. & Yi, K. M. Self-Supervised Deep Active Accelerated MRI. *arXiv Prepr. arXiv1901.04547* (2019).